THE LEADING-EDGE EFFECTS ON A LAMINAR FLAT-PLATE BOUNDARY LAYER AT MACH 10.4

A Thesis

Presented to

the Faculty of the School of Engineering and Applied Science

University of Virginia

In Partial Fulfillment

of the Requirements for the Degree

Master of Aerospace Engineering

by

Howard W. Stone

May 1968

APPROVAL SHEET

This thesis is submitted in partial fulfillment of

the requirements for the degree of

Master of Aerospace Engineering

_____

Author

Approved:

_____

Faculty Advisor

_____

Dean, School of Engineering and
Applied Science

May 1968

ACKNOWLEDGMENTS

The author is indebted to the National Aeronautics and Space Administration for permission to use material obtained from a research project at the Langley Research Center in this thesis. Particular thanks are due to Robert W. Rainey, Assistant Head of the Hypersonic Aerodynamics Branch, for serving as an off-campus advisor.

The author is also grateful to Dr. W. G. Rose for his guidance at the inception of the project and to Dr. J. O. Bunting for his assistance in preparing this thesis.

TABLE OF CONTENTS

LIST OF FIGURES

FIGURE PAGE

LIST OF SYMBOLS

a	speed of sound
C_D	nose drag coefficient
C_f	local skin friction coefficient
C_m	heat capacity of the metal
C_p	constant pressure heat capacity of air
C_w	$= \frac{\mu_w}{\mu_\infty} \frac{T_\infty}{T_w}$
d	leading-edge diameter
D	nose drag
E	total energy
f	$\equiv 1/2 \int_0^\eta \rho^* u^* d\eta$
$F(\gamma)$	undetermined function in equation 6
$g(x)$	boundary layer growth function
G	function defined by equation 2
h	enthalpy
$\bar{h}$	heat transfer coefficient
K_3	pressure gradient correction factor
K_4	an integral function plotted in reference 11
K_5	$\equiv M_\infty (\frac{d\delta}{dx})$
M	Mach number
n	exponent in power law variation of wall pressure, $P_w \propto x^n$

N_{Pr}	Prandtl number
N_{ST}	Stanton number
p	pressure
Δp	$p-p_\infty$
p_{t_3}	impact pressure
$\dot{q}_A$	heat transfer
r	recovery factor
R	distance of blast wave from the origin
$R_{\infty,d}$	Reynolds number based on free-stream conditions and the leading-edge diameter
$R_{\infty,x}$	Reynolds number based on free-stream conditions and the distance from the leading edge
t	metal thickness
T	temperature
u	velocity
x	distance from the leading edge
y	distance perpendicular to model surface
z	lateral distance on model surface measured from model centerline
α	accommodation parameter
γ	ratio of the specific heats
δ	boundary layer thickness
δ'	characteristic boundary layer thickness

ϵ $\approx 1 - [0.0048/(\gamma - 1)]^2$

η Blasius similarity variable, $\frac{y}{x}\sqrt{R_{\infty,x}}$

θ $\equiv \frac{h-h_\infty}{h_t-h_\infty}$

θ_s angle of shock wave inclination with free-stream direction

μ viscosity

μ' apparent viscosity = $\frac{\mu\rho}{\rho+q\mu}$

ρ density

ρ_m metal density

τ time

χ_∞ $\equiv \frac{M_\infty^3}{\sqrt{R_{\infty,x}}}$

$\bar{\chi}_\infty$ $\equiv \frac{M_\infty^3\sqrt{C_w}}{\sqrt{R_{\infty,x}}}$

Subscripts:

aw adiabatic wall

e boundary layer edge condition

l local condition

t total (stagnation) condition

w wall condition

z static condition behind a shock wave

∞ freestream

Superscript:

* dimensionless quantity based on free-stream conditions (i.e., $u^* = u/u_\infty$)

ABSTRACT

An experimental investigation was performed at Mach 10.4 in air on a 30 inch flat plate model with cylinderical leading edges of 0.002 inches, 0.063 inches, and 0.50 inches in diameter to examine the leading edge thickness effect on the laminar boundary layer. The free stream Reynolds number based on leading edge diameter was varied between 73 and 70,000. Wall pressure distributions, boundary layer impact pressure surveys, and wall heat transfer distributions were measured and velocity profiles, boundary layer growth, skin friction, and Reynolds analogy factor were determined.

The wall pressure distributions are compared with a viscous interaction theory and the modified "blast wave" theory. The boundary layer profiles, skin friction, and heat transfer are compared with a zero-pressure gradiant laminar boundary layer theory and a boundary layer growth correlation is shown.

Chapter I

INTRODUCTION

Vehicles moving at hypersonic speeds in the atmosphere must have blunt leading edges to avoid locally intolerable skin temperatures. The vehicle boundary layer must then grow in a pressure field generated by the bluntness. Temperatures in the boundary layer become very high, reducing the mass flux and displacing the inviscid flow field. This displacement provides a new "effective" body shape, which produces a further perturbation of the flow field.

The streamlines entering the low mass flux hypersonic boundary layer far downstream of the leading edge will have passed through the strong leading edge shock and will therefore have a reduced total pressure. The characteristics of a boundary layer growing in this bluntness and viscous-induced flow field have been a subject for study by many researchers. The first approach has been to study the extremes of the problem. That is, to study the sharp leading edge model with its purely viscous-induced pressure gradient and the very blunt leading edge model with predominantly an inviscid induced pressure gradient.

Lees and Probstein (Ref. 1) published one of the first analytical studies of the viscous-induced pressure gradient behind a sharp leading edge in hypersonic flow. In this work it was assumed that Mach waves, extending from the growing boundary layer to the shock, produce negligible reflected waves. Therefore, the region between the boundary layer edge and the shock is an isentropic Prandtl-Meyer type of flow. This type of interaction is called a weak interaction. The tangent-wedge approach is an approximation to the oblique shock wave equation for high Mach numbers and slender bodies. This approach is used to determine the local pressure with the effective body being described by the boundary layer displacement thickness of a zero-pressure-gradient flat plate solution. From this analysis, the main interaction parameter was found to be

$$\chi_\infty = M_\infty^3 / \sqrt{R_{\infty,x}}$$

and the weak-interaction regime encompassed values of χ_∞ less than about one.

For values of χ_∞ much greater than one, a strong interaction region would be encountered. In this region, the reflected waves affect the boundary layer growth. Closer to the leading edge the shock wave is very close to the surface and new flow models must be applied. E. S. Moulic, Jr., has a rather complete review of the analytical work in this flow regime in Reference 2.

The blunt flat plate has generally been treated by the inviscid blast-wave analogy to obtain the pressure distribution and shock-wave shape. Lees (Ref. 3) showed the similarity between the flow behind an intense blast wave and the transverse flow field of a flat plate with a blunt nose in a hypersonic flow. He was then able to relate the shock shape and wall pressure distribution to the blast wave and the pressure behind the blast wave.

Cheng, et al., (Ref. 4) considered the combined case of leading edge bluntness and boundary layer displacement. They used a flow model consisting of a thin detached shock layer and an entropy layer to obtain a "zero-order" theory for the boundary layer on a flat plate with leading edge bluntness. The asymptotic solutions of the theory agree with blast wave analogy when the bluntness induced effects are dominant, and agree with strong interaction theory when viscous-induced effects are dominant. Reference 4 also had a solution for the heat transfer.

Several experimental studies have been conducted on flat plates with sharp leading edges. Kendall (Ref. 5) measured the wall pressure distribution and the impact pressures from the wall to the shock wave on a 7-inch sharp leading edge flat plate at $M_\infty = 5.8$. He found that the measured viscous-induced wall pressures were about 25 percent greater than the weak interaction theory of Lees (Ref. 6). The impact pressure measurements and an experimental determination of the shock wave shape indicated that the static

pressure and the flow deflection were nearly constant along the Mach waves between the boundary layer and the shock, implying that the reflected waves from the shock were very weak. This corroborated the assumption of the weak interaction theory. He also found the Mach lines were nearly parallel to the shock, and thus, the shock strength must decay very slowly. The average skin friction coefficient was nearly equal to the zero-pressure gradient value downstream but was approximately twice the zero-pressure gradient value near the leading edge.

Graham and Vas (Ref. 7) measured the shock shapes and wall pressure distributions behind sharp and blunt (square and cylindrical) leading edges on a 4.25 inch model in helium at $M_\infty = 11.7$. They found that Lees' first-order weak interaction theory (Ref. 1) did not predict the pressure level for the sharp leading edge, whereas the blast wave analogy adequately predicted the pressures for the thickest leading edge ($R_{\infty d} \approx 21 \times 10^3$).

The surface pressure and heat transfer distributions back to four inches from the leading edge on sharp and blunt flat plates were obtained by Marvin (Ref. 8) in helium at $M_\infty = 12.5$ and 14.7. The sharp leading edge pressure data were in fair agreement with the first-order weak interaction theory of Lees in Reference 6. There appears to be contradictory data in References 7 and 8, since one set of data agrees with Lees' weak interaction theory and the other does not. However, while theories in both references are

credited to Lees, the evaluation of the Mach number and wall temperature effects apparently differ between References 7 and 8. Also in Reference 7 the sharp leading edge Reynolds number was approximately 200 as compared to 900 in Reference 8. The blunt leading edge pressure data of Reference 8 ($30 \times 10^3 \leq R_{\infty,d} \leq 120 \times 10^3$) is proportional to $(x/d)^{-.89}$ instead of $(x/d)^{-.667}$ as is expected from blast wave analogy. Marvin (Ref. 8) did find a correlation in terms of $(R_{\infty,d})^{.25}\ \Delta p/p$ versus x/d. The heat transfer data for the sharp leading edge model compared favorably with a theory by Bertram and Feller (Ref. 9) which accounts for the slight pressure gradient.

Measurements of wall pressures and heat transfer within five inches of the leading edge of sharp and blunt flat plates in a $M_\infty = 20$ hotshot tunnel using nitrogen as the test gas were reported by Harvey (Ref. 10). The sharp leading edge pressure data show a good comparison with Bertram and Feller's strong interaction theory (Ref. 9), but the theoretical heat transfer rates were about 20 percent below the measured data. Linear addition of the modified strong interaction theory to the modified blast wave theory (Ref. 11) gave a good prediction of the pressures and poor prediction of heat transfer rates behind the blunt leading edges.

In the lower Mach number range ($M_\infty = 5.7$), Creager (Ref. 12) made impact pressure surveys of the region between the wall and the shock wave and measured surface pressures within seven inches of

the leading edge of flat plate models with various leading-edge thicknesses. A linear combination of the weak interaction theory and a blast wave term did not satisfactorily predict wall pressure data for any leading-edge configuration. An attempt was made to correlate the boundary layer edge total pressure as a function of x/d. For large x/d ($x/d \geq 200$), the data scattered around the boundary layer edge total pressure to free-stream total pressure ratio of 1 and for small x/d ($x/d \leq 40$), the ratio was near the normal shock value. Relatively few data points fell in the intermediate range of x/d, but it appeared that the data would not correlate in terms of x/d.

Tests of a two-foot flat plate in a Mach 6.8 airstream with various bluntnesses were reported by Neal (Ref. 13). Wall pressure data for the sharp leading-edge model were satisfactorily predicted by weak interaction theory (Ref. 11). The maximum value of $\overline{\chi}_\infty$ was 0.55 for these tests. The blast wave analogy of Reference 14 predicted a slightly higher pressure level than the level of data for the very blunt leading-edge model. The pressure data for the intermediate bluntness were satisfactorily predicted by a linear addition of the strong viscous interaction and inviscid pressure theories. Progressively blunting the leading edge first decreased the heat transfer and then increased the heat transfer relative to the sharp leading-edge value as long as the boundary layer remained laminar. Skin friction data obtained by a floating-

element balance agreed with the heat transfer data when converted by Colburn's modification to Reynolds analogy based on boundary layer edge conditions.

Recently, Townsend, Vollmar, and Vas (Ref. 15) measured the bluntness effect on wall pressures and heat transfer to a five-inch flat plate at $M_\infty = 10.3$ in air. The leading edge was blunted by grinding a flat face normal to the plate surface. The pressure data showed that a very slight leading edge bluntness did not affect the measured pressure, and the sharp leading edge data agreed with theory (Ref. 11, "complete" theory). Blast wave analogy predicted a pressure level above the data for the blunt leading edge ($R_{\infty,d}$ = 7425 and 14,550). Slight bluntness did not change the heat transfer from the sharp leading edge value but further blunting increased the heat transfer. The Bertram and Feller theory agreed with all the data.

In the Mach number range of 10 to 12, the references noted herein show that the leading edge effect on the wall pressure distribution has been the subject of greatest study. Much of this work has been done in helium, and the results are not in complete agreement. For the investigation in air (Ref. 15), the maximum Reynolds number based on the leading edge diameter was 14,550, which does not seem very blunt when compared to $R_{\infty,d} \approx$ 21,000 to 120,000 in the helium tests.

Some neglected areas of investigation include the unit Reynolds number effect in conjunction with leading-edge bluntness and the leading-edge effect on boundary-layer distributions, boundary-layer growth, and skin friction. Most of the experimental investigations have been conducted on relatively short models; however, since flight vehicles may have extended regions of laminar boundary layer, the leading-edge effect "far" from the leading edge is of interest. The present investigation was designed to examine these deficiencies in the experimental knowledge of the leading-edge effect on the laminar boundary layer.

In this investigation, a 30-inch model was tested in air at Mach 10.4 with leading-edge thicknesses of 0.002, 0.063, and 0.50 inches. The resulting ranges of x/d for which data were obtained are 1920 to 14,500; 93 to 469, and 8.25 to 58.5 for the three leading edges, respectively. Wall pressure distributions were measured over a range of $R_{\infty,d}$ from 73 to 70,000. Impact pressure surveys, the determination of the velocity profiles, and comparisons with a zero-pressure gradient theory have also been made. The boundary-layer thickness, the skin friction, and heat transfer were obtained "far" from the leading edge and the effect of the leading-edge thickness on Reynolds analogy factor was examined.

The present experimental program was carried out in the Langley Continuous Flow Hypersonic Tunnel. The facility is capable of maintaining the test stagnation conditions at a more constant

level and over a longer period of time than the usual blow-down tunnels. Thus, there was always ample time for the pressure instrumentation to reach steady state. The boundary-layer probe design and the instrumentation configurations were optimized to obtain the most accurate measured data possible in this hypersonic air tunnel. The unit Reynolds number was varied from about 0.04×10^6/inch to 0.13×10^6/inch. Also T_w/T_{aw} was about 0.4 which is much closer to a flight value than a ratio of nearly 1.0 for tests in helium.

A complete description of the facility, the models, the instrumentation, and the test procedures is presented in Chapter II. Chapter III contains a discussion of the theoretical methods and the data reduction procedures are presented in Chapter IV. The results and analysis of the experiment program and comparisons with theory are presented in Chapter V.

CHAPTER II

APPARATUS AND TESTS

Facility

The facility used for these tests was a continuous-flow hypersonic tunnel with a 31-inch-square test section using air (dewpoint $\approx -30^{\circ}$ F) as the test gas. A schematic diagram of the tunnel circuit is shown in Figure 1. The vacuum sphere and high-pressure air-supply bottles were used to initiate the hypersonic flow. When hypersonic flow was achieved in the tunnel, the second minimum in the diffuser was closed down to about 25 percent of the test section area, and the compressors then maintained the hypersonic flow for the tests. The heaters are tubular electrical resistance elements. The throat used for these tests was constructed of beryllium copper with cooling water passages. A photograph of the tunnel is shown in Figure 2.

For the purpose of these tests the model was attached to the injection mechanism shown mounted on the side of the tunnel in Figure 3. The model is shown mounted on the strut attached to the injection mechanism in the retracted position in Figure 4. The photograph was taken through the test section with the injection box door open.

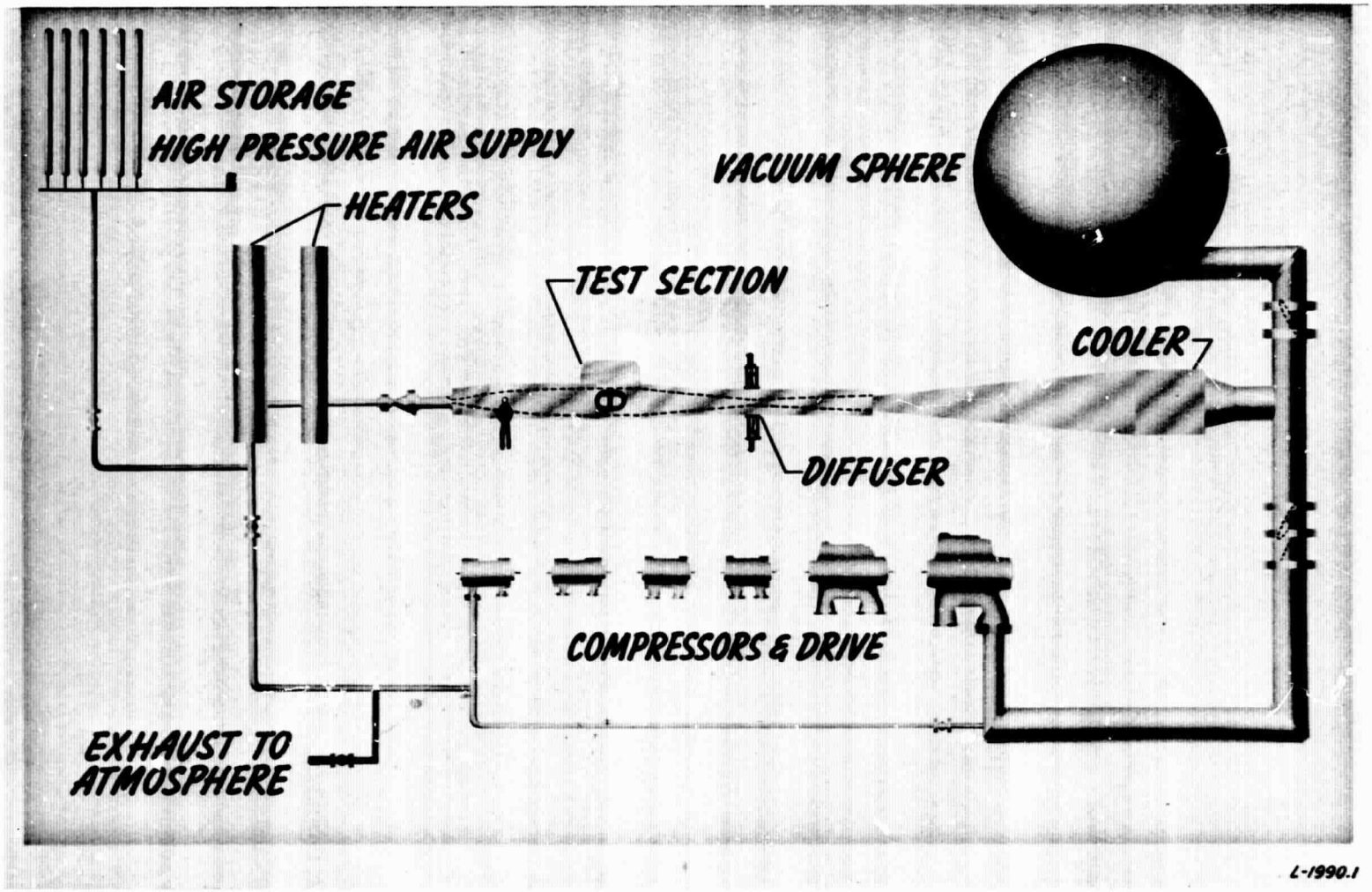

Figure 1.- Schematic diagram of the facility.

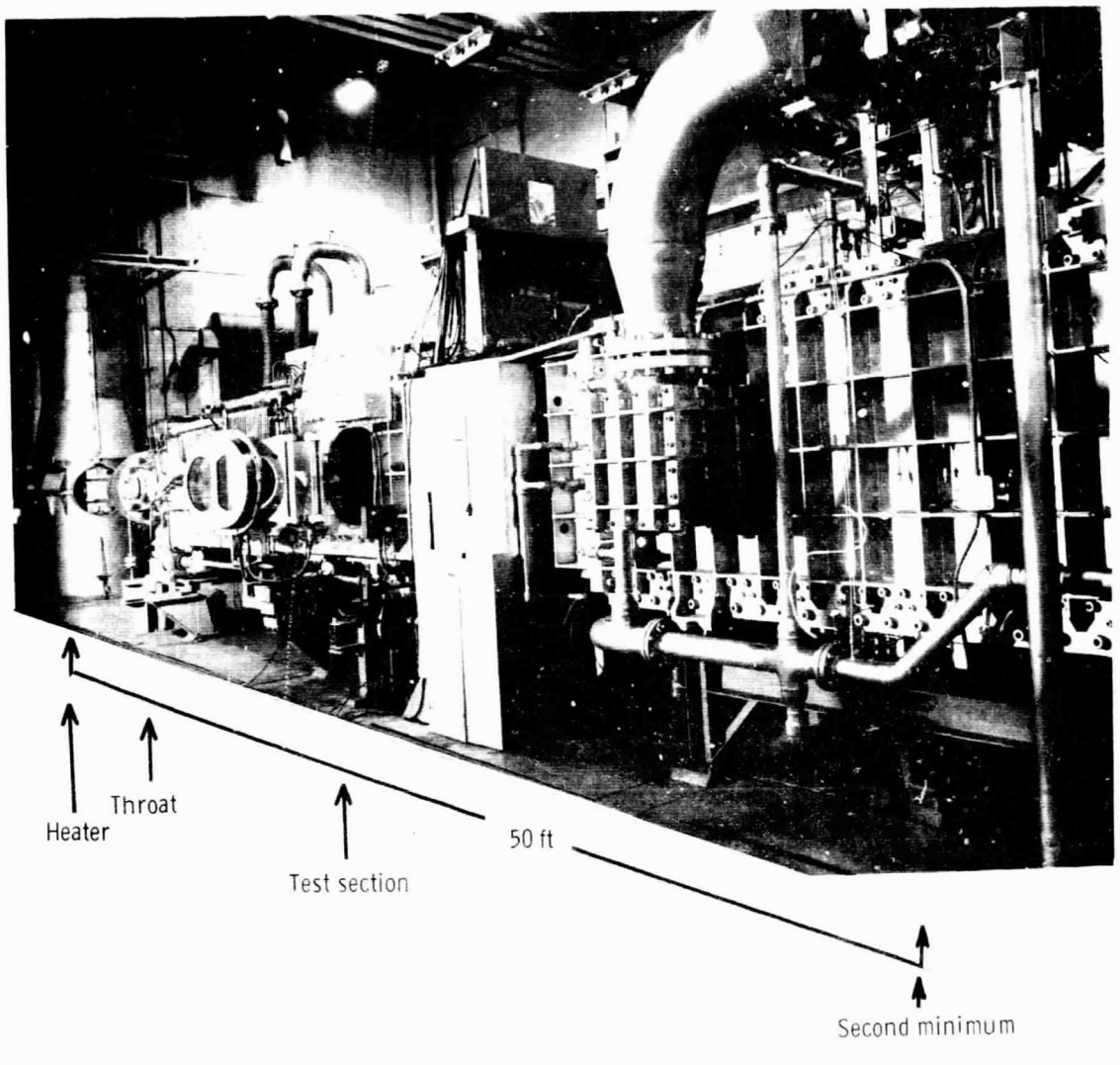

Figure 2.- Langley continuous flow hypersonic tunnel.

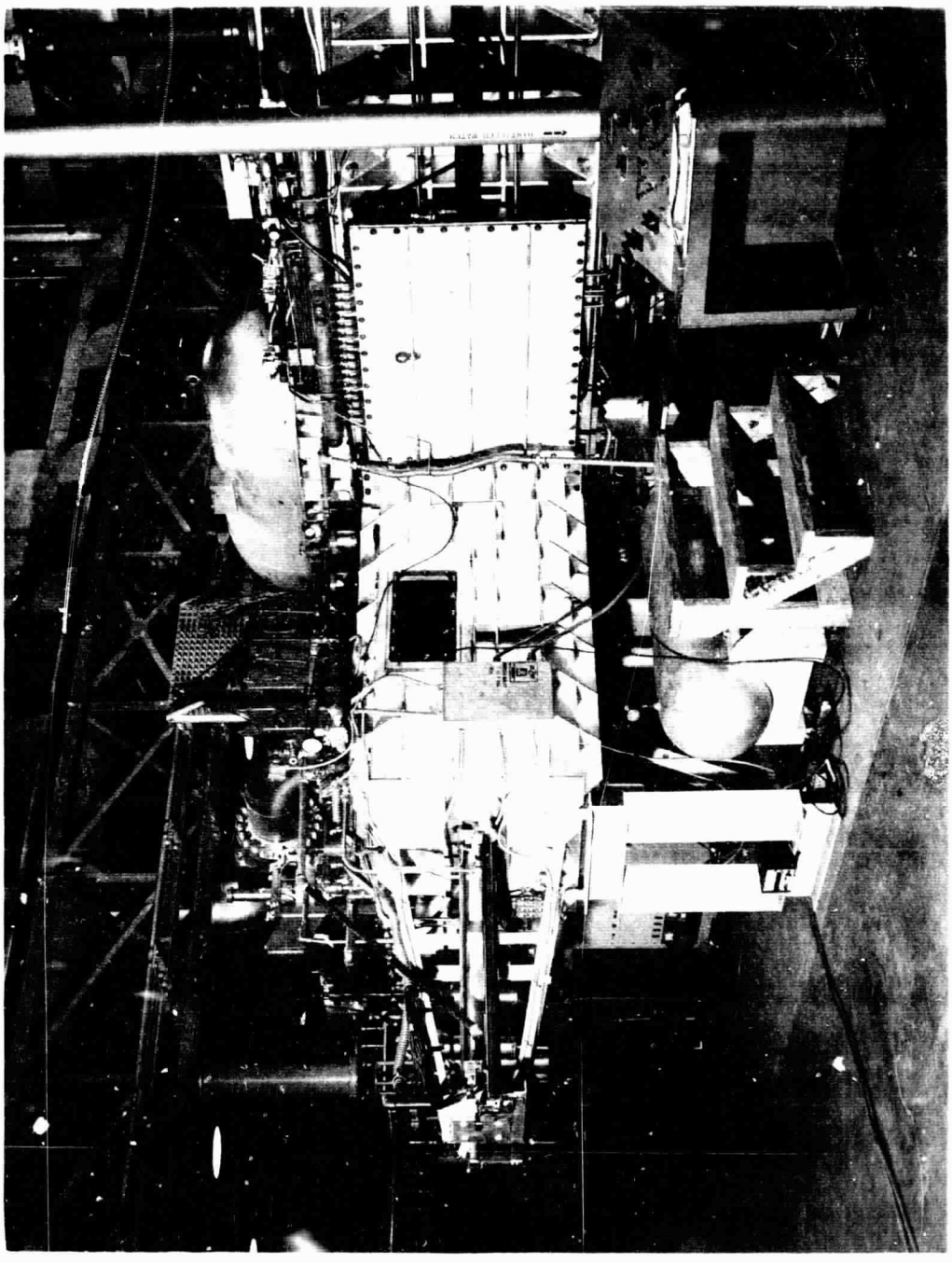

Figure 3.- Injection mechanism.

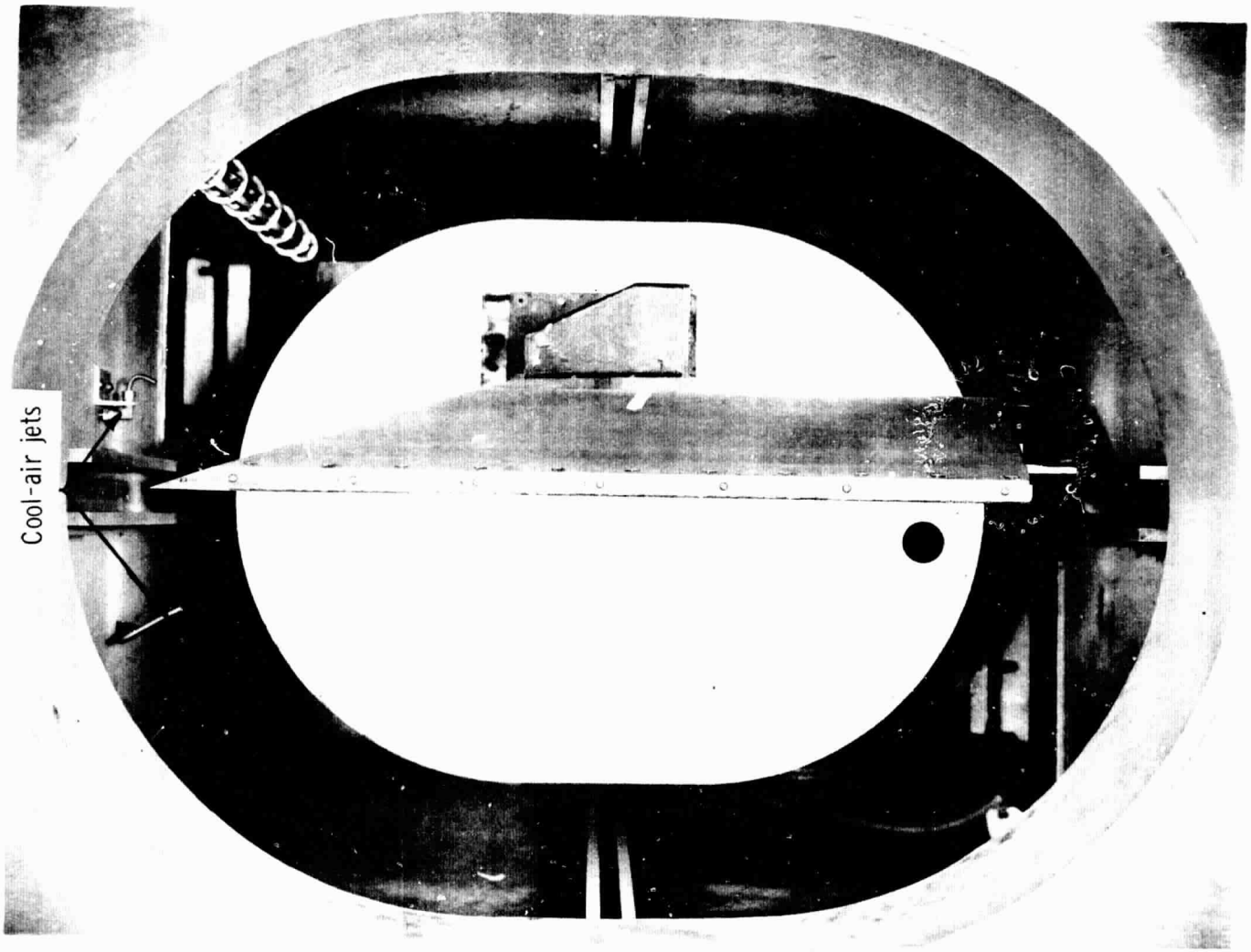

Figure 4.- Model retracted in injection mechanism.

Models

The models for this series of tests consisted of interchangeable plates supported by a model frame and instrumented for heat-transfer measurements and for wall-pressure measurements. The model frame was 29 × 15 inches with a 20° bevel on the sides and leading edge (see Fig. 5). The support strut attached to the top of the frame (orientation of the model was instrumented surface down) and extended to the movable portion of the injection mechanism (see Fig. 5). The strut had a sharp leading edge with a 25° bevel on the upper surface. The instrumentation leads were inside the strut, and the pressure transducers were mounted to the back of the movable portion of the injection mechanism. The instrumented plates were bolted to the model frame around the edges (see row of screws in model photographs, Figs. 4 and 5) and were supported in the interior by longitudinal ribs in the model frame.

The plate instrumented for the measurement of wall pressures was 3/16-inch thick stainless steel. The pressure orifices were 0.070 inch in diameter. The orifice locations are shown in the sketch in Figure 6.

The heat-transfer plate was inconel sheet with a mean thickness of 0.0317 inches. The thickness (t) had a maximum variation of 5 percent and from about 20 inches behind the leading edge to the trailing edge the thickness decreased and was 4 to 5 percent thinner than the mean value.

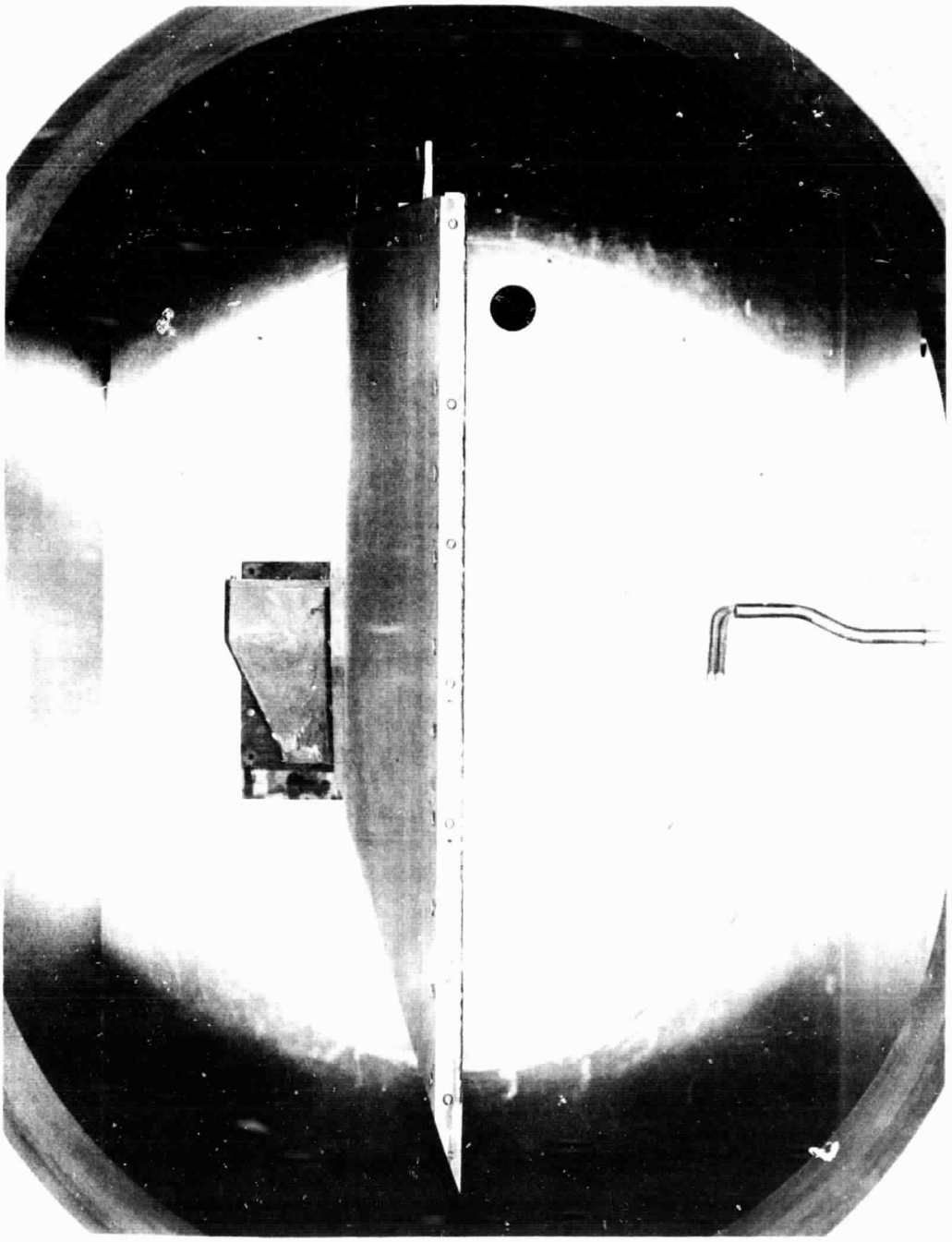

Figure 5.- Model positioned in test section.

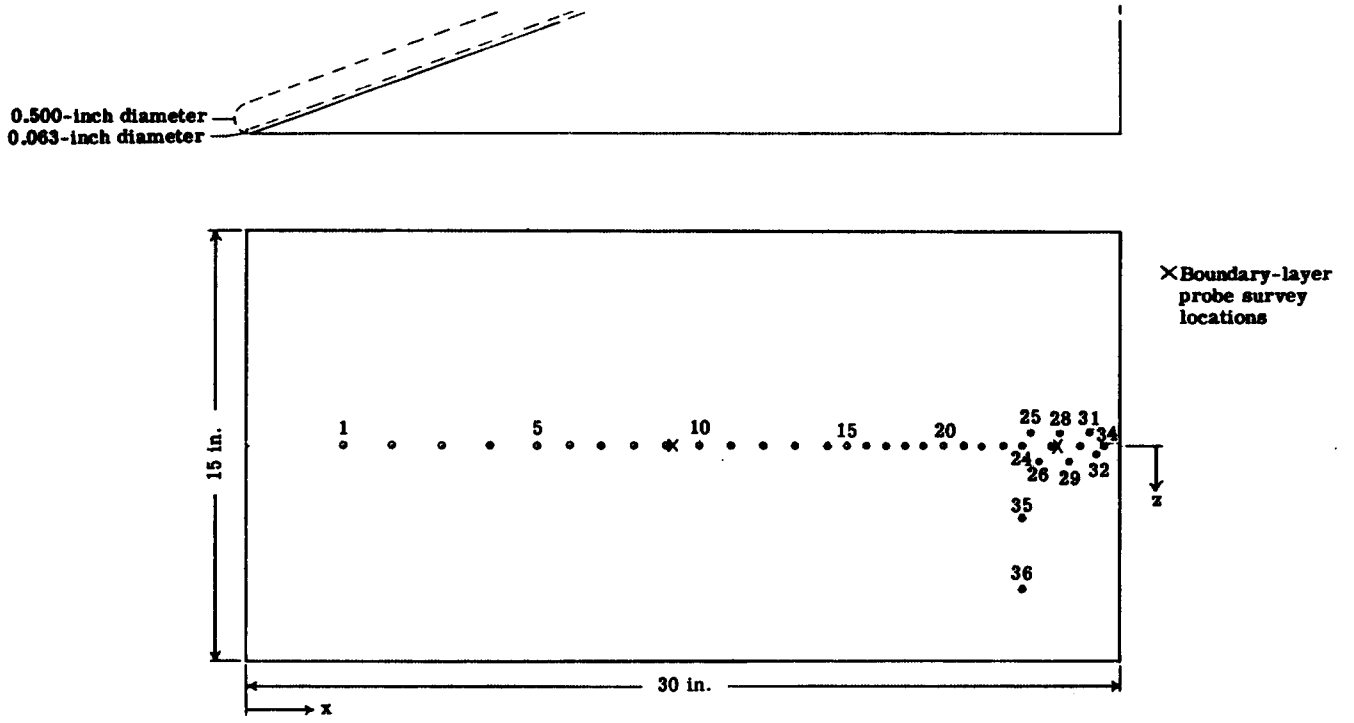

Location of Pressure Tubes													
No.	x	z		No.	x	z		No.	x	z		No.	x	z
1	3.85	0		10	15.55	0		19	23.33	0		28	28.00	+0.50
2	5.52	0		11	16.66	0		20	24.00	0		29	28.33	- .50
3	7.18	0		12	17.77	0		21	24.66	0		30	28.66	0
4	8.85	0		13	18.88	0		22	25.33	0		31	29.00	+ .50
5	10.00	0		14	20.00	0		23	26.00	0		32	29.25	- .25
6	11.11	0		15	20.66	0		24	26.66	0		33	29.50	0
7	12.22	0		16	21.33	0		25	27.00	+ .50		34	29.75	+ .25
8	13.33	0		17	22.00	0		26	27.33	- .50		35	26.66	-2.50
9	14.44	0		18	22.66	0		27	27.66	0		36	26.66	-5.00

Figure 6.- Pressure orifice and boundary layer probe survey locations.

The material properties (density and heat capacity) were not measured for the specific sheet of inconel used in these tests. The values used herein were obtained from manufacturers' literature or other independent studies. A survey of the available information for the material properties revealed the measured values for different samples varied within ±2 percent for the material density and ±4 percent for the heat capacity. Thermocouples (30-gage chromel-alumel wire) were spot-welded to the back side of the plate. The thermocouple locations are shown in Figure 7.

Both the heat-transfer and the pressure plates had solid leading edges which were ground to a 20° bevel with a 0.001 to 0.003 inch leading-edge thickness. The 1/16-inch and 1/2-inch-diameter cylindrical leading edges were attached to the wedge surface. All sharp leading-edge runs were completed first and then the sharp wedge was worked until each cylindrical leading edge fitted with minimum surface discontinuity.

Both the heat-transfer plate and the pressure plates were finished to less than a 32×10^{-6}-inch root-mean-square surface finish. The maximum waviness on the centerline of the surface as detected by a series of dial indicator measurements was 0.33°.

End plates were constructed from 1/8-inch 347 stainless steel for both the heat-transfer and pressure models. The shape (shown in Fig. 7) was generally that of the shock wave for the 0.50-inch-diameter leading-edge model. An arc of 1.25-inch radius formed the nose region

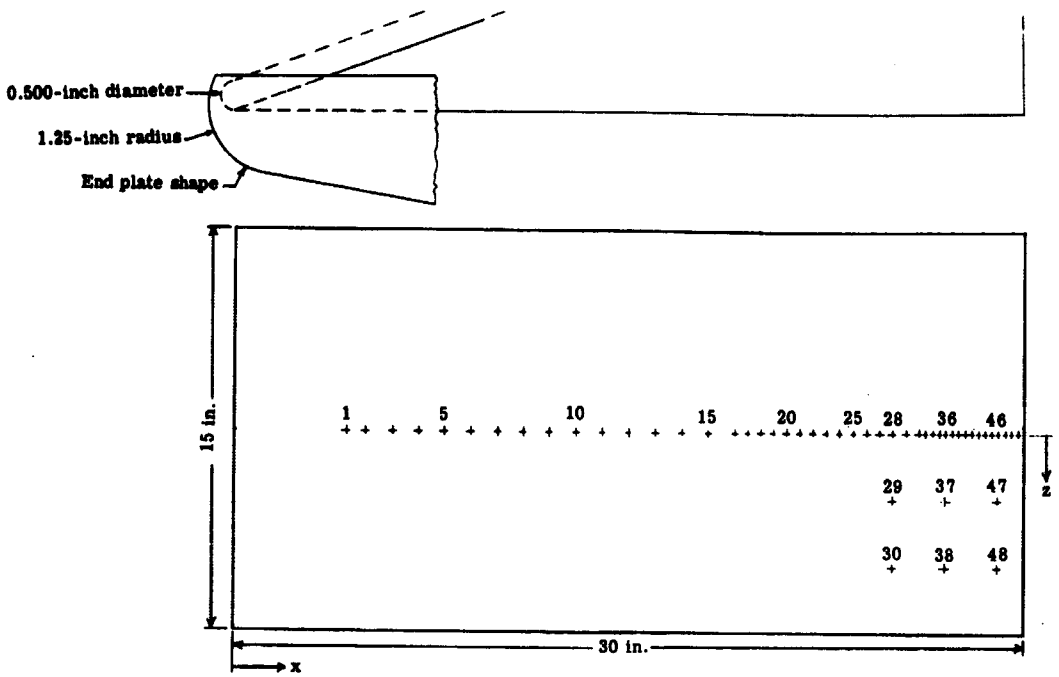

Thermocouple Position												
No.	x	z	No.	x	z	No.	x	z	No.	x	z
1	4.25	0	14	17.00	0	27	24.50	0	40	27.50	0
2	5.00	0	15	18.00	0	28	25.00	0	41	27.75	0
3	6.00	0	16	19.00	0	29	25.00	2.50	42	28.00	0
4	7.00	0	17	19.50	0	30	25.00	5.00	43	28.25	0
5	8.00	0	18	20.00	0	31	25.50	0	44	28.50	0
6	9.00	0	19	20.50	0	32	26.00	0	45	28.75	0
7	10.00	0	20	21.00	0	33	26.25	0	46	29.00	0
8	11.00	0	21	21.50	0	34	26.50	0	47	29.00	2.50
9	12.00	0	22	22.00	0	35	26.75	0	48	29.00	5.00
10	13.00	0	23	22.50	0	36	27.00	0	49	29.25	0
11	14.00	0	24	23.00	0	37	27.00	2.50	50	29.50	0
12	15.00	0	25	23.50	0	38	27.00	5.00	51	29.75	0
13	16.00	0	26	24.00	0	39	27.25	0			

Figure 7.- Thermocouple locations and end plate shape.

(extending 1/4 inch ahead of the model leading edge) with an approximately 8° wedge afterbody. The leading edges of the end plates were sharpened, and the plates were detachable so that the model could be run with or without the end plates.

Boundary-Layer Probes

Two boundary-layer survey probes were constructed for these tests. A sketch of the probe heads is shown in Figure 8. Each probe had three tubes formed from 0.090- by 0.125-inch stainless tubing which was flattened and filed at the tip to form the almost rectangular orifices shown in the sketch. The three tubes were mounted onto a 1/2-inch OD by 3.8-inch ID stainless tube which was air cooled. A 2000°F solder was used to form a smooth transition from the 1/2-inch tube to the smaller tubing and to form a strengthening gusset with a sharp leading edge for the impact pressure tubes (see shaded area of sketch). The measurements of each orifice as obtained with a shop microscope are also presented in Figure 8. Photographs of the probes and the orifices are shown in Figure 9.

There were several facets considered in the probe design. It was desired to obtain the boundary-layer characteristics with a probe of such design that minimum interference occurred. Bradfield, Decoursin, and Blumer (Ref. 16) surveyed a 0.050-inch-thick boundary layer with flattened probes with heights of 0.0025 inch and 0.008 inch and found no interference at $M_\infty = 3.05$. Kendall (Ref. 5) tested flattened probes of 0.010 inch, 0.005 inch, and 0.0025 inch in height in a

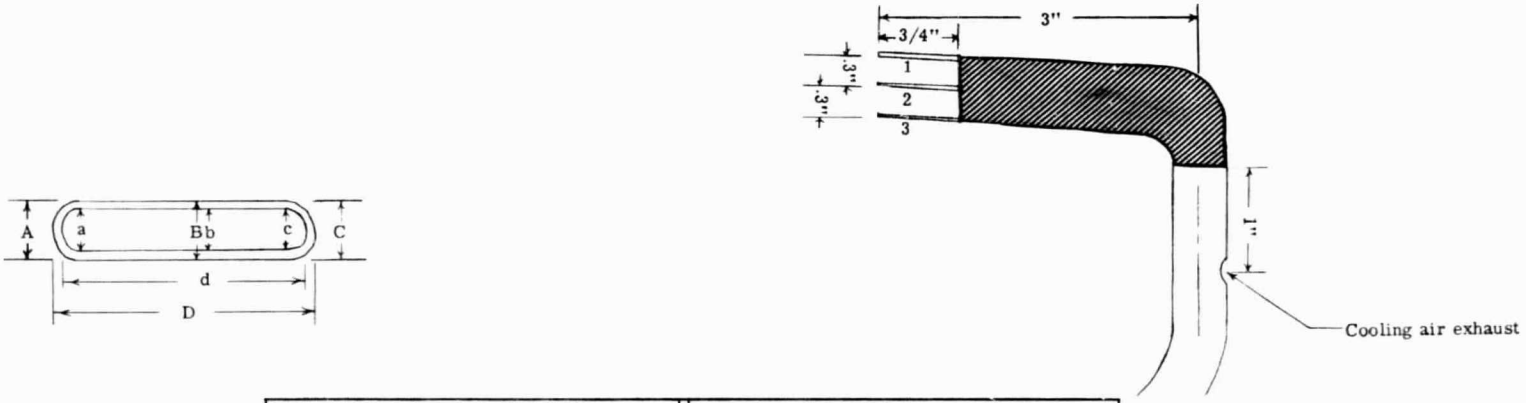

	Probe No. 1				Probe No. 2		
	Tube 1	Tube 2	Tube 3		Tube 1	Tube 2	Tube 3
A	0.020	0.021	0.021	A	0.018	0.021	0.021
a	.013	.001	.012	a	.013	.012	.010
B	.023	.032	.024	B	.020	.021	.022
b	.011	.011	.011	b	.012	.012	.010
C	.020	.020	.022	C	.019	.018	.020
c	.012	.013	.014	c	.013	.011	.009
D	.152	.154	.156	D	.162	.161	.161
d	.136	.139	.140	d	.140	.137	.142

Figure 8.- Sketch of boundary-layer probe heads.

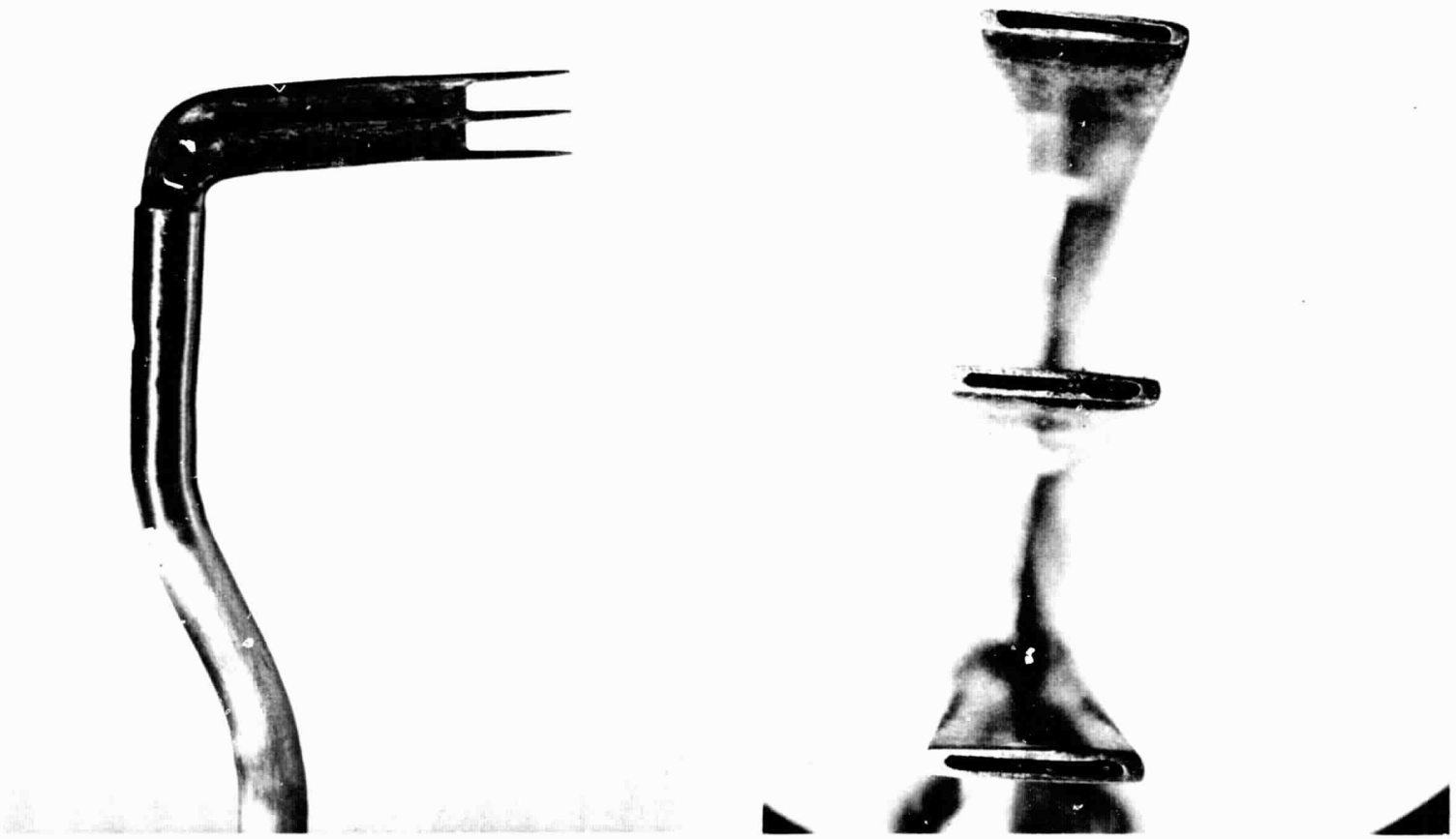

(a) Probe 1.

Figure 9.- Photographs of boundary-layer probe heads.

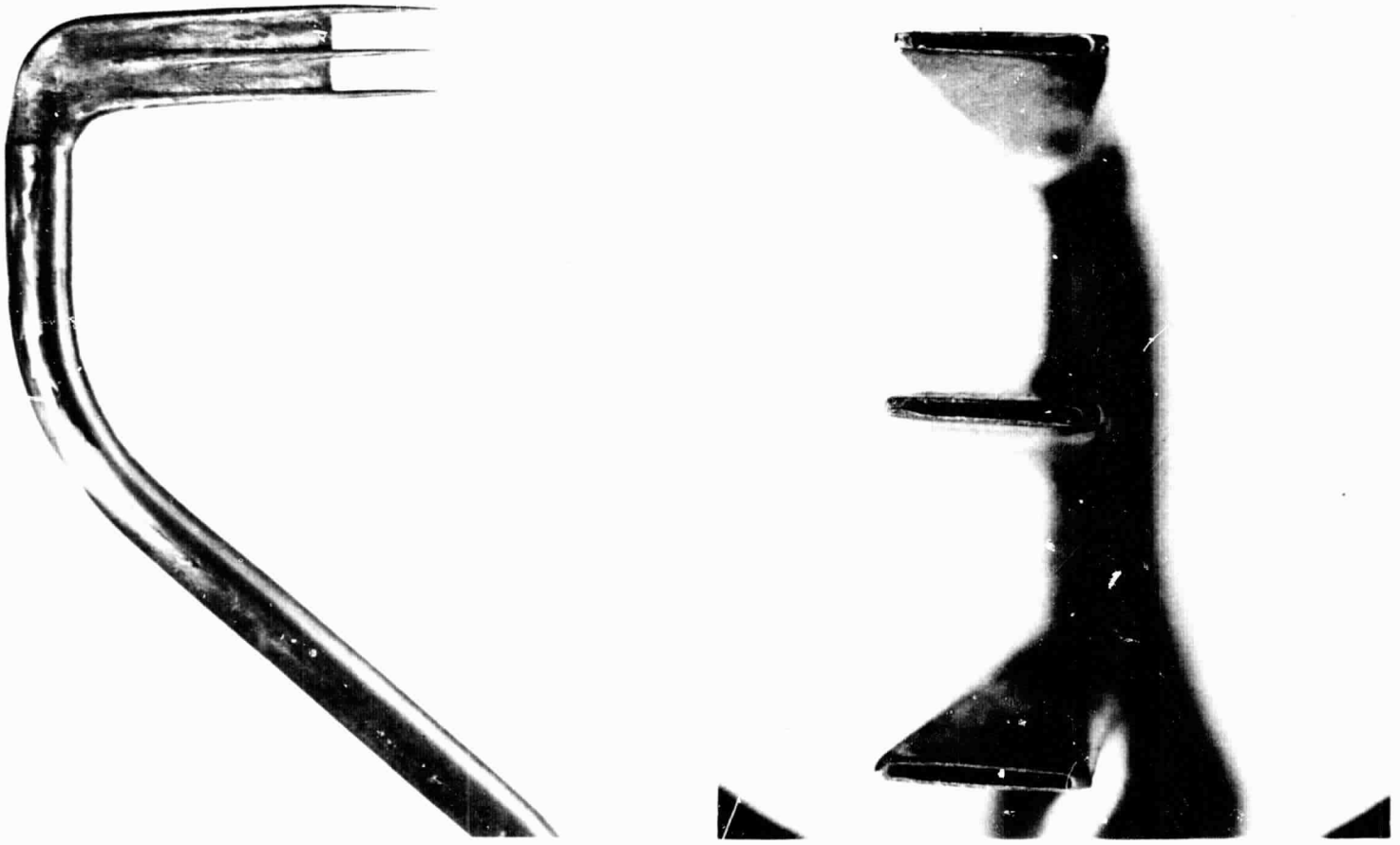

(b) Probe 2.

Figure 9.- Concluded.

0.042-inch-thick laminar boundary layer at $M_\infty = 5.8$. Kendall's surveys show a definite probe interference effect for the 0.010-inch tube and virtually no differences between the surveys with the smaller tubes. Thus from these and other tests an apparently safe criterion for tube height is less than 15 percent of the boundary-layer thickness for no probe interference effect. In the hypersonic boundary layer the density near the wall can be relatively low, and thus the local unit Reynolds number can be very small. Many experimenters have found a resulting "viscous effect" on probe measurements near the wall. MacMillan (Ref. 17) has shown in a very low-speed stream that a flattened tube of a width-to-height ratio of 7 or greater would minimize this effect. Thus the tubes used in these tests were flattened to a width-to-height ratio of approximately 7, and the tube heights were restricted to values less than 15 percent of the expected minimum boundary-layer thickness.

Both probes were mounted on electric motor-driven traversing mechanisms that extended through the tunnel floor. Each mechanism had two 10-turn potentiometer-type slidewires driven by nonslip gears. One slidewire was adjusted to have high sensitivity over a 1-inch travel in the vicinity of the model surface, and the other potentiometer was read over a 7-inch travel. During bench tests of the traversing mechanisms, the probe location always repeated to within 0.003 inch on the high-sensitivity slidewire. The model surface location was determined by a very low voltage fouling circuit. The

probe transducers were mounted on fixtures attached to the traversing mechanism so that no pressure tubing was being moved relative to the transducer during a survey. The orifices of probe 1 traversed along a line perpendicular to the model surface 15 inches behind the sharp leading edge and probe 2 was 28.22 inches from the sharp leading edge. These locations are shown in Figure 6. After each day's run, the probes were inspected for damage, cleaned, and checked for any change in dimension.

Instrumentation and Accuracy

The pressure and temperature data for these tests were automatically recorded on magnetic tape by an analog-to-digital converter.

The stagnation pressures (p_t) were measured by four bonded-wire strain-gage-type transducers with a manufacturer-specified accuracy of ±0.2 percent of full scale. The four transducers varied in pressure range from 0 to 500 psia to 0 to 5000 psia. To obtain the most accurate value for data reduction, the transducer with the lowest pressure range that was on scale was always used. The resultant accuracy for the stagnation-pressure values for these tests, including the recording accuracy, is ±0.85 percent. For each test, all the transducers that were on scale agreed well within the above-stated accuracy.

The tunnel stagnation temperature (T_t) was measured by a chromel-alumel thermocouple located on the centerline of the tunnel

stagnation chamber. This temperature measurement, including the recording error, is considered to be accurate to within ±1.2 percent.

Wall-pressure (p_w) measurements were obtained by three alphatrons. Alphatrons have a radium source that emits alpha particles at a constant rate. This produces ionized gas molecules and results in a current between two electrodes that is proportional to the pressure at a constant temperature. The alphatrons, used for these tests, have two pressure ranges: 0 to 3 torr and 0 to 30 torr (ranges are changed manually on the amplifiers). Prior to testing, the alphatrons were adjusted to have a 45 mv output at the midrange point for each range. A check was then made to ascertain whether the output was linear within a certain band. The instrument was again checked after the tests. The random instrument error plus the recording error results in an accuracy of about 3 percent for pressures greater than 1 torr and 6 percent below about 1 torr. Three 12-port scanning valves were used and thus 3 alphatrons could be employed to measure the pressure at up to 36 orifices. The valves and alphatrons were located just behind the tunnel side wall panel on the injection mechanism. This was done to keep the tube lengths as short as possible and therefore keep response time to a minimum.

The temperature of the back side of the heat-transfer plate (T_w) was measured with 30-gage chromel-alumel glass-insulated thermocouple wire. Each roll of thermocouple wire used is tested and must have an absolute error less than ±2° from 0° to 530°F and

0.38 percent above 530°F. However, to obtain the heat transfer where the time rate of change of temperature is needed, the measuring system repeatability must be considered. The reference junction temperature is maintained at 125°F by a thermostatically-controlled heater. The unit has a maximum variation in the temperature of less than 1° and has a relatively slow variation of temperature with time. The repeatability of the temperatures measured including the repeatability of the high-speed recording system is taken as 1 percent.

Each tube of the boundary-layer probes had several transducers to obtain the most accurate measurement over the range of impact pressures incurred. The following table lists the range of each transducer for each tube.

Tube	Range of transducer, psia
1	0 → 0.58 (alphatron) 0 → 3.0 0 → 10
2	0 → 3.0 0 → 10
3	0 → 10 0 → 50

On tube 1, the alphatron was calibrated and checked in the same way as the wall-pressure alphatrons. The instrument and recording accuracy was ±3 percent of the reading. The transducers were the

unbonded straingage type, and they were calibrated and checked several times before, during, and after the test program. The 0 → 3 psia transducer was a high-precision device with an accuracy of ±0.6 percent of full scale based on experience. The other transducers had manufacturers' stated accuracies of ±1 percent of full scale.

Nozzle Calibration

The tunnel calibration for the tunnel stagnation pressures used for these tests is shown in Figure 10. All of the data shown were obtained from measurement of the stream impact pressure by probes moving on the tunnel vertical centerline and from measurement of the tunnel stagnation chamber pressure. The streamwise position of the probe varied from 12 inches downstream of the leading edge to near the trailing edge of the 30-inch model used in these tests. There was a slight positive streamwise Mach number gradient which appears to be maximum for the lowest tunnel stagnation pressure (about 0.10 per 13 inches). The values of Mach numbers used for these tests were 10.3 for p_t = 350 and 10.4 for p_t = 750 and p_t = 1200 with an accuracy of ±0.10.

Test Conditions

The test stagnation conditions for this study were p_t = 350, 750, 1200 psia with a maximum deviation of ±3.0 psia from the nominal value, and T_t from 1738° to 1873°R. During a given run, T_t varied no more than 14°R. Using the tunnel Mach numbers from the nozzle

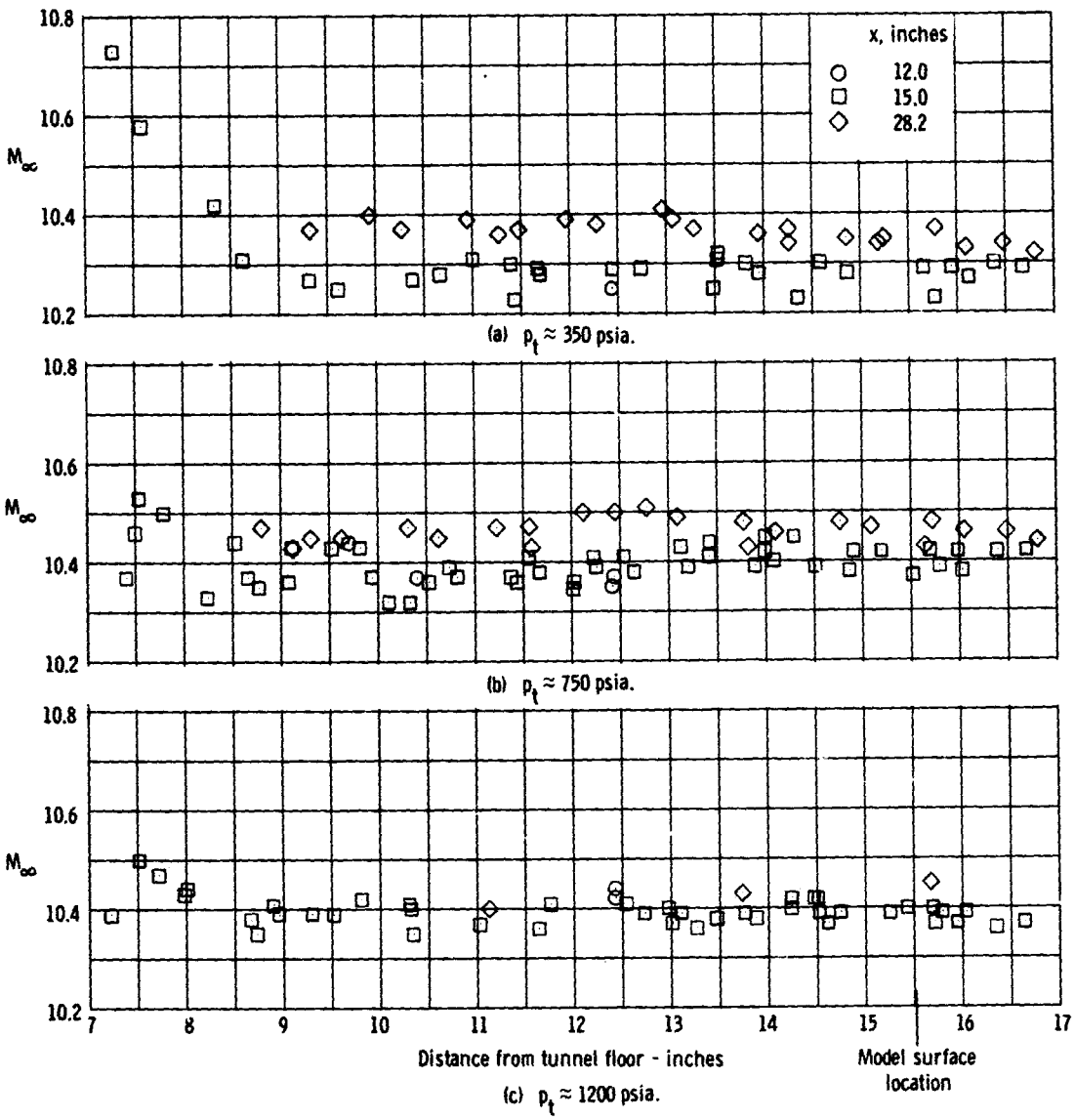

Figure 10.- Tunnel Mach number calibration.

calibration for the above tunnel stagnation pressures, the following ranges free-stream unit Reynolds numbers were obtained.

p_t	M_∞	Range of free stream
psia		Unit Reynolds number per inch (R_∞/x)
350	10.3	0.036×10^6 to 0.042×10^6
750	10.4	0.074×10^6 to 0.088×10^6
1200	10.4	0.12×10^6 to 0.14×10^6

The actual Reynolds number was calculated for each run and used in the data reduction.

The model wall temperature (T_w) varied during each run. For the heat-transfer tests the maximum variation during a run was 8^oF. With an adiabatic wall temperature (T_{aw}) near 1600^o F, this 8^o change is negligible. During boundary-layer survey and wall pressure tests the wall temperature varied by about 100^o F.

The model was maintained parallel to the test section floor for all the tests. Tunnel-flow angularity checks have shown that the flow angularity on the model centerline was between 0.2^o and 0.5^o up onto the model surface.

Test Procedure

Four types of tests were conducted in this study: oil flow, wall pressure, impact pressure surveys, and wall-heat transfer. When the desired test conditions had been established for each test a probe survey of the core of good flow was conducted to obtain the

tunnel Mach number. The model was then rapidly injected into the stream from the sheltered position in the injection mechanism, and the desired data were recorded. During the injection stroke, the model traveled through the tunnel flow in less than one second. Upon completion of the test, the model was withdrawn into the injection mechanism and cooled by air jets (see Fig. 4).

A short series of oil-flow tests was conducted initially to determine which end-plate configuration would provide a more nearly two-dimensional flow over the entire instrumented surface. For these oil-flow tests, just prior to starting the tunnel, a mixture of 10 cs silicon oil and lamp black was dotted on the model surface by a 1/8-inch-diameter felt tip applicator. The oil dots were spaced approximately 1.5 inches apart over the entire length of the model. The tunnel was started, preheated, and test conditions were achieved with the model sheltered in the injection chamber. The tunnel stagnation pressure for these tests was 750 psia, and the model leading edge was sharp. When the model was injected into the tunnel, the development of the oil-flow pattern was watched via a closed circuit television. Once the flow pattern had developed satisfactorily, the model was retracted, and the tunnel was shut down. The oil-flow pattern was recorded by photographing a mirror image of the model surface.

In the wall-pressure tests, after the model was in the tunnel,

a continuous indication of the wall pressure was examined until the pressure instruments had settled out. The pressure reading was then recorded on the magnetic tape, and the scanner valve advanced to the next port. This sequence was repeated until all the pressure orifices had been read.

In the boundary-layer survey tests the scanner valve was set on the port for the orifice under the probe. When the model had come to rest in the tunnel, the impact pressure probe was driven toward the model at a constant speed while data were being recorded every few seconds. The probe speed was sufficiently slow and the volume of tubes 2 and 3 with two transducers each was sufficiently small that lag time for the pressure readings was negligible. When tube 1 was about 0.75 inch from the model surface the probe was stopped, and a continuous plot of the pressure readings was examined until all pressures settled out. From 0.75 inch to the model surface, the probe was moved a few thousandths of an inch at a time, and the pressure readings were allowed to settle out before the data were taken. When the model surface was reached the fouling circuit signaled, and a data point was recorded to establish the surface location on the recorded data. The probe was then removed and the model was retracted. All during the recorded survey of the boundary layer, the probe was moved only in the direction toward the model surface.

Just prior to injection of the model instrumented with thermocouples for the measurement of heat transfer, a system of "continuous" data recording was initiated. This "continuous" data recording system records all data 20 times per second. This mode of recording was continued until five seconds after the model had come to rest in the tunnel at which time the test was terminated.

CHAPTER III

THEORETICAL METHODS

Calculation of Wall-Pressure Distributions

As was discussed in the Introduction, two different approaches must be used to calculate the wall-pressure distribution behind a leading edge of varying thickness. First there is the viscous interaction theory for the sharp leading edge and second the blast-wave theory for the blunt leading edge dominated flow field.

The approximate shock wave shapes for the three leading edges of this investigation are shown in Figure 11. The shock wave shapes for the two blunt leading edges were calculated by the method of Reference 18, whereas the shock wave shape for the sharp leading-edge configuration was measured by Townsend, et. al (Ref. 15) at Mach 10.3. As the figure depicts, the d = 0.50-inch-diameter leading edge gives rise to a strong shock wave with a large pressure jump. The sharp leading-edge configuration, however, has a weaker shock wave which is due to the displacement effect of the boundary layer alone. The theoretical methods of calculating the wall-pressure distributions for the weak shock wave viscous-induced interaction and the strong shock wave bluntness-induced interaction are presented in this section.

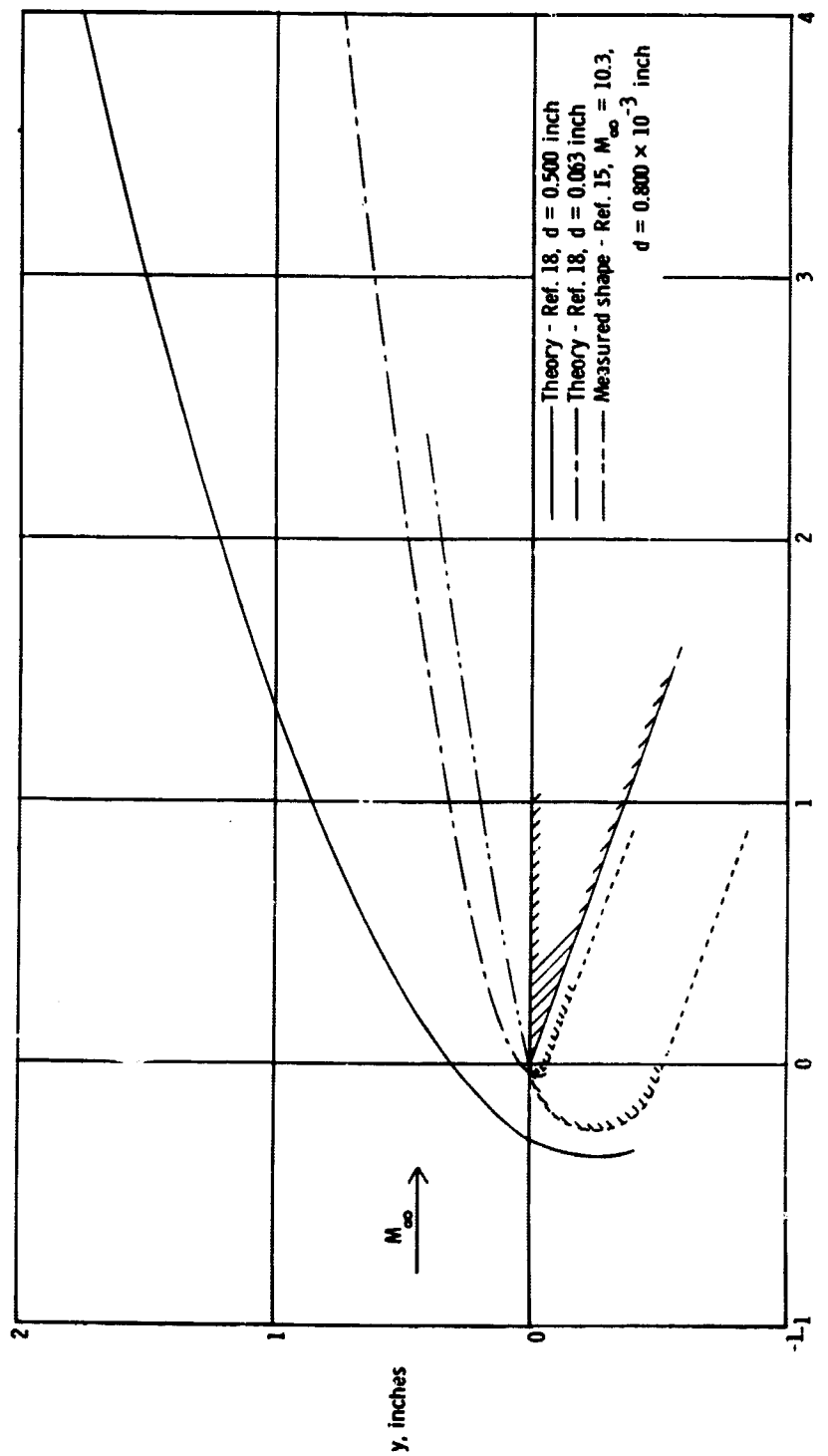

Figure 11.- Shock wave shape for sharp and blunt leading edges.

The theory of Lees and Probstein (Ref. 1) for the prediction of the pressures on a sharp leading-edge flat plate in a hypersonic stream is for the weak interaction regime ($\bar{\chi}_\infty \leq 1$). The measured wall pressures of the sharp leading-edge model in this investigation are in the range of $0.6 \leq \bar{\chi}_\infty \leq 2.9$. Bertram and Blackstock (Ref. 11) developed a method which is more applicable at higher values of $\bar{\chi}_\infty$.

In Reference 11 the following equation for the boundary-layer thickness is obtained from the hypersonic similarity solution of Li and Nagamatsu (Ref. 19).

$$\delta = G K_4\left(\gamma, n, \frac{T_w}{T_t}\right) \frac{M_\infty^2 \sqrt{C_w}}{\sqrt{P_w/P_\infty}} \frac{x}{\sqrt{R_{\infty,x}}} \qquad (1)$$

where

$$G = 1.648 \frac{\gamma-1}{2}\left(\frac{T_w}{T_{aw}} + 0.352\right) \qquad (2)$$

for $N_{Pr} = 0.725$

$$C_w \equiv \frac{\mu_w}{\mu_\infty}\frac{T_\infty}{T_w} \qquad (3)$$

$K_4\left|\gamma, n, \frac{T_w}{T_t}\right|$ is an integral function that is plotted in Reference 11. In this formulation the pressure gradient is postulated to be of the form $p_w \propto x^n$. It is then assumed that the slope of the outer edge of the boundary layer is sufficient to determine the local surface pressures. Differentiating Equation (1) with respect to x and substituting the hypersonic interaction parameter $\bar{\chi}_\infty$, an equation for the hypersonic similarity deflection angle is obtained.

$$K_\delta \equiv M_\infty \frac{d\delta}{dx} = \frac{K_4}{2} \frac{G \bar{\chi}_\infty}{\sqrt{P_w/P_\infty}} \left[1 + \frac{\bar{\chi}_\infty}{2 P_w/P_\infty} \frac{d\left|P_w/P_\infty\right|}{d\,\bar{\chi}_\infty} \right] \qquad (4)$$

For slender two-dimensional bodies in hypersonic flow, the tangent-wedge approximation gives

$$\frac{P_w}{P_\infty} = 1 + \frac{\gamma|\gamma+1|}{4} K_\delta^2 + \gamma K_\delta \sqrt{1 + \left(\frac{\gamma+1}{4} K_\delta\right)^2} \qquad (5)$$

An iterative-type solution of Equations (4) and (5) will give an approximate prediction of the wall-pressure distribution. The reason this method is more applicable at the higher values of $\bar{\chi}_\infty$ is that the full tangent wedge equation is used (5).

Generally in the weak interaction theories a power series for small K_δ is used.

When the flow over a flat plate is dominated by a blunt leading edge, the theory of the decay of intense blast waves presents an analogy that can be used to obtain surface pressures and the shock shape. G. I. Taylor first studied the sudden release of a finite amount of energy at a point resulting in a spherical blast wave. Others (Ref. 3) extended the work to cylindrical and planar blast waves (for summary see Ref. 14). These studies revealed that the law of propagation of an intense blast wave is

$$R = F(\gamma)\left(\frac{E}{\rho_\infty}\right)^{1/3}\tau^{2/3} \qquad |6|$$

for a planar wave. F is an undetermined function of γ, ρ_∞ is the density of the undisturbed gas, τ is the time, and E is constant total energy of the explosion. A blunt flat plate in a hypersonic stream may have a nose drag far greater than the afterbody drag. That is to say, the flow field would be dominated by the blunt leading edge. When this is the case, the energy E can be identified with the nose drag (D). For the blunt flat plate, considering only the surface of interest,

$$E = \frac{D}{2} = \frac{\rho_\infty u_\infty^2 d}{4} C_D \text{ per unit width} \qquad |7|$$

where C_D is the nose-drag coefficient ($C_D = 1.2$ for cylindrical leading edge). Setting $\tau = x/u_\infty$ and substituting Equation (7) into equation (6), the shock shape for the blunt flat plate has the form

$$\frac{R}{d} \propto C_D^{1/3} \left(\frac{x}{d}\right)^{2/3} \qquad (8)$$

In Taylor's model of the blast wave, to be consistent with the functional forms for the pressure, density ratio, and the radial velocity, it is necessary to assume the asymptotic form of the Rankine-Hugoniot relations for a strong shock wave. The pressure ratio across the shock wave must be large $\left| \frac{\gamma - 1}{\gamma + 1} \cdot \frac{p_2}{p_\infty} >> 1 \right|$. Following the development of the theory by Baradell and Bertram (Ref. 14) the shock pressure ratio is

$$\frac{p_2}{p_\infty} = \frac{2\gamma}{\gamma+1} M_\infty^2 \sin^2\theta_s \approx \frac{2\gamma}{\gamma+1} M_\infty^2 \tan^2\theta_s = \frac{2\gamma}{\gamma+1} M_\infty^2 \left(\frac{d(R/d)}{d(x/d)}\right)^2 \qquad (9)$$

where θ_s is the shock-wave inclination with the free stream. Performing the indicated differentiation on Equation (8) and assuming $p_w/p_\infty \approx p_2/p_\infty$, the pressure distribution on a blunt flat plate will have the form

$$\frac{p_w}{p_\infty} \propto M_\infty^2 \left(\frac{C_D}{x/d}\right)^{2/3} \qquad (10)$$

In Reference 14, Baradell and Bertram used a sonic-wedge-characteristics-method calculation to fit Equation (10) to the inviscid pressure distribution. The resulting equation is

$$\frac{P_w}{P_\infty} = 0.187\,\epsilon\left(\sqrt{\gamma}\,(\gamma-1)\,\frac{M_\infty^3\,C_D}{x/d}\right)^{2/3} + 0.74 \qquad (11)$$

where $\epsilon \approx 1-(0.0048/(\gamma-1)^2)$ and is a correction term for γ (see Ref. 11). Also in Reference 14 it was found that the linear addition of the pressure increment due to local surface angle on a curved plate and the blast-wave pressure increment agreed satisfactorily with the characteristic theory. Therefore on the blunt flat plate Bertram and Blackstock (Ref. 11) considered the boundary layer to be growing under the influence of an inviscid (blast wave) pressure gradient. The resulting viscous-induced increment and the bluntness-induced increment were added to obtain the wall pressure. Assuming a weak interaction viscous-induced pressure increment, the resulting equation is

$$\left|\frac{P_w}{P_\infty}\right|_{total} = \left\{0.187\,\epsilon\left[\sqrt{\gamma}(\gamma-1)\,\frac{M_\infty^3\,C_D}{x/d}\right]^{2/3} + 0.74\right\} + \frac{5}{6}\,\frac{\gamma G \bar{X}_\infty}{\sqrt{P_2/P_\infty}} \qquad (12)$$

where the last term is the viscous-induced increment which is a function of $p_2/p_\infty = (p_w/p_\infty)$ blast wave (Equation 11).

Theoretical Boundary-Layer Profiles

It was considered necessary in this study to have a theoretical calculation of the boundary-layer profiles for comparison with some of the measured profiles. A widely known compressible laminar boundary-layer theory is the Van Driest-Crocco method (Ref. 20). Klunker and McLean (Ref. 21) organized an iterative-type solution to the boundary-layer equations. A quick comparison of the Van Driest-Crocco and the Klunker and McLean profiles in the back of each report shows that the results are nearly identical. The Klunker and McLean method is easily programmed on the high-speed computer and therefore has been used in this study.

In the Klunker and McLean method the two-dimensional compressible-flow boundary-layer equations for steady flow, an isothermal wall, and a zero-pressure gradient are solved iteratively. The Blasius similarity variable $\eta = y/x \sqrt{R_{\infty,x}}$ is used to reduce the partial differential equations to ordinary differential equations. The continuity equation can then be solved for (ρu) and integrated by parts. The resulting equation is substituted into the x-momentum and energy equations along with the function $\theta = (h-h_\infty)/(h_e-h_\infty)$. The following pair of differential equations is obtained after nondimensionalizing all flow properties with

respect to the free-stream values.

$$\frac{d}{d\eta}\left(\mu^* \frac{du^*}{d\eta}\right) + \frac{f}{\mu^*}\left(\mu^* \frac{du^*}{d\eta}\right) = 0 \qquad (13)$$

$$\frac{d}{d\eta}\left(\frac{\mu^*}{N_{Pr}^*}\frac{d\theta}{d\eta}\right) + N_{Pr} f \frac{N_{Pr}^*}{\mu^*}\left(\frac{\mu^*}{N_{Pr}^*}\frac{d\theta}{d\eta}\right) = -2 N_{Pr} \mu^* \left(\frac{du^*}{d\eta}\right)^2 \qquad (14)$$

where

$$f = \frac{1}{2}\int_0^{\eta} \rho^* u^* d\eta$$

All the coefficients in the above equations are functions of η. However, an initial solution can be used to evaluate these coefficients and then by the method of successive approximations a solution is readily obtained since the approximations converge rapidly. The equations with constant coefficients are solved by integrating factors.

The Klunker and McLean solution has been programmed on the high-speed digital computer. In the computer program the successive approximations were continued until the change between two successive approximations was less than ±0.05 percent.

Whenever gas properties were needed in the calculations in the

program, tables of thermodynamic properties of air were used. The enthalpy table from the N.B.S. tables (Ref. 22) was used to determine the temperature distribution from the calculated enthalpy distribution. The Mach number was calculated using a table for the speed of sound. The impact-pressure distribution was calculated using the perfect gas Rayleigh-pitot equation. Chart 17 of Reference 23 reveals that any imperfect gas effects on this equation are less than 0.5 percent for the range of conditions occurring in this investigation. The Prandtl number was also taken from a table in Reference 22.

Ordinarily, viscosity is considered to be independent of the pressure level. However, at low pressures, the viscous drag at a surface has been found to decrease due to the slip flow of gas layers over adjacent surfaces. Figure 2 in Reference 24 shows that at a pressure of 1 torr the decrease with pressure of the viscous drag is just starting and increases with increasing temperature. Grieser and Goldthwaite (Ref. 25) undertook a careful study at low temperatures and over a range of pressures. From th measurements, the best equation fit to the data at atmospheric pressure was

$$\mu = 0.022091 \frac{T^{3/2}}{T + 178.6} \times 10^{-6} \frac{lb\text{-}sec}{ft^2} \qquad (15)$$

over the temperature range of 144°R to 530°R. This equation is plotted in Figure 12 along with the low-temperature Sutherland formula. Grieser and Goldthwaite also determined the accommodation parameter

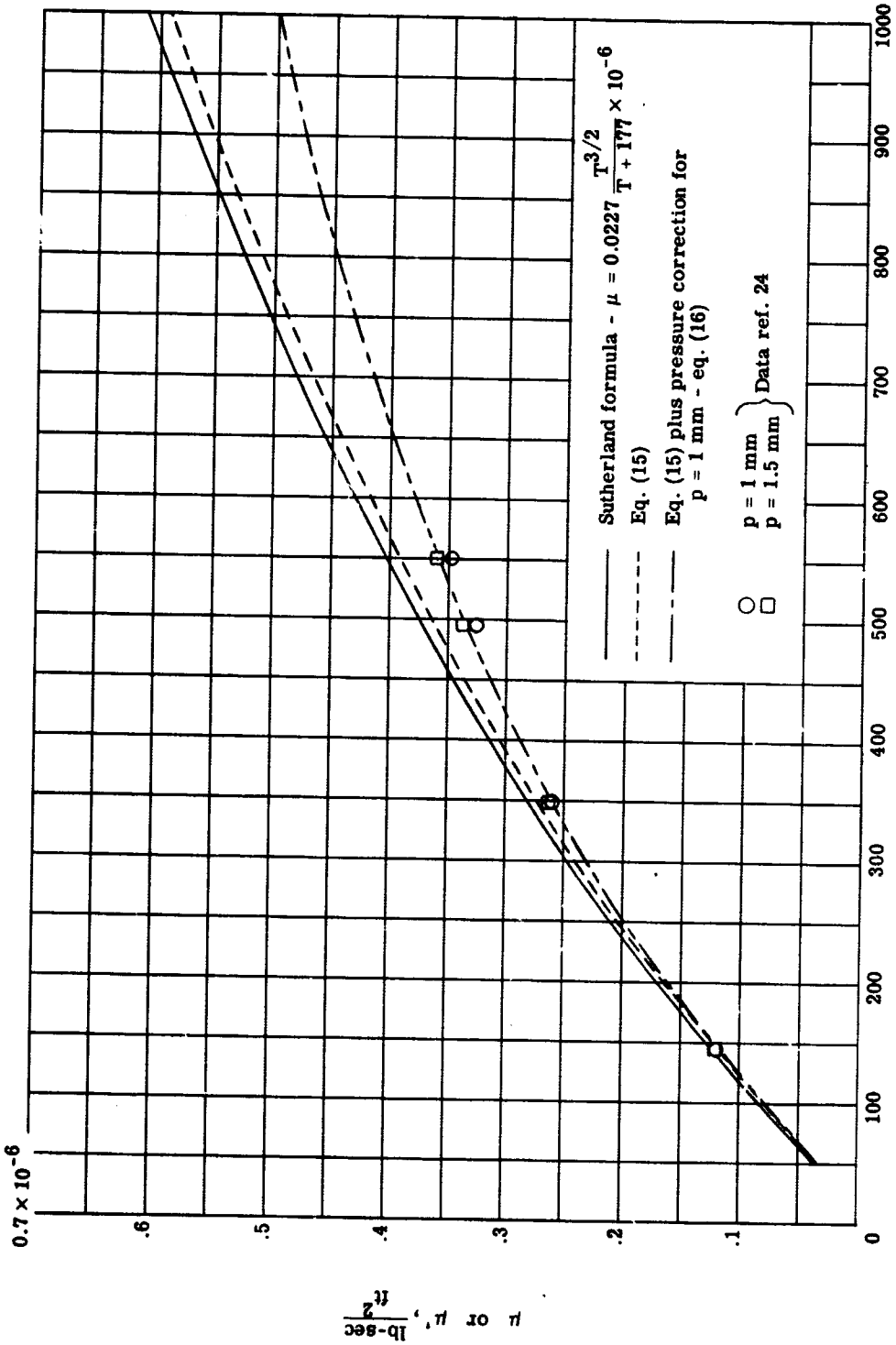

Figure 12.- Viscosity of air.

"a" for the low-pressure data to be used in the Kurdt and Warburg equation for the apparent viscosity μ'. The equation is

$$\mu' = \frac{\mu P}{P + a\mu} \qquad (16)$$

A curve for μ' for a pressure of 1 mm of mercury is also shown in the figure using the Grieser and Goldthwaite value of a. Also shown in the figure are some data obtained by Johnston and others (Ref. 24) at 1.C and 1.5 torr. The data and correlation agree within 3.3 percent. This correlation was used in the program to calculate the viscosity.

Calculation of Skin Friction and Heat Transfer

Bertram and Feller (Ref. 9) showed that under certain assumptions the ratios of local values of either skin-friction, heat-transfer, or boundary-layer thickness to the corresponding zero-pressure gradient values are proportional to the square root of the pressure ratio. These proportionalities were drawn from the work of Li and Nagamatsu (Ref. 19). The required assumptions are a hypersonic Mach number at the boundary-layer edge with the velocity nearly constant, linear viscosity-temperature relation, $p_w \propto x^n$, Prandtl number 1, and isothermal wall. The constants of proportionality depend on the value of n and the wall temperature. Bertram and Feller (Ref. 9) present plots to determine the constants.

CHAPTER IV

DATA REDUCTION

Pressure Measurements

All pressure measurements were converted to the desired units on the high-speed digital computer by use of the experimentally determined calibrations. The impact-pressure probe locations were determined by use of the slide-wire calibrations and a zero location determined from the fouling circuit.

Free-Stream Quantities

The free-stream Mach number was calculated from the probe measurements of free-stream impact pressure and the stagnation chamber pressure. The ratio of these measured pressures along with the "Ames Tables" (Ref. 23) for an ideal gas were used in conjunction with a set of correction curves. The correction curves were derived from the report on the thermodynamic properties of equilibrium air by Erickson and Creekmore (Ref. 25) and account for imperfect gas effects.

The stream quantities (p_∞, T_∞, and u_∞) were calculated from the Mach number, the "Ames Tables" and the correction curves. The free-stream viscosity μ_∞ was calculated from Equation (15) of the theoretical methods chapter.

Boundary-Layer Profiles

To compute the velocity profile from the measured impact-pressure data in the boundary layer, it was necessary to assume that the static pressure across the boundary layer was equal to the measured wall pressure. The Rayleigh-pitot equation was then used to calculate a Mach number profile. The imperfect gas effects on the Mach number value are less than 0.5 percent using this equation. The theoretical total enthalpy distribution (h_t) from the Klunker and McLean theory was available in the computer from the calculation of the theoretical profiles. Then, using the one-dimensional adiabatic energy equation,

$$h_t = h + \frac{M^2 a^2}{2} \qquad (17)$$

the local static enthalpy (h), the speed of sound (a), and the local static temperature were determined; h and a are functions of temperature only and were available from the N.B.S. air tables (Ref. 22) stored in the computer memory.

The local skin friction (C_f) was obtained by plotting the resulting velocity profiles and graphically determining the slope of the tangent at the wall.

$$C_f = \frac{\mu'_w \left|\frac{\partial u}{\partial y}\right|_w}{\frac{1}{2}\rho_\infty u_\infty^2} \qquad (18)$$

Reduction of Heat-Transfer Data

The rapid injection of the "thin skin" model provides a sudden exposure to a heating environment. The heat transfer to the model is determined by measuring the change with time (τ) of the internal energy of the skin. The equation used for the calculation of the heat transfer is

$$\dot{q}_A = C_m \rho_m t \frac{dT_w}{d\tau} \qquad (19)$$

where C_m is the heat capacity of the inconel sheet determined from the equation

$$C_m = 0.0000611 (T_w - 460) + 0.098 \frac{BTU}{lbm\,^\circ R} \qquad (20)$$

ρ_m is the material density = 525.312 lb/ft^3, and t is the plate thickness.

A machine program of the method of least squares was used to fit a second-degree polynomial to the temperature data at each location in a 2-second interval. At the middle of the interval, the slope of the polynomial was determined and was used in Equation (19).

The adiabatic wall temperature (T_{aw}) was calculated from the equation

$$T_{aw} = r(T_t - T_\infty) + T_\infty \qquad (21)$$

where the recovery factor r was assumed to be $\sqrt{N_{Pr}} = \sqrt{0.72}$. For the purposes of this study, the heat-transfer coefficient was defined as $\bar{h} = \frac{q_A}{T_{aw} - T_w}$, and the Stanton number is then $N_{ST} = \frac{\bar{h}}{\infty u_\infty C_p}$ where C_p was assumed to be 0.24 Btu/lbm °R.

CHAPTER V

DISCUSSION OF RESULTS

Oil-Flow Tests

A short series of oil-flow tests was conducted initially to determine what end plate configuration would provide a two-dimensional flow in the area of interest on the instrumented surface of the model. A series of photographs of the mirror image of the oil-flow patterns are shown in Figure 13. Since the instrumented surface of the model was in a plane perpendicular to the tunnel windows, after each oil-flow test a mirror was placed in the tunnel to obtain an image that could be recorded by photography.

Because of lighting problems, the camera was in a different location and at a different angle relative to the mirror for the shots of the front and rear portions of the model. This is the reason for the skew appearance and varying model image size. To relate the front and rear portion photographs, the model centerline is noted and the corresponding locations in the two photographs are indicated.

The oil-flow pattern without the end plates installed is presented in Figure 13(a). A severe cross flow is observed to intersect the model surface at approximately the model midlength and feed across the model toward the centerline. The origin of the cross flow is the mounting strut.

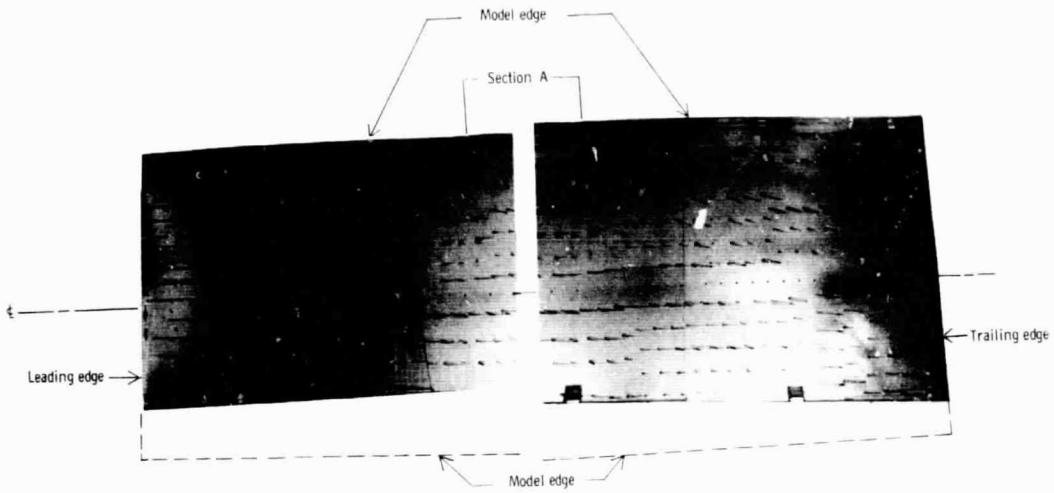

(a) Without end plates.

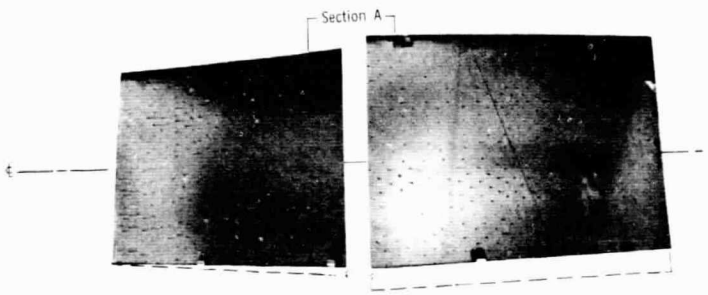

(b) With end plates.

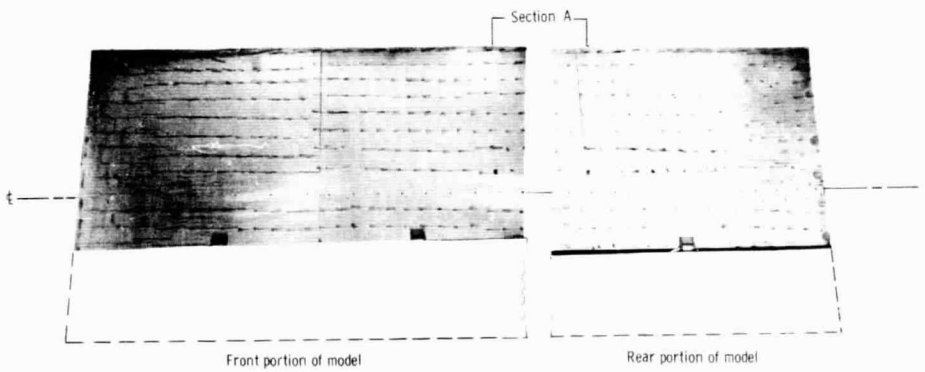

(c) With strut shield.

Figure 13.- Oil-flow patterns.

The oil-flow pattern with end plates installed (Fig. 13(b)) did not flow properly since many of the oil dots were too small. The existing pattern does show, however, that the severe cross flow is not present on the surface. However, a slight inward flow is seen along the model edge (near the end plate) especially very near the leading edge.

Still another configuration was tried with one end plate installed on the far side of the model and extending upward at an angle of 30° to the plane of the model surface. In this configuration, the end plate shielded the model surface from the interference field of the strut. The resulting oil pattern (Fig. 13(c)) shows an inward flow near the leading edge on the far side which is quickly damped out. For the rest of the model length, the flow near the edge is outward off the plate surface. All of the disturbed flow occurs along the far row of oil dots. The oil dots on the near side of the model (not shown in the photographs) showed a pattern similar to that of the far side. The flow near the center of the plate was parallel.

On the basis of these results the configuration of one end plate directed upward on the far side shielding the plate from the strut interference field was used throughout the pressure and heat-transfer tests. It is believed also that the flow along the model centerline is two-dimensional and is representative of the flow over an infinitely-wide flat plate.

Pressure Distributions

The bluntness effect on the wall-pressure distribution is shown in Figure 14 where p_w/p_∞ along the model centerline is plotted as a function of x for three unit Reynolds numbers. The overall accuracy of these data is believed to be ±9 percent (6-percent transducer accuracy and 7 percent due to the tunnel Mach number accuracy).

The modified blast wave theory of Bertram and Blackstock (Eqns. 11 and 12) is generally in good agreement with the pressures behind the 0.50-inch-diameter leading edge where the bluntness-induced effects are dominant. The 0.063-inch-diameter leading-edge data are slightly below the sharp leading-edge data for the lowest unit Reynolds number case, but as the unit Reynolds number is increased, the two sets of data draw closer together and cross at the highest unit Reynolds number. The viscous-induced pressure rise decreases as the unit Reynolds number increases because of boundary-layer thinning, whereas, the bluntness-induced pressure rise, blast-wave effect, is insensitive to unit Reynolds number. Thus, the data suggest that at the lowest unit Reynolds number, the viscous-induced pressure rise on the sharp leading-edge model is greater than the combined pressure rise due to bluntness and any boundary-layer displacement effect on the 0.063-inch-diameter leading-edge model between 93 and 469 diameters from the leading edge. The data appearing in References 7, 8, 13, and 15 show that generally slight leading-edge bluntness increases the surface

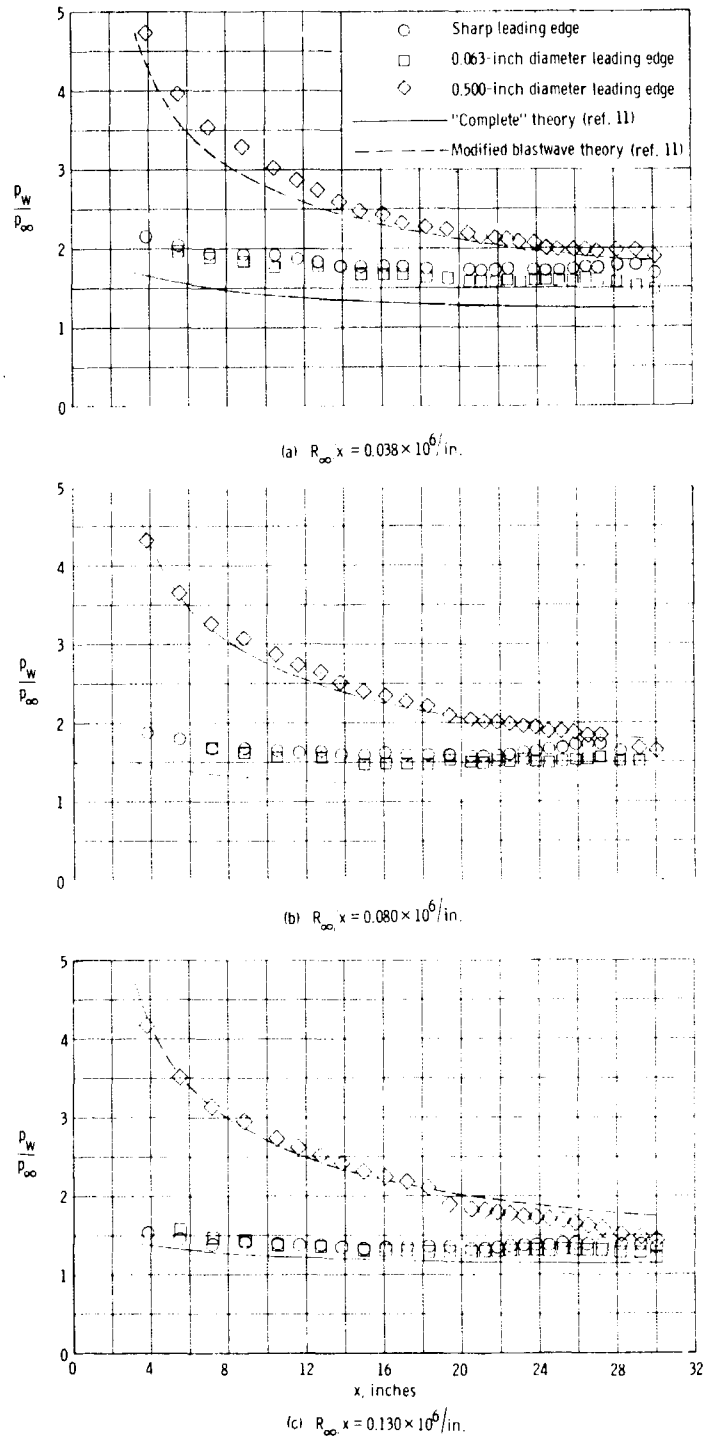

Figure 14.- Bluntness effects on wall pressure distributions.

pressures, but none of these references have much data in the range of the present data $\left(\frac{x}{d} \geq 93 \text{ and } 2400 \leq R_{\infty_d} \leq 8200\right)$.

A comparison of the sharp leading-edge wall-pressure distributions with the Bertram and Blackstock theory (Eqns. 4 and 5) for predicting viscous-induced pressures is also shown in Figure 14. This theory is below the data at all Reynolds numbers with the largest difference being about 25 percent at the lowest unit Reynolds number.

The slight tunnel flow angularity discussed in the Test Conditions section of Chapter II may account for between five and twelve percent of this difference; however, the greater part of the difference is unexplained.

The sharp and 0.063-inch-diameter leading-edge model pressure distributions tend to increase slightly on the rear 1/3 of the model, but the oil-flow patterns and the lateral pressure distributions did not indicate any model edge effects in this region. There does appear to be a model trailing-edge effect over the last two inches of the model.

Impact-Pressure Profiles

The results of the impact-pressure surveys for the sharp leading-edge model and the three test unit Reynolds numbers are shown in Figure 15. Near the wall the data shows the large impact-pressure gradient typical of the laminar boundary layer. Outside of this region, the impact-pressure ratio for the front probe (see Fig. 15(a))

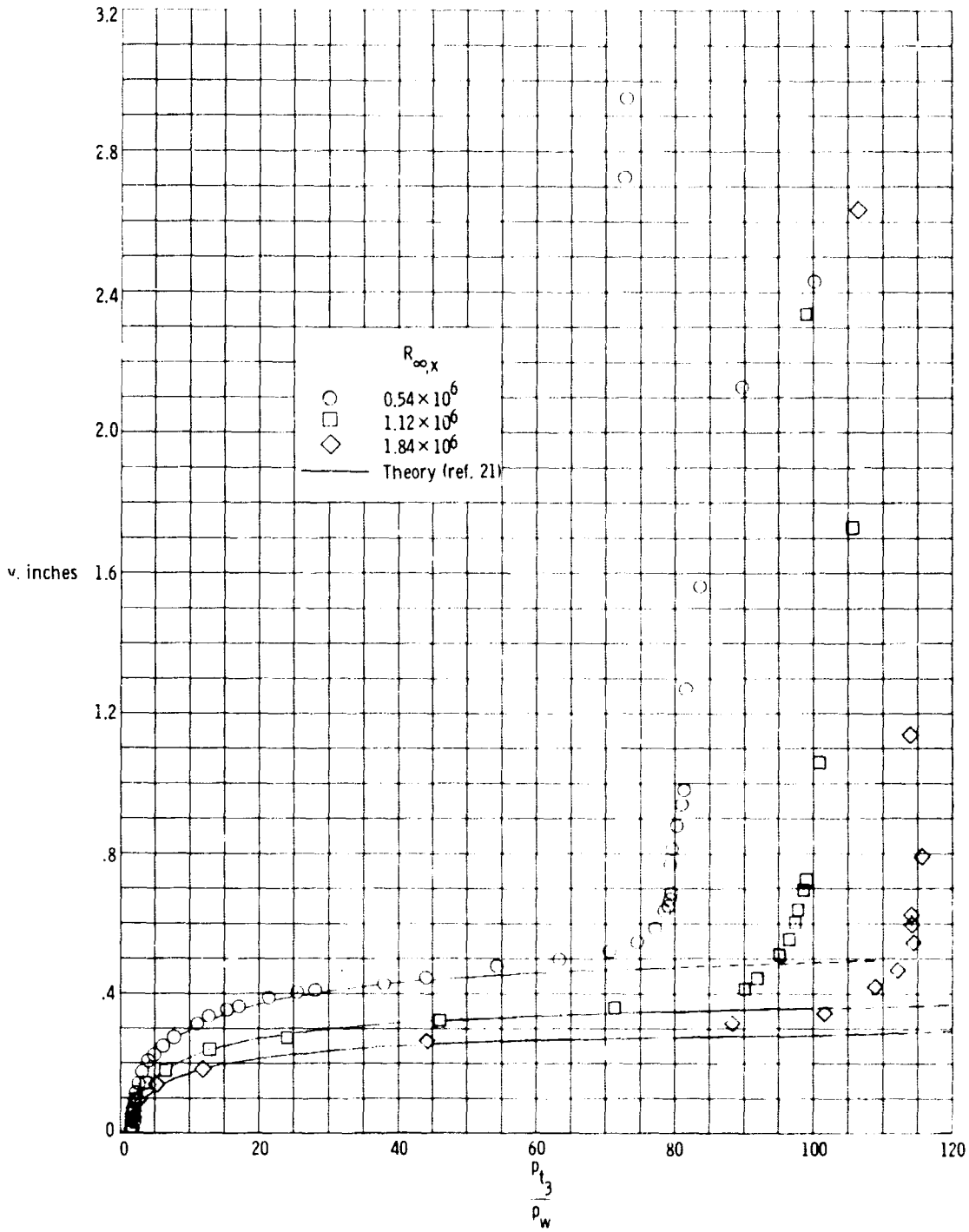

(a) x = 15.0 inches.

Figure 15.- Impact pressure profile for sharp leading-edge model (d = 0.002 inch).

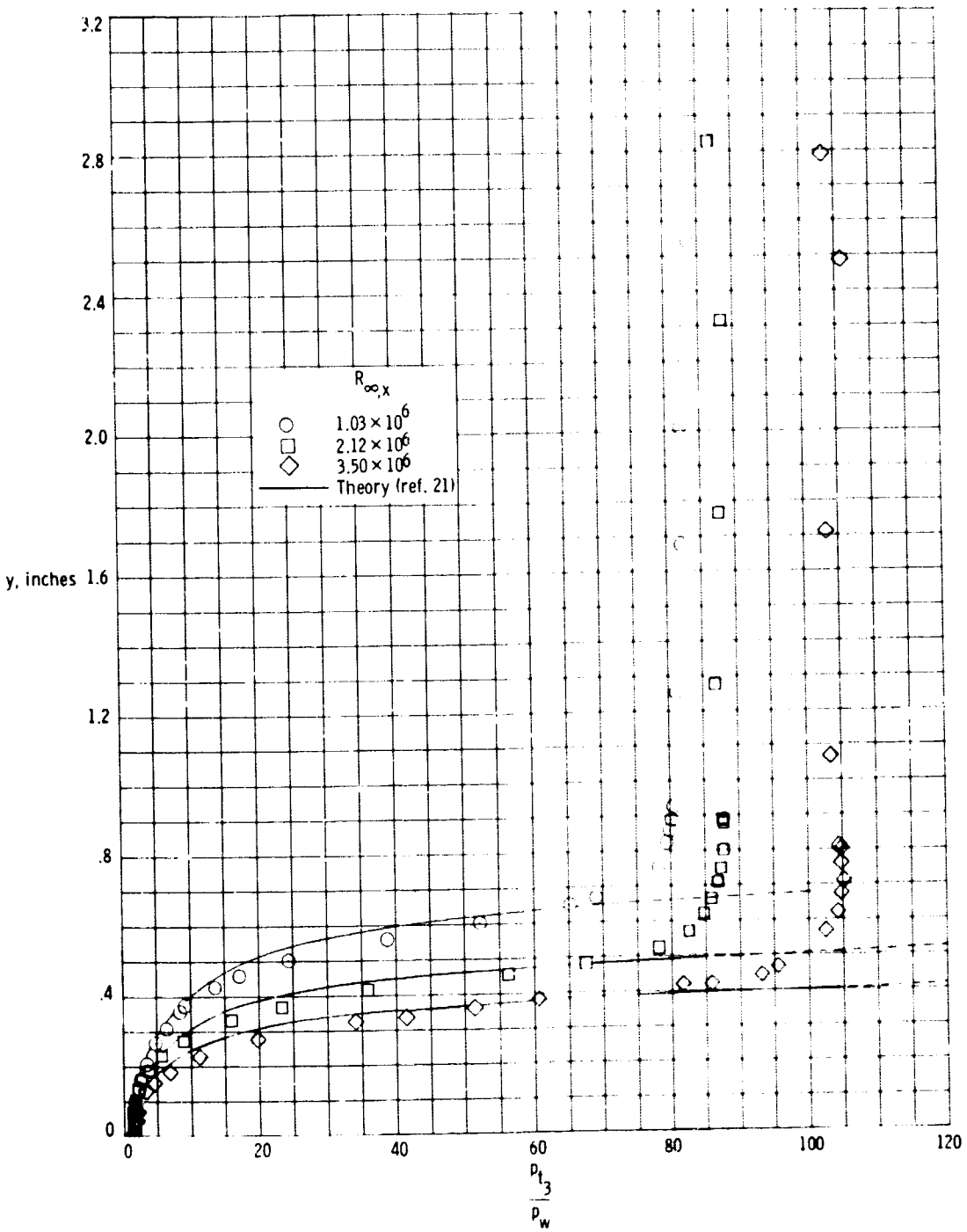

(b) x = 28.2 inches.

Figure 15.- Concluded.

increases as the probe approaches the shock wave (in particular the $R_{o,x} = 0.54 \times 10^6$ data). For $y = 2.72$ and beyond, the probe was outside of the leading-edge shock wave and measured the free-stream impact pressure.

Since several different range transducers were used to obtain each profile, the accuracy of the data across the boundary layer will vary. The maximum accuracy for the pressure ratio was within ±7 percent. The accuracy in the probe location measurement is within ±0.004 inch from the model surface to $y = 1.0$ inch and ±0.01 inch beyond. The pressure ratio (p_{t_3}/p_w) at the wall should be 1; however, as the probe approaches the wall, the data approach a value of about 1.5. This is due to viscous effects which are indicated by a very low local Reynolds number based on orifice height and wall-probe interference. The viscous effects were studied by MacMillan and are referred to in the boundary-layer probe section of Chapter II. No attempt has been made to correct these data using MacMillan's work due to the differences in the test conditions and other unknown effects such as wall probe interference. These data near the wall are very evident on the velocity profile plots and this matter will be considered in the velocity profile discussion. These data must therefore be recognized as being subject to the above-mentioned conditions and should not be used in evaluating boundary layers.

Figure 15 shows that the Klunker and McLean boundary-layer theory (Ref. 21 (see Chapter III)) based on free-stream conditions adequately

predicts the measured impact pressure profiles from the wall out to the region of nearly constant impact pressure. Outside the boundary layer on a sharp leading edge model with a nearly straight shock, the impact pressure is fairly constant; thus, while the boundary-layer edge is difficult to establish from the impact-pressure profiles, the start of this region of constant impact pressure must be in the vicinity of the boundary-layer edge. As was stated in Chapter III, the Klunker and McLean theory assumes the wall pressure is constant. However, the sharp leading-edge model has a small pressure gradient (Fig. 14). Nevertheless, the theory based on free-stream conditions (M_∞ = 10.4) is in good agreement with the impact-pressure profiles in the boundary layer. The probe measurements indicate a rather substantial change in Mach number from the free-stream value of 10.4 to the boundary-layer edge values of 7.82 to 9.39. Hayes and Probstein (Refs. 27 and 28) demonstrated the existence of an independence principle for hypersonic boundary layers. In essence, this principle says that for given wall-pressure and wall-temperature distributions and a given (and nearly constant) boundary-layer edge velocity, the solution or profiles in the principal part of the boundary layer (the whole boundary layer except for the extreme outer edge) are independent of the boundary-layer edge Mach number. The requirements for this principle to apply are a perfect gas and hypersonic flow outside of the boundary layer. Apparently in the present test conditions, the wall-pressure gradient is sufficiently small and the boundary-layer

edge velocity is sufficiently close to the free-stream value that the zero-pressure gradient theory of Klunker and McLean is an accurate solution in the principal part of the boundary layer behind the sharp leading edge.

The impact-pressure profiles for the 0.063-inch-diameter leading-edge model are presented in Figure 16. A theoretical profile resulting from the Klunker and McLean boundary-layer theory for a sharp leading-edge model is also presented. The blunt leading-edge data do not have as large an impact-pressure gradient as the sharp leading-edge profiles. The outermost data points 28.22 inches behind the blunt leading edge (Fig. 16(b)) show an extended region of slightly varying impact pressure. This is as compared to approximately 2 inches of constant impact pressure the same distance behind the sharp leading edge (Fig. 15(b)).

It is impossible to determine a boundary-layer edge from the impact-pressure profiles for the 0.063-inch-diameter leading-edge model. However, the data for $p_{t_3}/p_w > 35$ in the nearly linear portion of these profiles are hypersonic. Therefore, it may be argued that the profiles should compare with the sharp leading-edge profiles according to the previously stated independence principle. However, Hayes and Probstein (Ref. 27) conclude that similitude may not be extended to the viscous-flow regime for a blunt body since at the nose the inviscid flow is far from hypersonic (local velocity perturbations are large), and results in an entropy layer adjacent to the body.

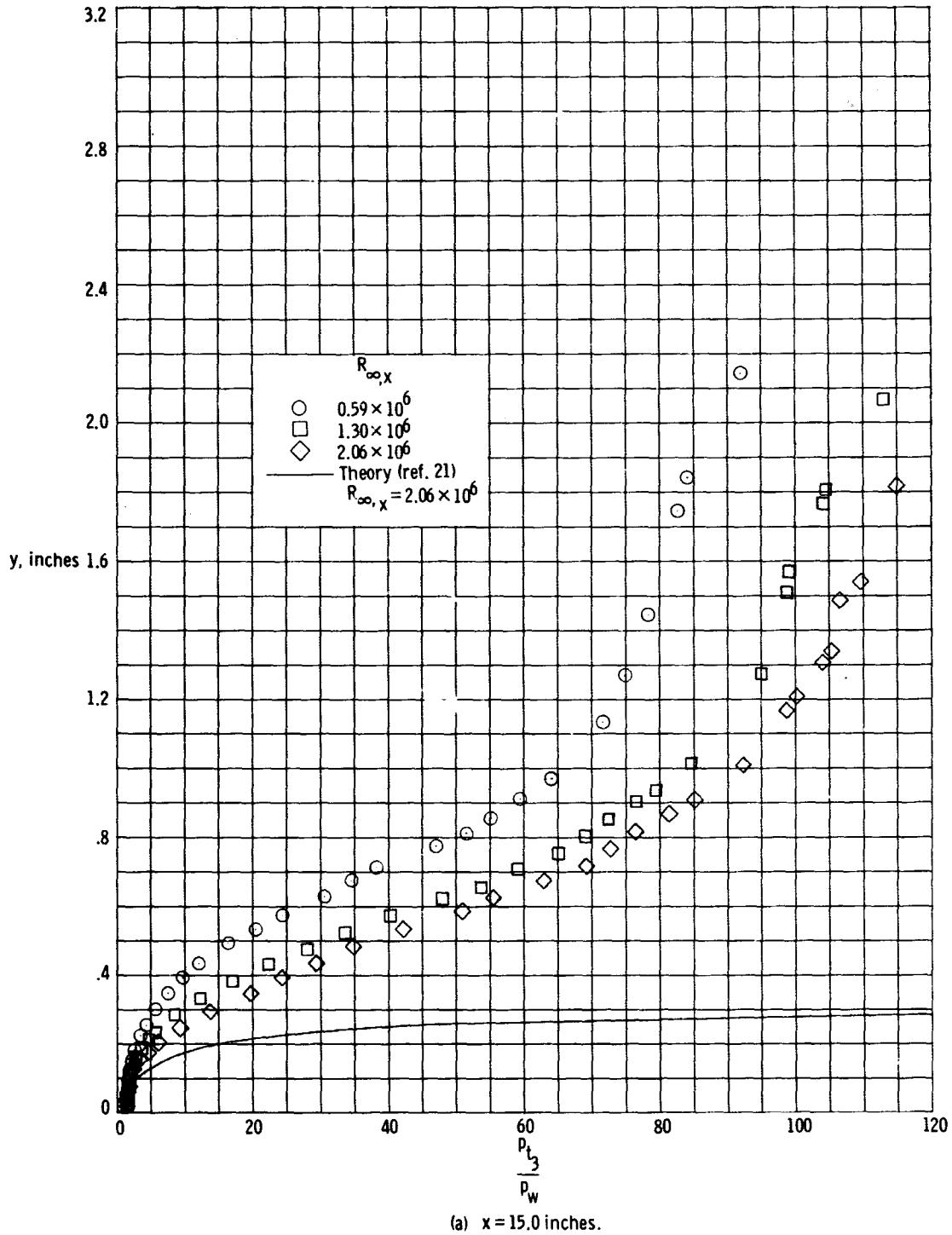

(a) x = 15.0 inches.

Figure 16.- Impact pressure profiles for d = 0.063-inch model.

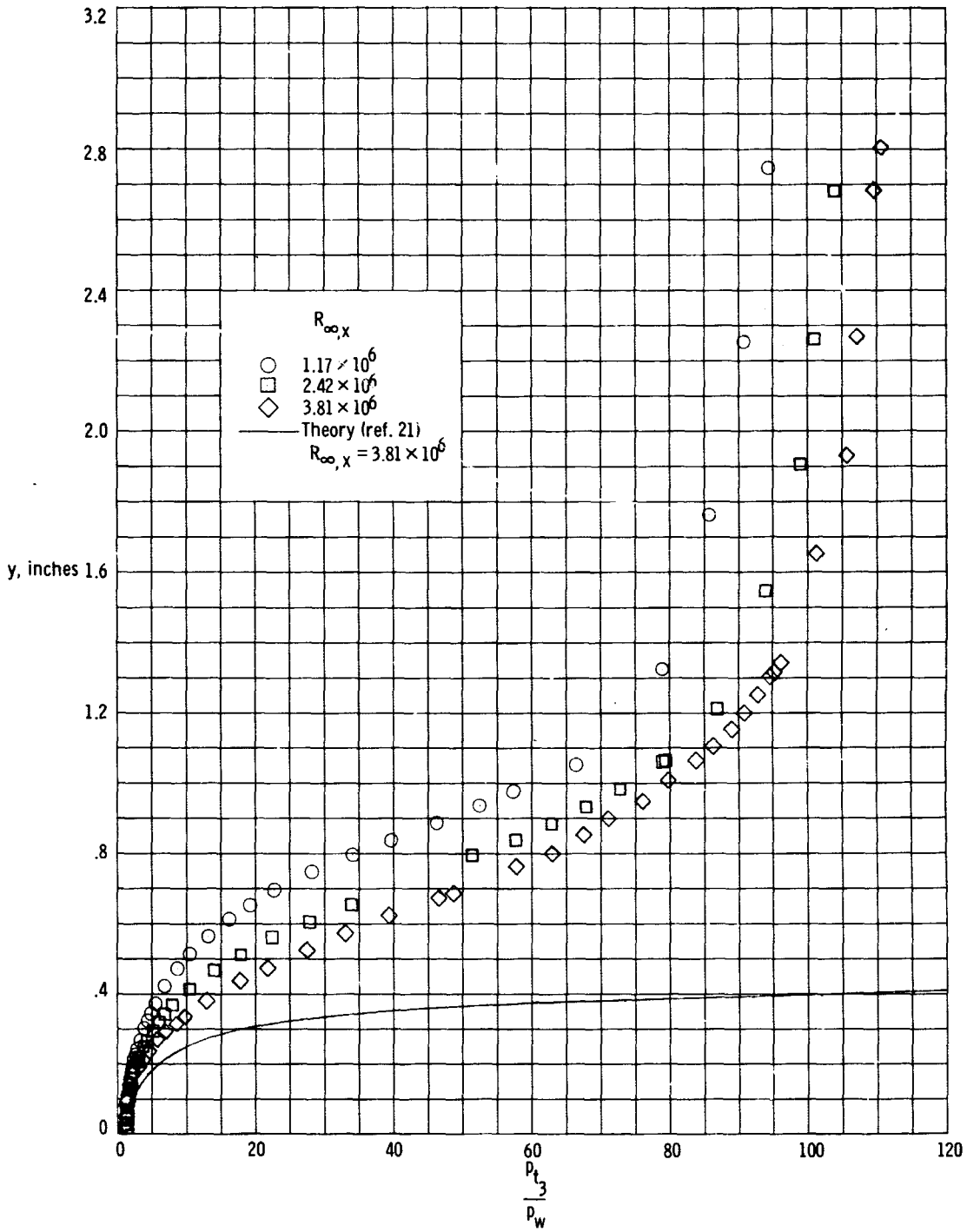

(b) x = 28.2 inches.

Figure 16.- Concluded.

Comparing the impact-pressure profiles of sharp and 0.063-inch-diameter leadings seems to support this conclusion.

The impact-pressure profile data for the 0.50-inch-diameter leading-edge model are presented in Figure 17. These data have a region of nearly constant impact pressure outside the boundary layer much the same as the sharp leading-edge data. The beginning of this region indicates the vicinity of the boundary-layer edge. One of the effects of the blunt leading edge is the reduced level of impact pressure in this region and, therefore, at the boundary-layer edge.

The Rayleigh-pitot equation was used to obtain the boundary-layer edge Mach number (M_e) from the measured impact to wall-pressure ratio. The ideal gas relationship

$$\frac{P_{t_2}}{P_{t_e}} = \left[\frac{(\gamma+1)M_e^2}{(\gamma-1)M_e^2+2}\right]^{\gamma/\gamma-1}\left[\frac{\gamma+1}{2\gamma M_e^2-(\gamma-1)}\right]^{1/\gamma-1}$$

was then used to calculate the boundary-layer edge total pressure (P_{t_e}). At all unit Reynolds numbers and probe locations, this total pressure was equal to the free-stream impact pressure. Therefore, all the boundary-layer streamlines must have passed through the normal shock portion of the bow wave.

Outside the region of constant impact pressure, the impact pressure increases as the shock wave is approached indicating the influence of the curved portion of the bow wave.

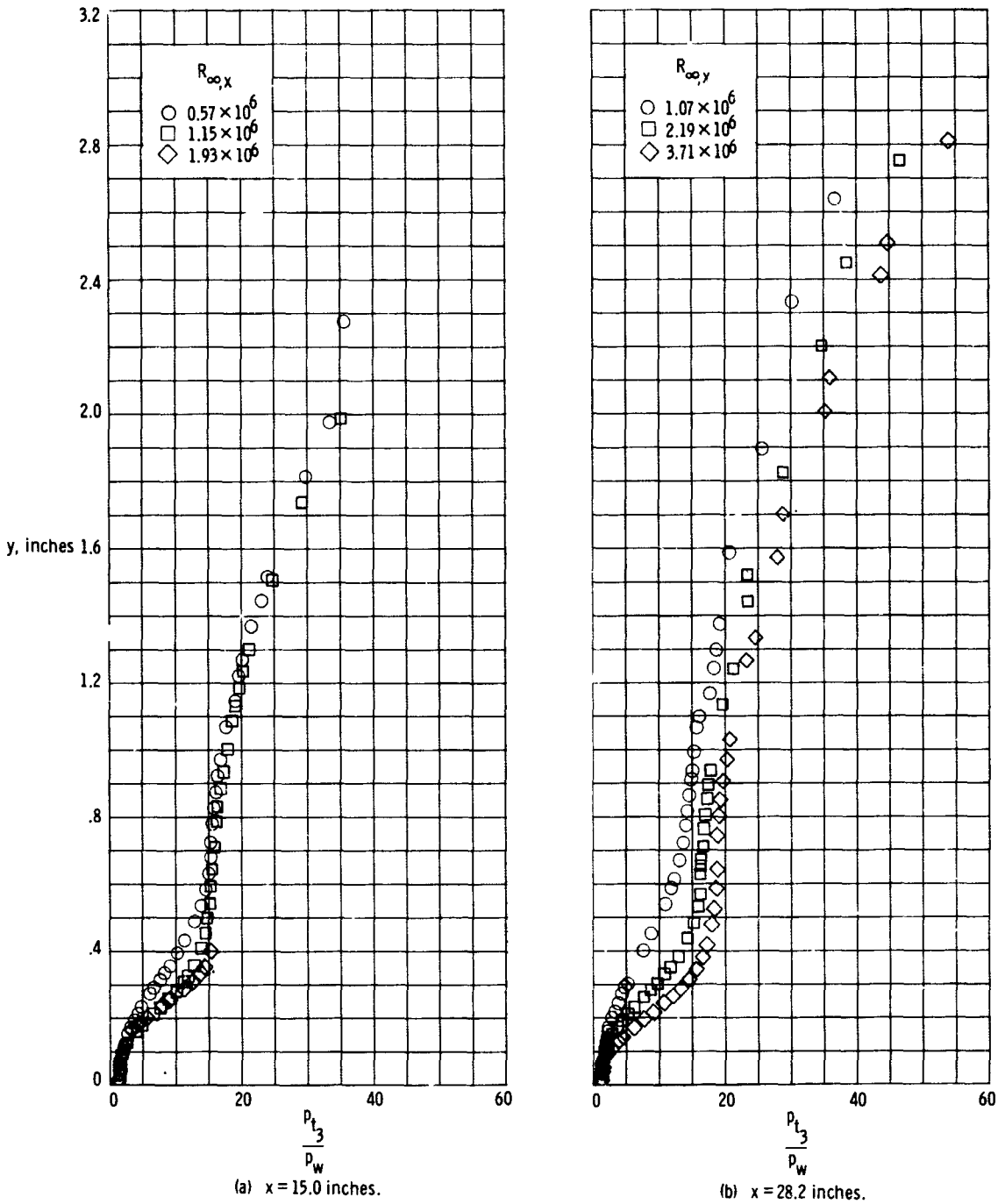

(a) x = 15.0 inches.

(b) x = 28.2 inches.

Figure 17.- Impact pressure profiles for d = 0.50-inch model.

Total Enthalpy Profile

To obtain the velocity profiles from the measured impact-pressure profiles, as mentioned in Chapter IV, it was necessary to determine a total enthalpy distribution. In Figure 18 three sample total enthalpy distributions are shown as a function of η_∞ (the Blasius similarity variable). A constant total temperature or constant total enthalpy profile is very often assumed when the wall temperature is near the adiabatic wall temperature. In the present tests, the wall temperature was much lower than the adiabatic wall temperature, and both the Klunker and McLean theory and the often-used laminar Crocco equation indicate a large difference from the constant total enthalpy distribution. The two theories agree closely. All measured velocity profiles presented in this report have been obtained using the Klunker and McLean theoretical total enthalpy distribution.

Velocity Profiles

The velocity profiles for the two probes on the sharp leading-edge model at each unit Reynolds number are presented in Figure 19. In these figures, the local to free-stream velocity ratio is plotted against the Blasius similarity variable (η_∞). The data points very near the wall are influenced by the very low Reynolds number and wall probe interference effects pointed out previously and will, therefore, be neglected entirely throughout the rest of the discussion.

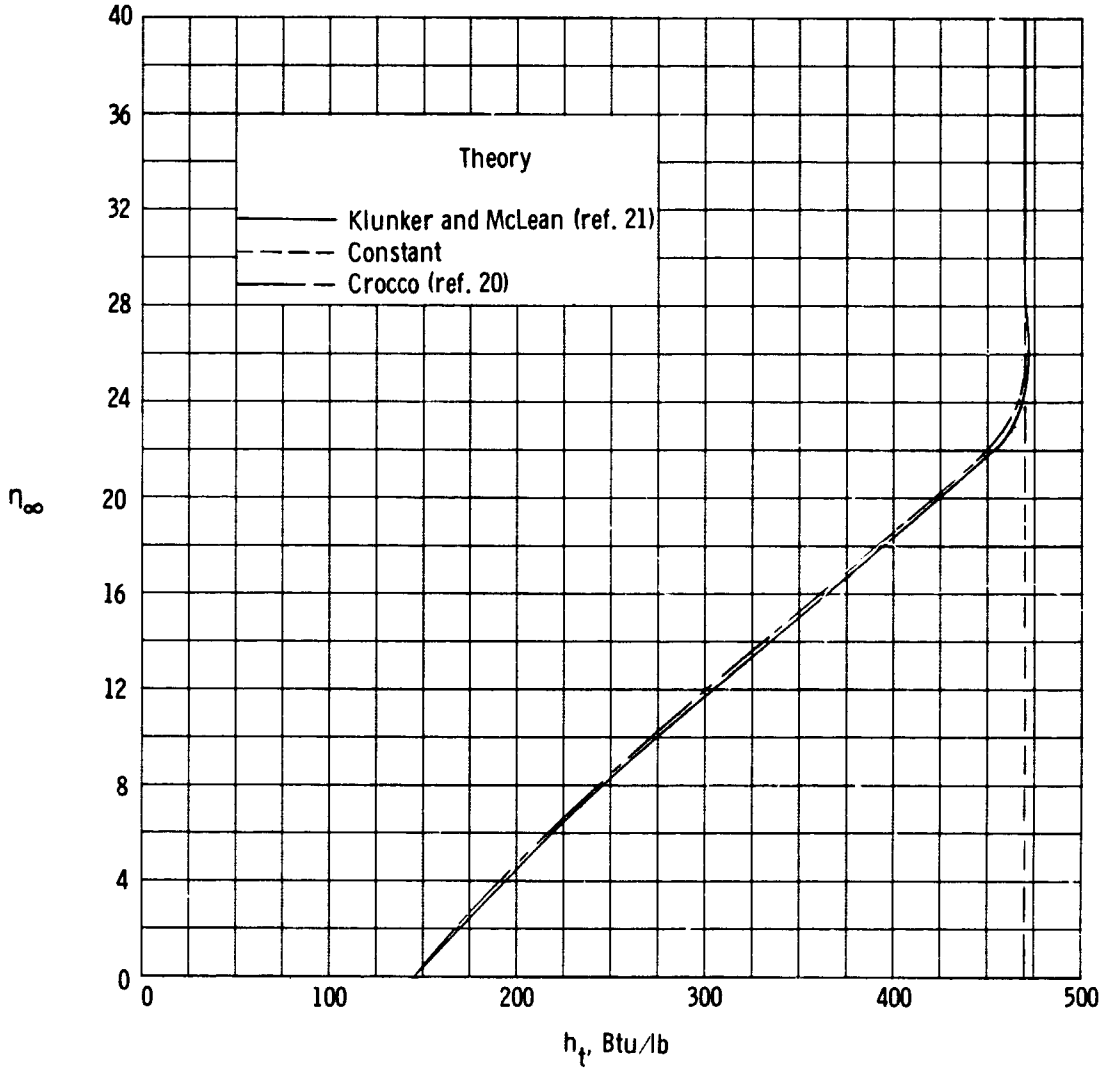

Figure 18.- Total enthalpy distributions, x = 15.0 inches, $R_{\infty,x} = 1.12 \times 10^6$.

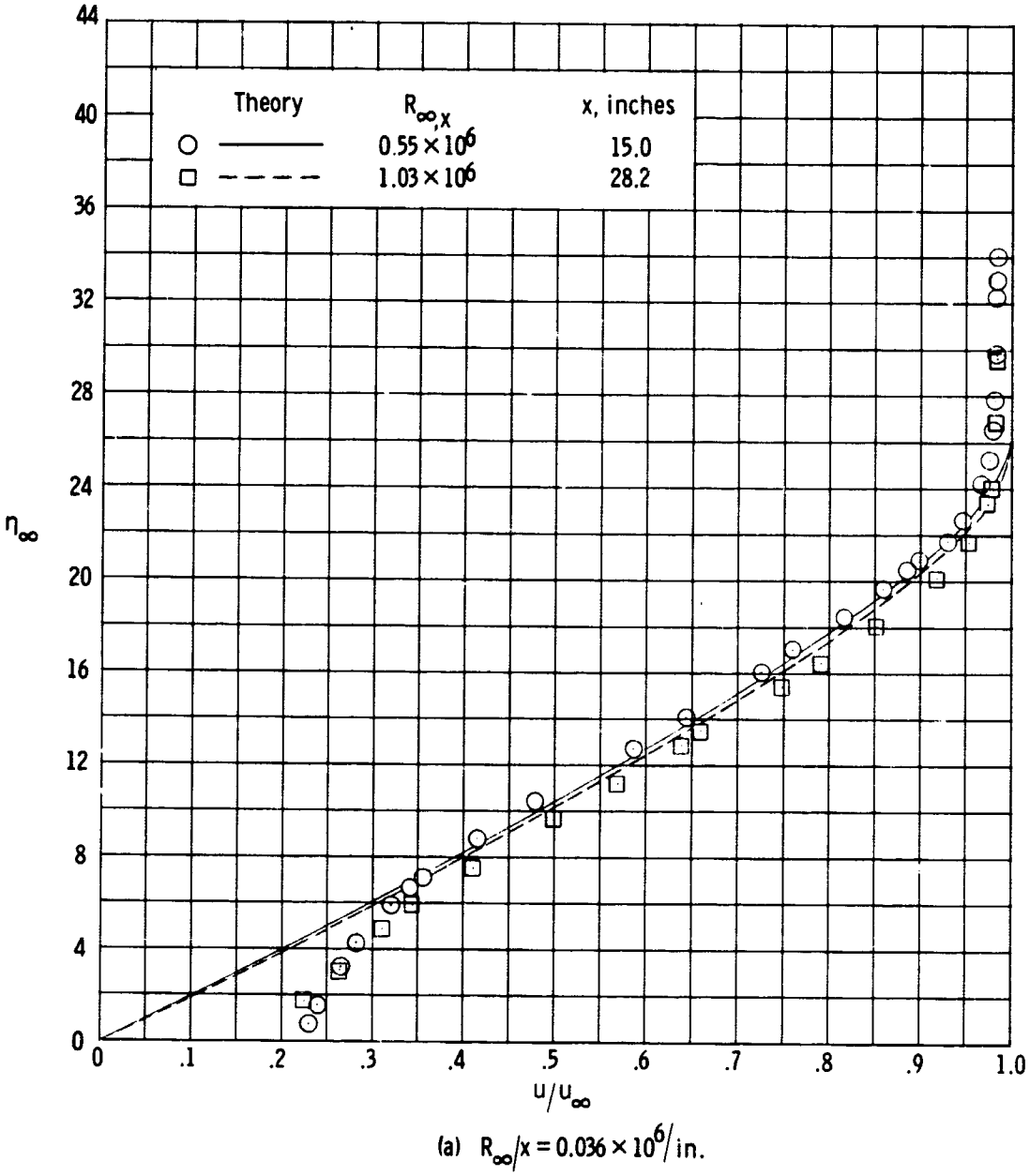

(a) $R_\infty/x = 0.036 \times 10^6/\text{in.}$

Figure 19.- Velocity profiles for sharp leading-edge model.

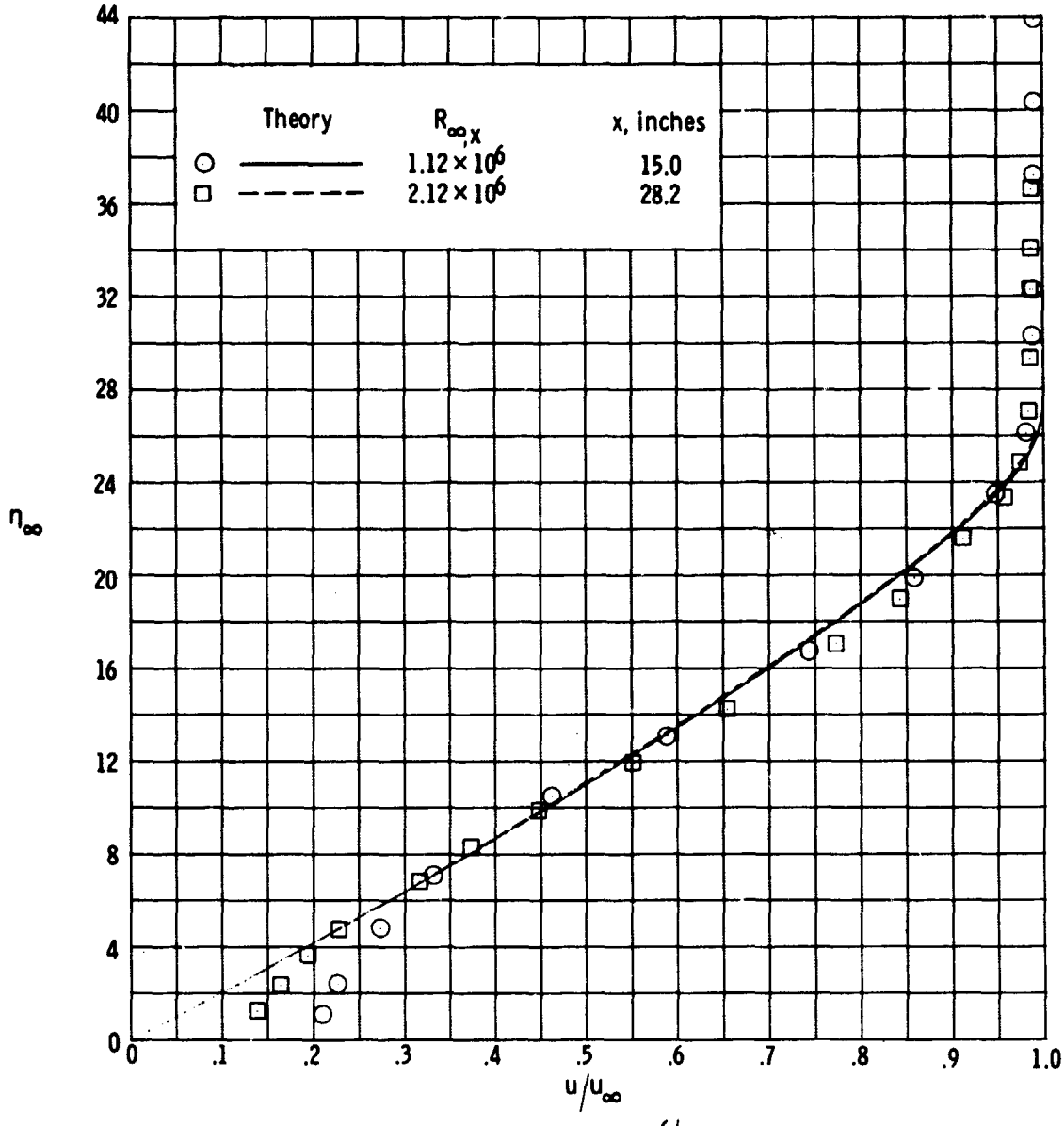

(b) $R_\infty/x = 0.075 \times 10^6/\text{in.}$

Figure 19.- Continued.

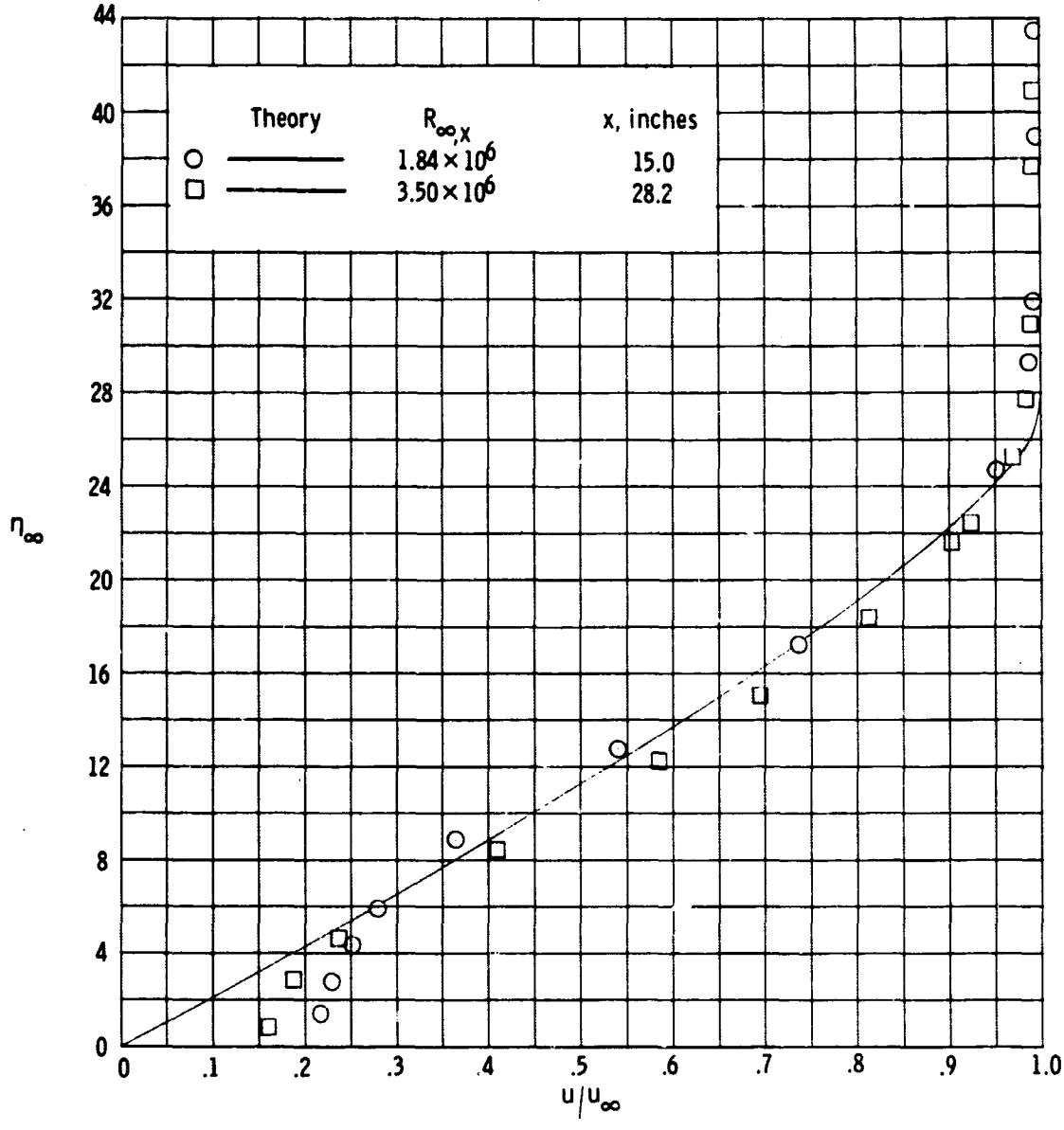

(c) $R_\infty/x = 0.123 \times 10^6$/in.

Figure 19.- Concluded.

The accuracy of the distance parameter η_∞ is within ±5 percent for the boundary-layer probe data. The accuracy of the velocity ratio due to measurement errors alone increases from 4 percent at the first "good" point to less than 1 percent at the boundary-layer outer edge.

The assumed theoretical total enthalpy distribution between the wall and the boundary-layer edge (where the total enthalpy is known) is believed to be adequate for obtaining the local velocities in the boundary layer even for the blunt leading-edge configurations. The "good" data point nearest the wall ($y \approx$ C.125 inch) has a theoretical total temperature of 975 ±50°R for all leading-edge configurations. It will be shown later that the Klunker and McLean theoretical values of heat transfer are a maximum of about twenty-six percent below the measured heat transfer for all the configurations of this study. To establish a maximum possible deviation in the total temperature at this first "good" point, a change of 100°R or about 11 percent of the total temperature was found to be sufficient to obtain a change in slope at the wall of the nearly linear total temperature distribution of about 26 percent and, therefore, a 26 percent variation of the heat-transfer rate. At other locations in the boundary-layer, total temperature differences of more than 11 percent would not be expected since the actual total temperature and total enthalpy distributions must converge to the same end points as the theoretical distributions.

The calculation procedures and equations used to calculate the velocity from the measured pressures and the assumed total enthalpy distribution are believed to be the most exact for air. The overall accuracy for the velocity then becomes ±10 percent including possible differences in total enthalpy and measurement errors.

The sharp leading-edge data agree with the theory within the above stated accuracies (Fig. 19). The data outside the boundary layer are slightly different from a velocity ratio value of one as would be expected from the differences in the impact-pressure ratio.

The velocity profiles for the 0.063-inch-diameter leading-edge model are presented in Figure 20 along with the Klunker and McLean sharp leading-edge theory as a reference profile. The data show two regions of different velocity gradients. For $\eta_\infty < 20$, there is a region of relatively large velocity gradient which is less than the sharp leading-edge gradient. For values of η_∞ greater than about 30, the velocity increases slightly with increasing η_∞. In Figure 20(a), for the $R_{\infty,x} = 0.59 \times 10^6$ data, $\eta_\infty = 32$ corresponds to $y = 0.604$ inches. In Figure 16(a) the impact-pressure profile for this survey shows that at $y = 0.604$ inch, the region of the largest impact-pressure gradient is just starting. Thus, the outer region of small velocity gradient is a region of large impact-pressure gradient. In the usual sense, the boundary layer is considered to be the region adjacent to the wall where there is a large velocity gradient and, therefore, a region of viscous shearing. On this

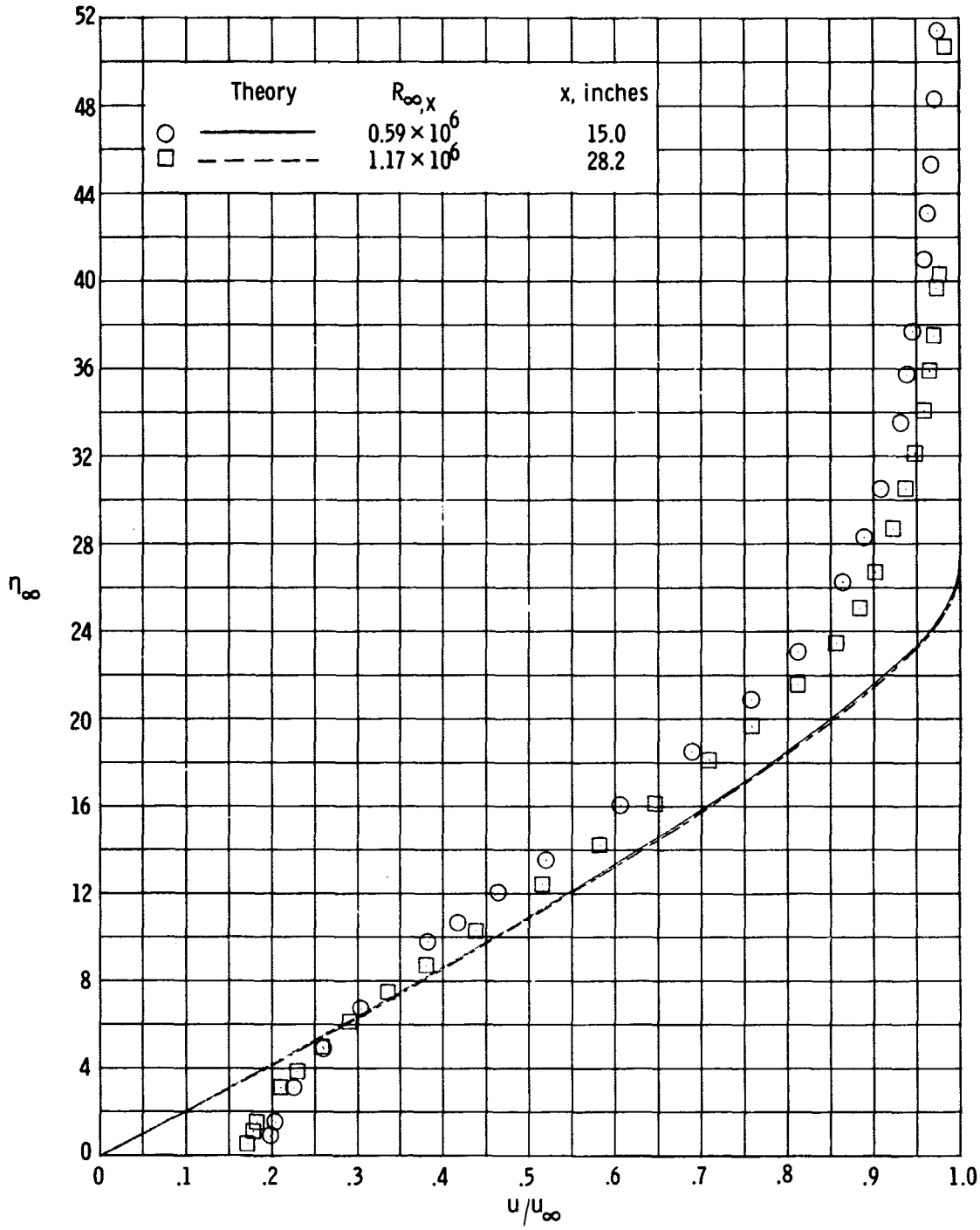

(a) $R_\infty/x = 0.041 \times 10^6/\text{in.}$

Figure 20.- Velocity profiles for the 0.063-inch-diameter leading-edge model.

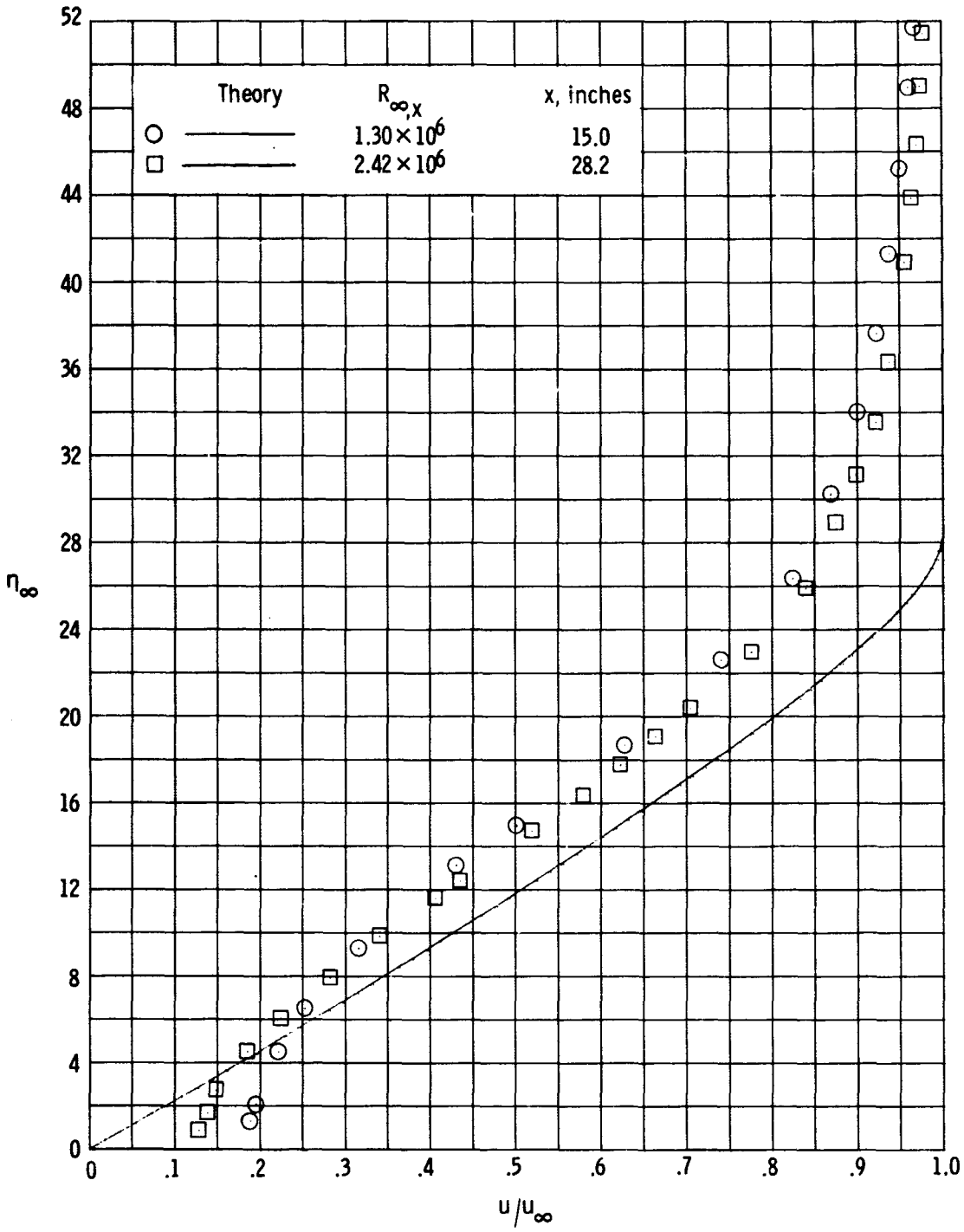

(b) $R_\infty/x = 0.086 \times 10^6/\text{in.}$

Figure 20.- Continued.

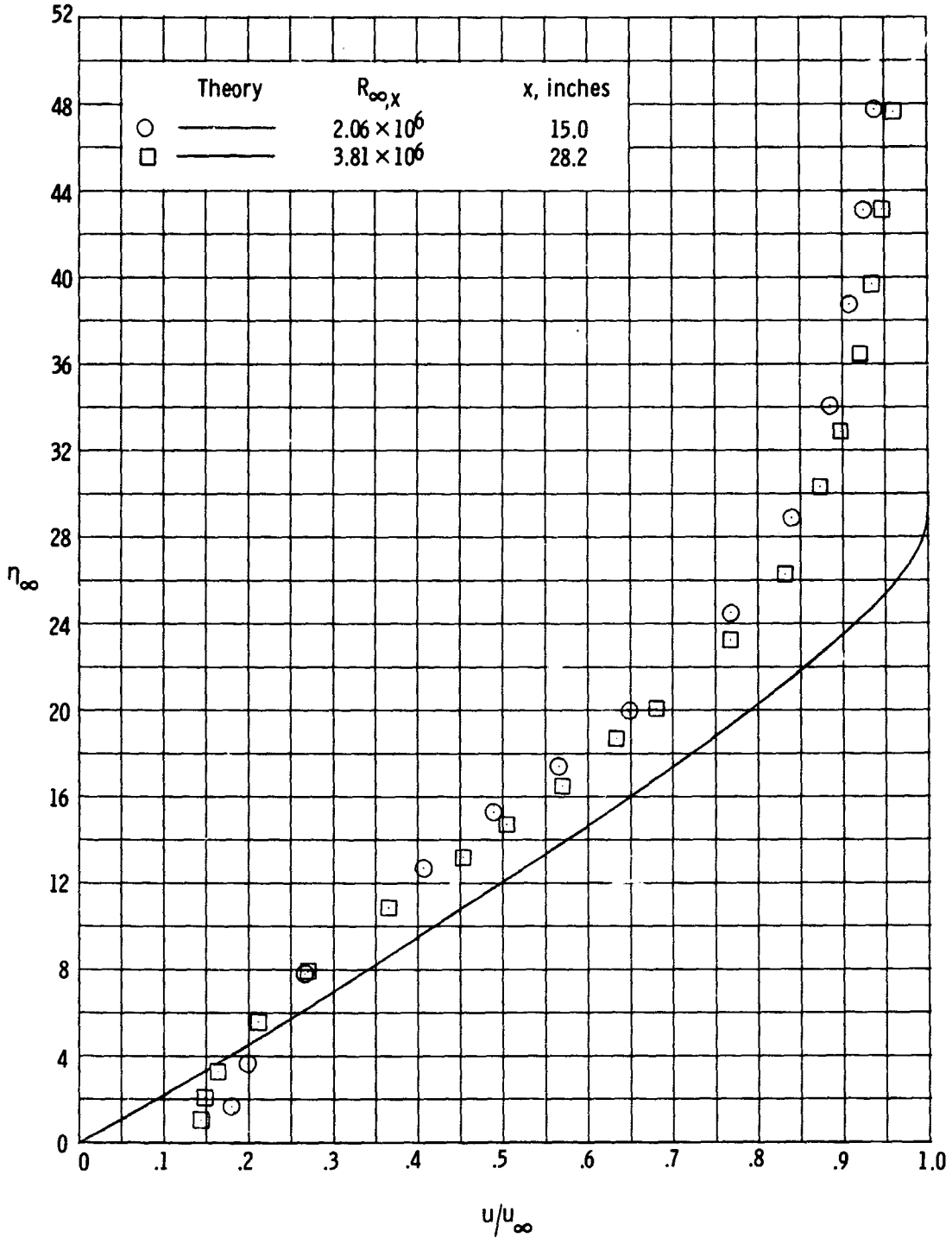

(c) $R_\infty/x = 0.136 \times 10^6/\text{in.}$

Figure 20.- Concluded.

basis then the boundary-layer edge would be in the vicinity of $\eta_\infty = 32$ for this configuration. Therefore, much of the impact-pressure variation occurring in the flow field adjacent to this model occurs outside the boundary layer. The streamlines just outside the boundary layer must have passed through the curve portion of the leading-edge shock wave and an entropy gradient exists in this region.

The velocity profiles for the 0.50-inch-diameter leading-edge model are presented in Figure 21. The measured profiles are surprisingly close to the theory except that the large blunt leading edge has caused a considerably lower boundary-layer edge velocity. The boundary-layer edge for the $R_{\infty,x} = 0.57 \times 10^6$ profile occurs at $\eta_\infty = 30$. This corresponds to $y = 0.58$ inches in Figure 17(a) at the start of the region of constant impact pressure.

The typical bluntness effect on the velocity profile is shown in Figure 22 where the profiles for the three leading-edge configurations for a given free-stream Reynolds number are plotted. The very blunt leading edge generally appears to have the steepest velocity profile near the wall while the boundary-layer thickness is nearly the same as for the sharp leading-edge configuration. The slight blunting decreases the velocity gradient and thickens the boundary layer.

Static Temperature Profiles

Sample static temperature profiles behind the three leading

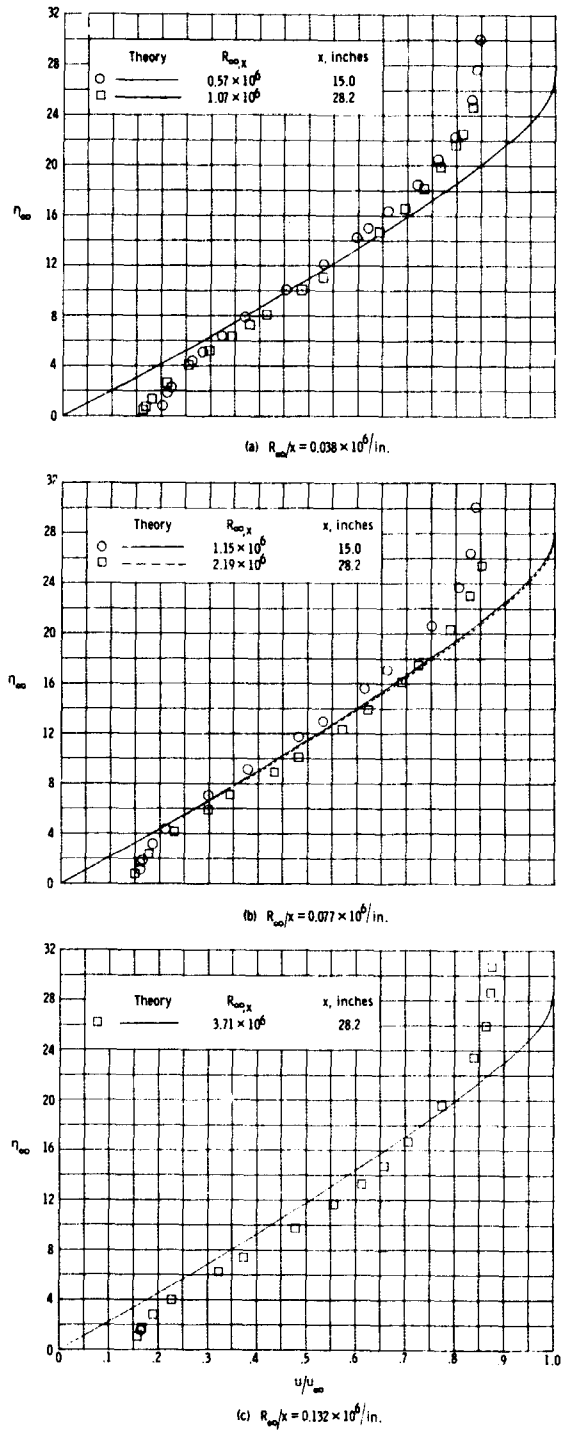

Figure 21.- Velocity profiles for the 0.500-inch-diameter leading-edge model.

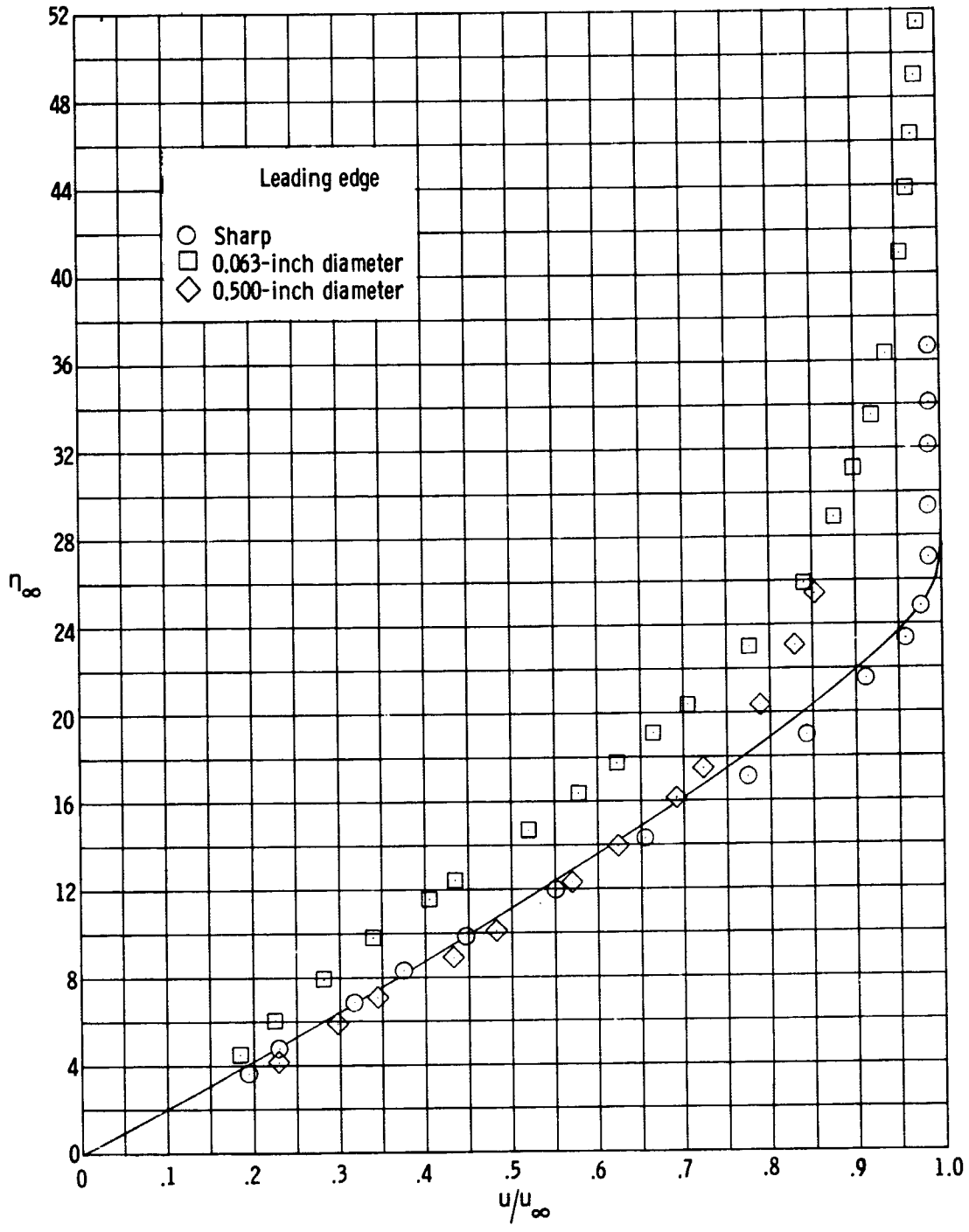

Figure 22.- Bluntness effect on velocity profile; x = 28.2 inches, $R_{\infty,x} \approx 2.25 \times 10^6$.

edges are shown in Figure 23. As previously mentioned, the data points near the wall are in the region of very low probe Reynolds number and have, therefore, been deleted from the plot. The sharp leading-edge data compare fairly well with the Klunker and McLean theory based on free-stream conditions except near the boundary-layer edge. The profile for the 0.063-inch-diameter leading-edge model shows a somewhat higher maximum static temperature with the peak located further from the surface than for the profile for the sharp leading-edge model. The profile for the 0.50-inch-diameter leading-edge model has a maximum static temperature only slightly lower than the sharp leading-edge model. It must be remembered, however, that these static temperature profiles are obtained from the experimental Mach number distribution and the Klunker and McLean theoretical total temperature distribution with an overall accuracy of 13 percent.

Velocity Profile Similarity

The velocity profiles for the sharp leading-edge model are similar in η_∞ by virtue of the agreement with the similarity solution of the Klunker and McLean theory. The Blasius similarity variable η_∞ allows for boundary-layer growth. It can be thought of as $\eta_\infty = y/g(x)$ where $g(x) = x/\sqrt{R_{\infty_x}}$. To have similarity, the following equality must hold

$$\frac{u\left|x_1, \frac{y}{g(x_1)}\right|}{u_e(x_1)} = \frac{u\left|x_2, \frac{y}{g(x_2)}\right|}{u_e(x_2)} \quad .$$

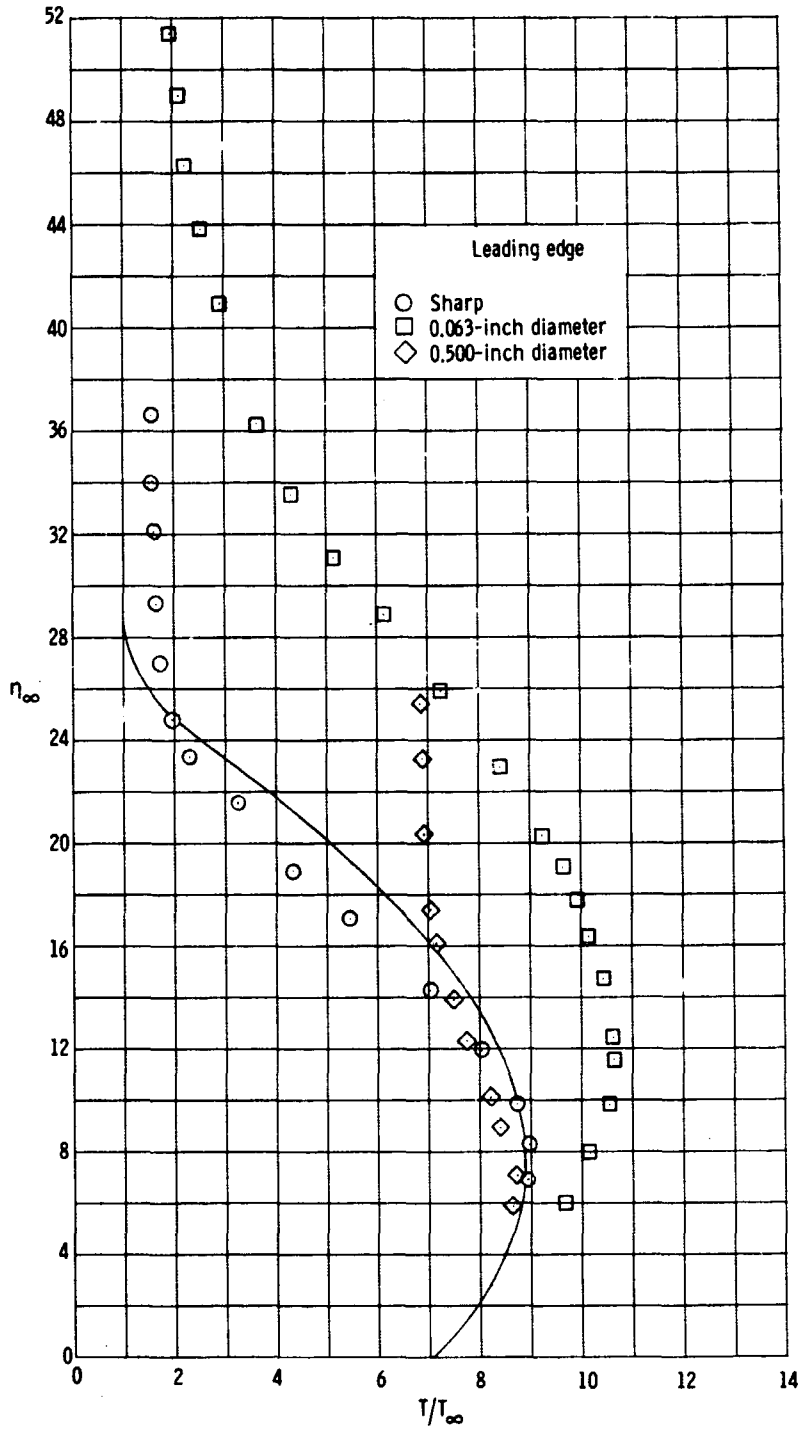

Figure 23.- Static temperature profiles; x = 28.2 inches, $R_{\infty,x} \approx 2.25 \times 10^6$.

When the induced pressure gradient is sufficient to affect the boundary-layer growth, the velocity profile would not be expected to be similar in η_x. However, the velocity profiles may still exhibit similarity. If any profile similarity exists, it must show up in the form of u/u_e versus y/δ.

An often-used definition of the boundary-layer thickness is δ = y where the velocity is 99.9 percent of the velocity outside the boundary layer. However, the 0.063-inch-diameter leading-edge model had a slightly varying velocity outside the boundary (see Fig. 21), and it would be impossible to determine 0.999 u_e. Therefore, a boundary-layer quantity δ' was defined as the point where a straight line fairing through the linear portion of the velocity profile crosses a straight line fairing through the velocity data points outside the boundary layer. This point was also used to define an effective boundary-layer edge (u_e) velocity.

In Figure 24 the velocity ratio, u/u_e, is plotted versus y/δ' for three different Reynolds numbers on the sharp leading-edge model. The data show, as expected, that the velocity profiles are similar in y/δ'. However, the velocity ratio is not unity at $y/\delta' = 1$. This is because δ' is not the usual boundary-layer thickness.

In Figure 25, the 0.063-inch-diameter leading-edge profiles are seen to exhibit similarity within the accuracy of obtaining δ'. Since similarity is exhibited for different unit Reynolds numbers

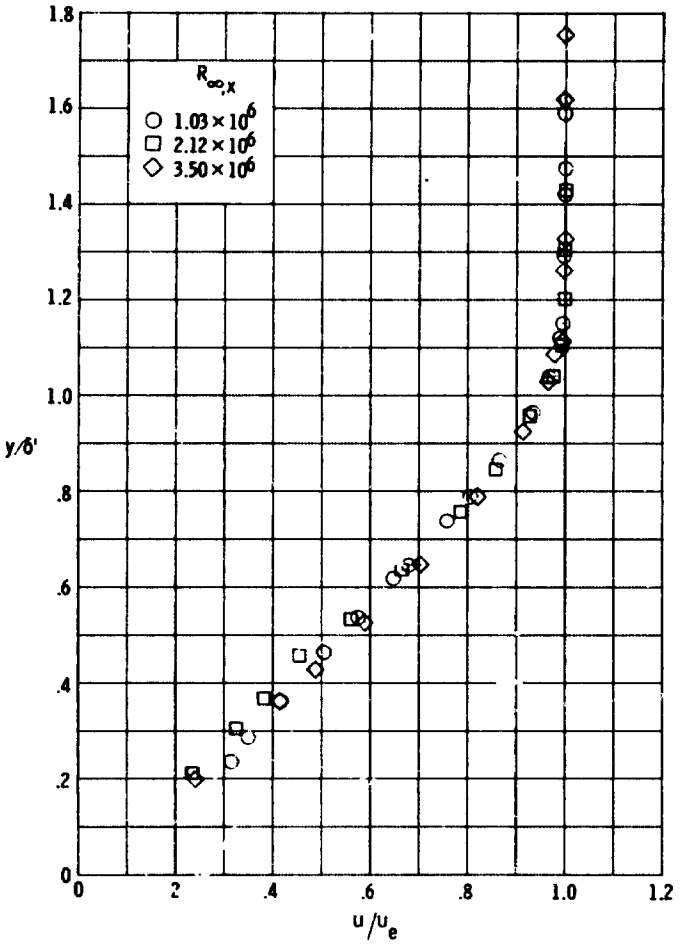

Figure 24.- Similarity of sharp leading-edge model velocity profiles; x = 28.2 inches.

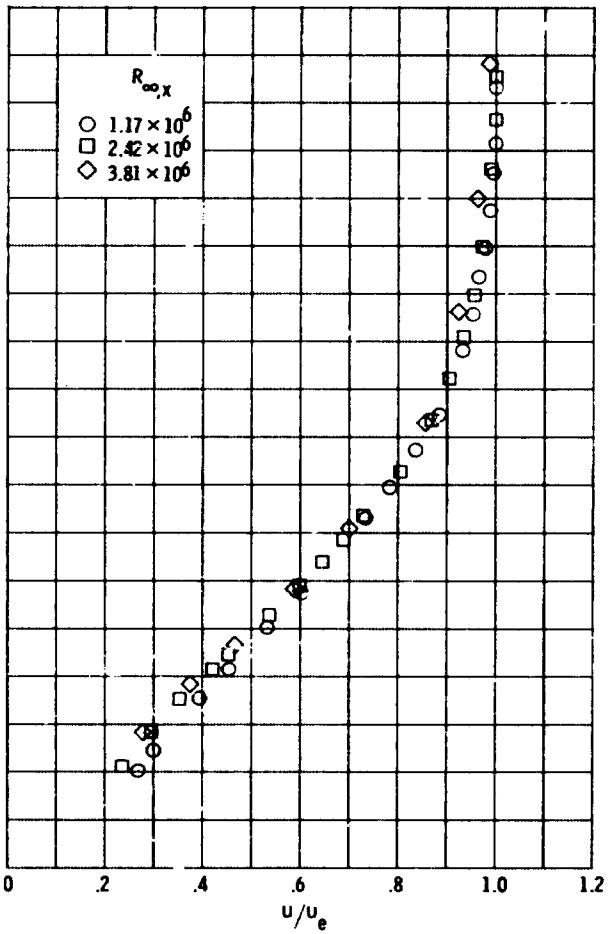

Figure 25.- Similarity of the 0.063-inch-diameter leading-edge model velocity profiles; x = 28.2 inches.

and different probe locations, then δ' or $g(x)$ must be a function of $R_{\infty,d}$ and x/d. The same conclusion is reached for the 0.50-inch-diameter leading-edge model. The similarity profiles are presented in Figure 26 for this configuration.

For the same probe location and free-stream unit Reynolds number, the effect of bluntness on the similarity of the velocity profiles can be seen in Figure 27. It appears that for y/δ' less than approximately 0.6, the velocity profiles do exhibit similarity. Thus, even though there is a large entropy increase for the bluntest leading edge and a pressure gradient, the inner portion of the boundary layer conforms to the zero-pressure gradient shape. This suggests a universal relationship for $g(x)$ involving $R_{\infty,d}$ and x/d.

Boundary-Layer Thickness

Creager (Ref. 29) found good agreement between his $M_\infty = 4.0$ boundary-layer thickness data and a theoretical equation from Lees and Probstein (Ref. 1) that was altered to account for the finite leading-edge thickness. Creager's equation was

$$\frac{\delta}{d}\sqrt{R_{\infty,d}} = \left[\frac{1.73}{M_\infty^2}\left|\frac{T_w}{T_\infty}\right| + 0.332(\gamma-1) + \frac{4.27}{M_\infty^2}\right] M_\infty^2 \sqrt{C_w}\sqrt{\frac{x}{d}} \quad (22)$$

To compare the present test results with this equation required locating the boundary-layer edge, as defined by Lees and Probstein, to be the location of $u/u_e = 0.999$. In Figures 24 and 26, the

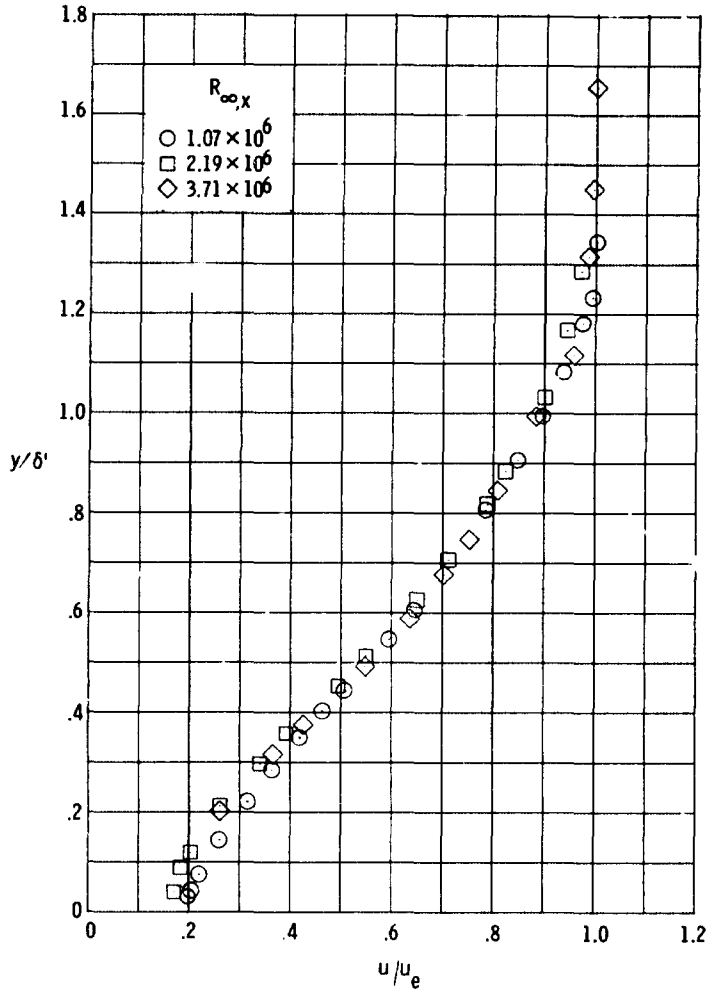

Figure 26.- Similarity of the 0.500-inch-diameter leading-edge model velocity profiles; x = 28.2 inches.

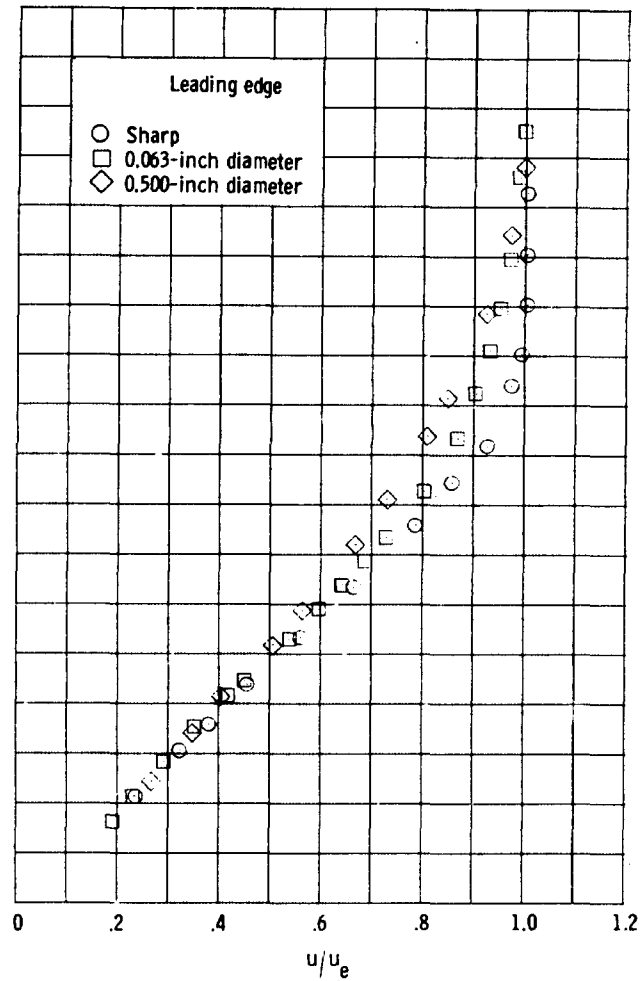

Figure 27.- Similarity of velocity profiles behind different leading edges; $R_{\infty,x} \approx 2.25 \times 10^6$, x = 28.2 inches.

similarity profiles become tangent to the $u/u_e = 1.0$ line and thus the y value for $u/u_e = 0.999$ was easily obtained. In Figure 25 the profiles showed the slight velocity gradient outside the boundary layer. In an attempt to select a boundary-layer edge value that could be compared with the other data of the present tests, a straight-line fairing of the velocity data outside the boundary layer was assumed to be analogous to the $u/u_e = 1.0$ line. The tangent point of the data with this fairing was picked as the boundary-layer edge. These data are compared with a plot of Equation (22) in Figure 28. The agreement of the boundary-layer thickness data for the present tests with Creager's equation (Eqn. 22) is surprisingly good considering the difficulty in determining the boundary-layer thickness. Creager's (Ref. 29) data showed that the boundary-layer thickness is proportional to the square root of x for $0.6 \leq x \leq 15.5$ at Mach 4 behind cylindrical leading edges. The present data show that $\delta \propto \sqrt{x}$ for $30 \leq x/d \leq 14{,}000$ at Mach 10.4 for cylindrical leading edges.

Skin Friction

The nearly linear portions of the velocity profiles were faired to the origin, and the slopes of the fairings at the wall were used to obtain the skin friction (Eqn. 18). A sample plot and fairing is shown in Figure 29. As can be seen in the figure, the previously discussed data points near the plate have not been considered in the fairings. Also in the previous discussion about

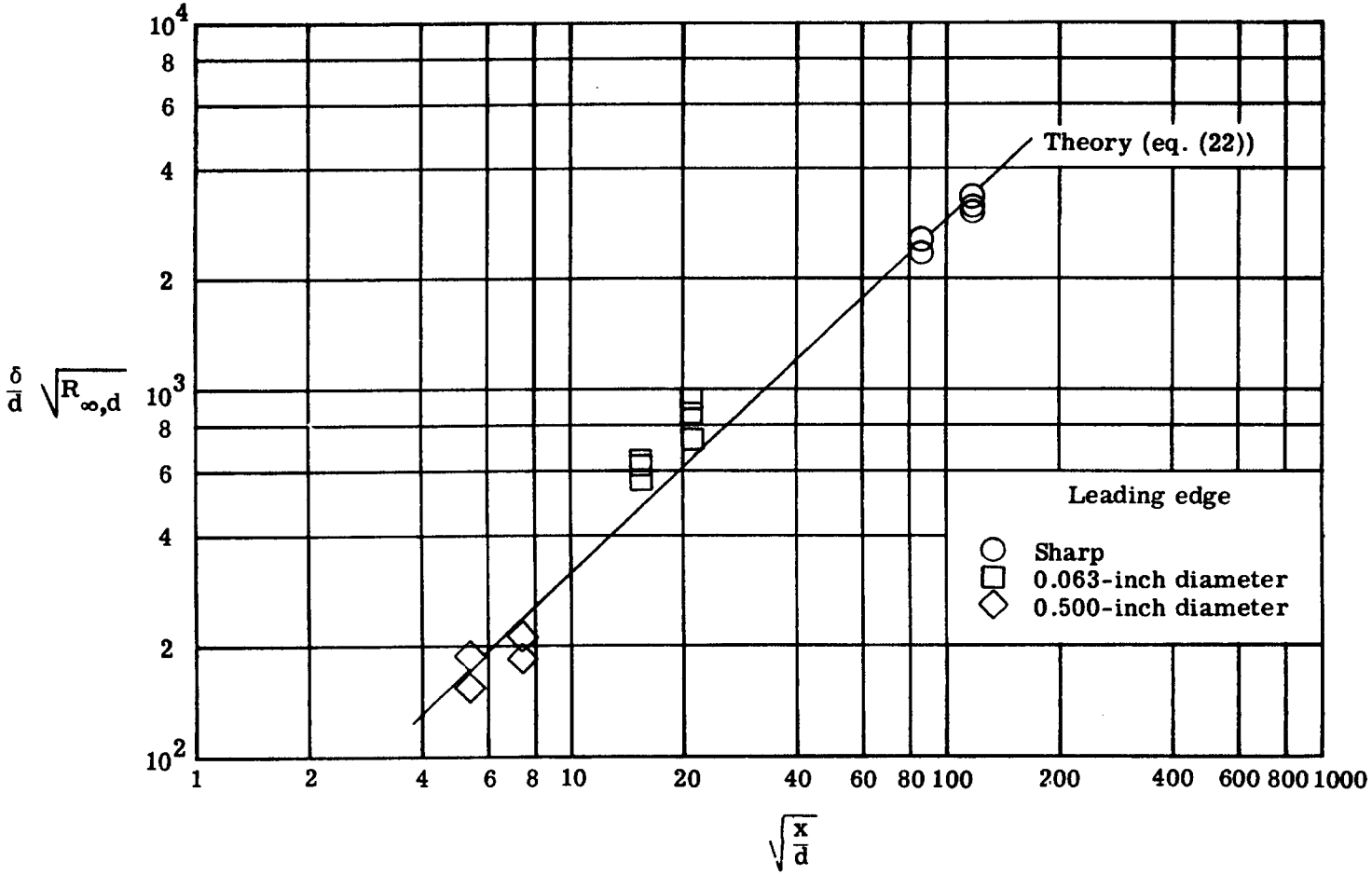

Figure 28.- Boundary-layer thickness behind different leading edges.

the velocity profiles, it was noted that at the first "good" point the accuracy was ± 10 percent in the velocity and 0.004 inch in the y dimension. If the velocity profile is linear from the first "good" point to the wall, then these maximum errors will result in an accuracy of 14 percent in the slope at the wall.

The graphical method used to obtain the slope decreases the accuracy level. The slope of some of the profiles was obtained several times with a maximum variation of 5 percent. It is believed that the maximum overall accuracy of $(\partial u/\partial y)_w$ is ± 19 percent.

The local skin-friction coefficient (C_f) based on the free-stream dynamic pressure is plotted in Figure 30 as a function of free-stream Reynolds number. The accuracy in the skin-friction coefficient is about 20 percent since the accuracy in $\rho_\infty u_\infty^2$ is 4 percent. The sharp leading-edge model data compare favorably with the Klunker and McLean theory as would be expected. The data for the 0.063-inch-diameter leading-edge model fall below the sharp leading-edge model data. The impact pressure and velocity profiles (see Figs. 16 and 22) revealed that the leading-edge bluntness altered the flow field, thickened the boundary layer, and decreased the slope of the velocity profiles. The skin-friction values reflect this effect. A further blunting of the leading edge increased the skin friction as suggested by the velocity profiles (Fig. 22).

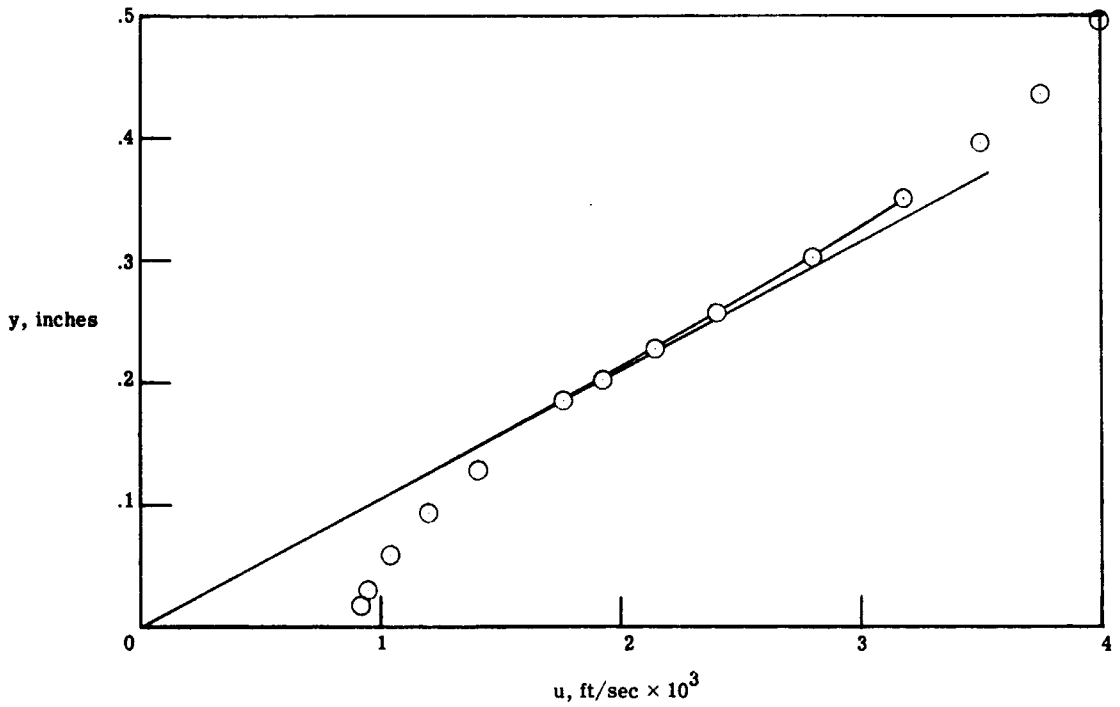

Figure 29.- Velocity profile and slope for 0.063-inch-diameter leading-edge model and $R_{\infty,x} \approx 0.59 \times 10^6$, x = 15.0 inches.

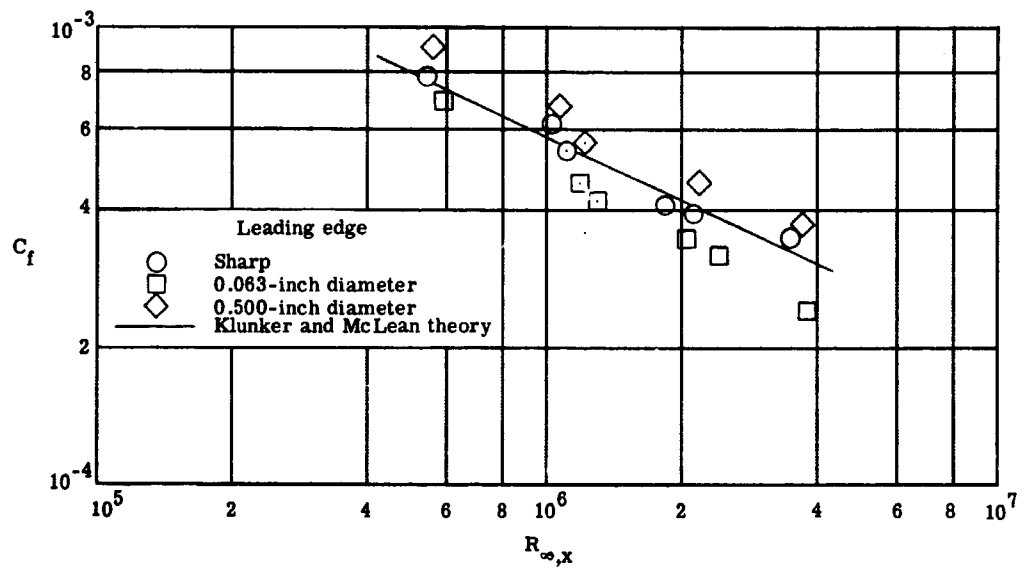

Figure 30.- Local skin friction.

Heat Transfer

All of the heat transfer data were reduced to the form of Stanton number (N_{ST_∞}). The accuracy for this quantity is ±9 percent which includes the accuracies for the material properties stated in Chapter II, the repeatability of the measured temperatures, and the accuracy of the free-stream Mach numbers, stagnation pressures, and stagnation temperatures. The accuracy value stated above does not include heat-conduction effects.

A finite difference approximation was applied to the measured wall temperatures to determine the heat conduction in the plate at the time the heat transfer values were obtained. The maximum heat conduction obtained was less than 0.50 percent of the absorbed energy. This conduction took place in the stream direction. At the stations where thermocouples were in a row perpendicular to the stream direction, the calculated heat conduction laterally was approximately one-third of the above value. Thus, no conduction correction was applied to the measured data. In addition, the contribution of radiant heat transfer to the model was evaluated. In the tunnel, the model (instrumented plate) was parallel to the tunnel floor and perpendicular to the tunnel side wall that supports the quartz schlieren windows. At certain wave lengths quartz has a high emissivity. The spectral emissivity of quartz, in general, is available; however, the spectral emissivity for the particular quartz used in the windows is not known. The temperature history of the

windows during the present tests was not measured; nevertheless, previous measurements show that the outside window temperature under similar conditions has not exceeded 300° F. A conservative estimate of heat transfer from the tunnel wall boundary layer and an approximate value of shape factor were used to calculate a radiant heating to the model. The resulting radiant heating was about 7 percent of the lowest model heating and 1 percent for the highest model heating rate.

The heat transfer data for the sharp leading-edge model are presented in Figure 31. The data are presented in the form of N_{ST_∞} versus $R_{\infty,x}$ and some of the data are shown "corrected" for the pressure effect $\left(N_{ST_\infty}/K_3\sqrt{P_w/P_\infty}\right)$ (darkened symbols). This "correction" method due to Bertram and Feller (8) was discussed at the end of Chapter III. Also presented in Figure 31 is the Klunker and McLean theoretical prediction for the present test conditions ($K_3 = P_w/P = 1$ for the theory) and a fairing of the "uncorrected" data parallel to the theory. The "uncorrected" data correlate nicely and seem to have the same slope as the fairing and the Klunker and McLean theory. The difference between the fairing and the theory is about 19 percent, which is more than the sum of accuracy plus the possible radiant heat transfer to the model. Thus, it appears that the induced pressures have caused an increased heat transfer.

The corrected heat transfer data have a slightly smaller slope than the theory and, in fact, cross the theoretical prediction.

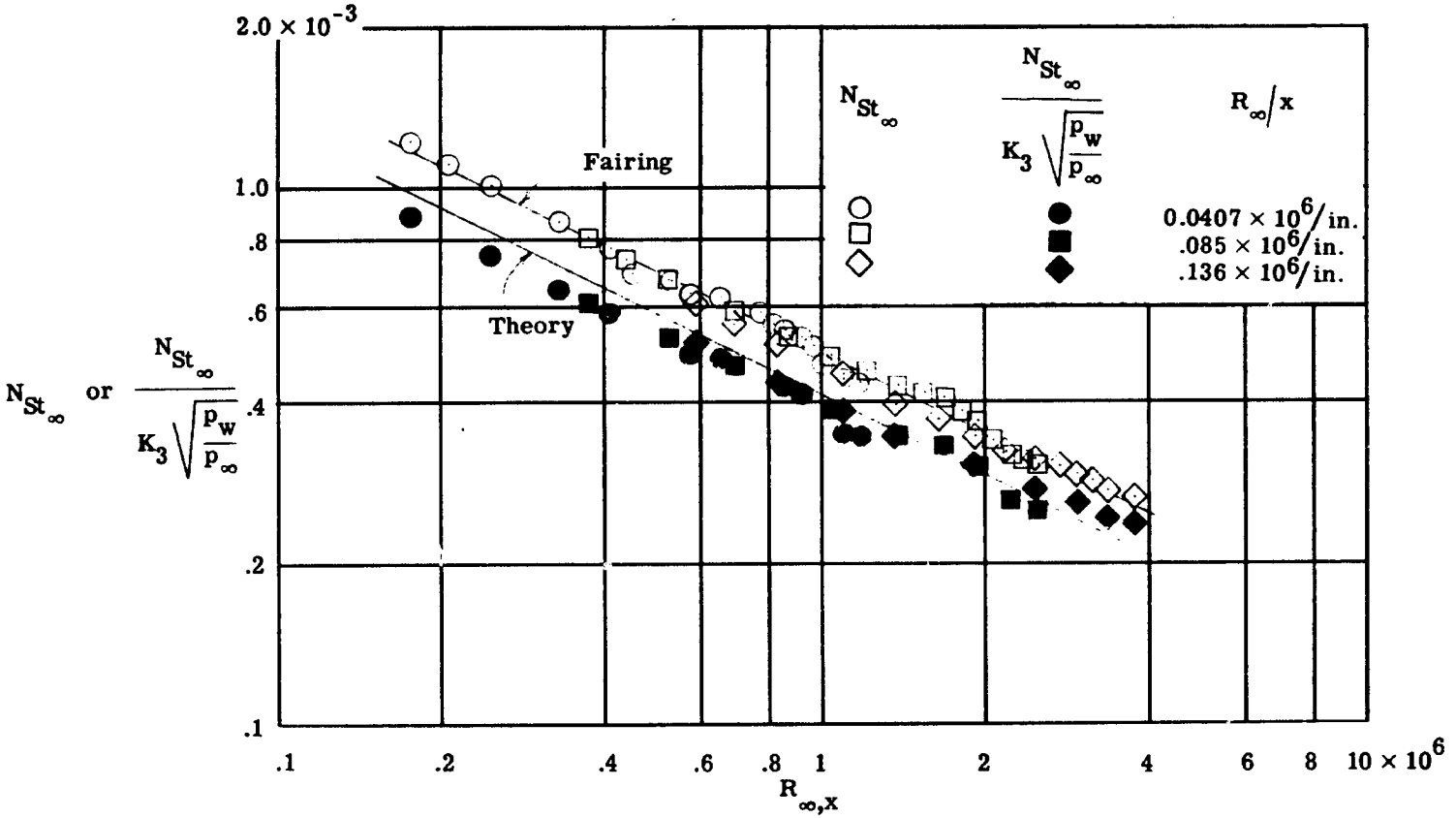

Figure 31.- Heat transfer to sharp leading-edge model.

The change in slope is due to the change in pressure with x. The corrected data are nevertheless in good agreement with the theory.

The bluntness effect at each free-stream unit Reynolds number on the heat transfer data (uncorrected) is shown on Figure 32. At each free-stream unit Reynolds number the 0.063-inch-diameter leading-edge model data are lower than the sharp leading edge data similar to the skin friction data.

In the discussion of the temperature profiles, it was pointed out that the peak in the boundary-layer temperature distribution for the 0.063-inch-diameter leading-edge model was higher and further from the model surface than for the sharp model (see Fig. 23). Although the peak is higher, the heat transfer data indicates that the slope at the wall must be less.

The heat transfer data for the 0.50-inch-diameter leading-edge model is generally above the data for the sharp model. Thus, progressively blunting the leading edge first decreases the heat transfer and then causes an increase in heat transfer. Neal (Ref. 13) found a similar bluntness effect at $M_\infty = 6.8$. The 0.50-inch-diameter leading-edge model data is about 26 percent above the Klunker and McLean theory as was postulated in the discussion regarding the assumed total enthalpy distribution.

Reynolds Analogy Factor

The Reynolds analogy is very often used to obtain skin-friction information from heat-transfer data. For the present test conditions,

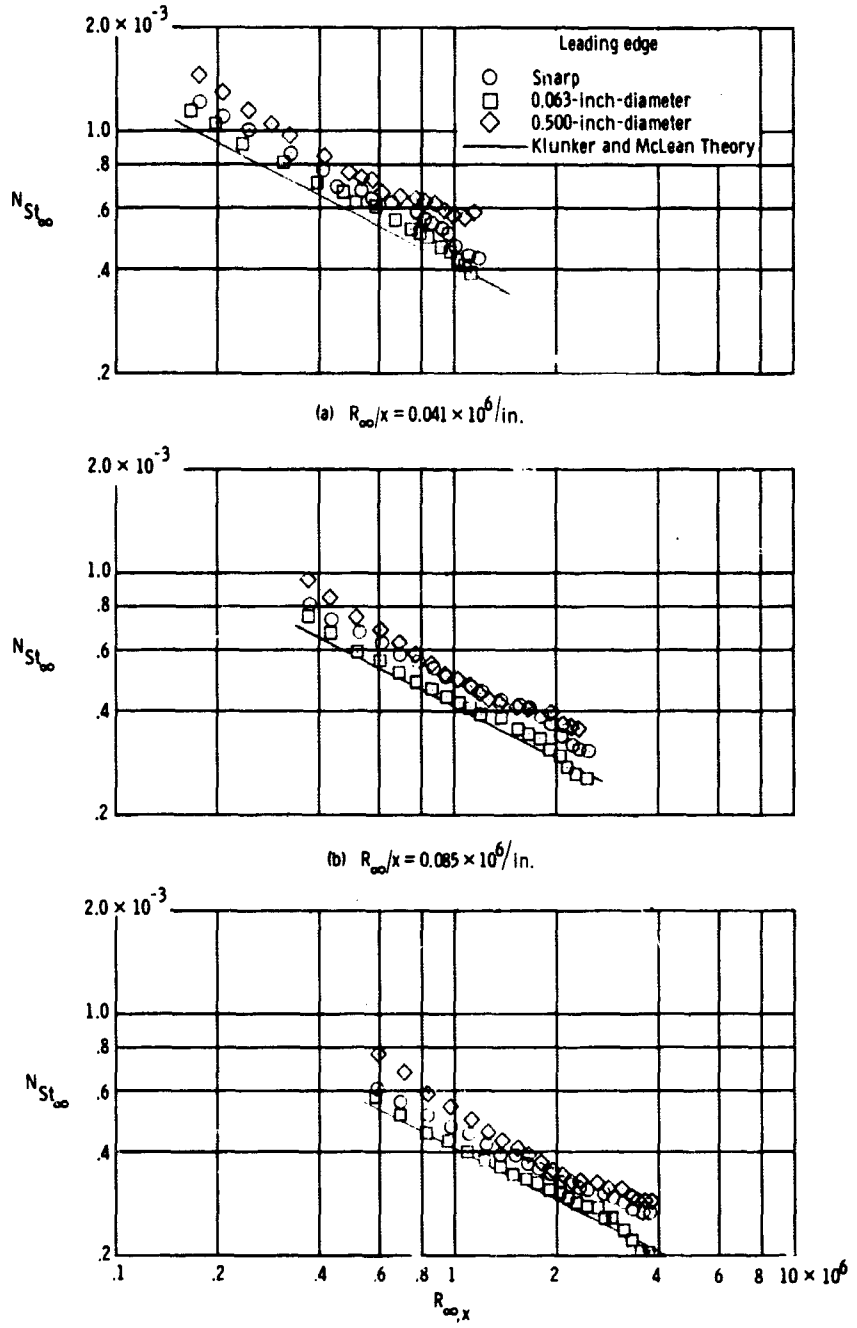

Figure 32.- Bluntness effect on heat transfer

the Klunker and McLean theory predicts that the ratio of Stanton number to one-half the skin-friction coefficient (Reynolds analogy factor) has a value of approximately 1.34. The well-known Colburn modification to Reynolds analogy, $2N_{ST}/C_f = N_{Pr}^{-2/3}$ gives a value of 1.25. In Figure 33, the experimentally determined Reynolds analogy factor (based on local conditions) is plotted as a function of the free-stream Reynolds number. The heat transfer and skin-friction data based on free-stream conditions were modified to local conditions by the following equation:

$$\frac{N_{ST_l}}{C_{f_l/2}} = \frac{M_l}{M_\infty}\sqrt{\frac{T_l}{T_\infty}}\left[\frac{T_{aw_\infty} - T_w}{T_{aw_l} - T_w}\right]\frac{N_{ST_\infty}}{C_{f/2}}$$

where M_l, T_l, and T_{aw_l} are computed for conditions at the boundary-layer edge (δ) using the probe data and the methods previously discussed. Since there is no correction method available for the pressure effect on the thermal conductivity, the skin friction coefficient used to determine Reynolds analogy factor was computed without the pressure effect on viscosity (Eqn. 15). These data have an overall accuracy of ± 22 percent.

The average values of the Reynolds analogy factor for the sharp and the 0.063-inch-diameter leading-edge data are about 1.51 and 1.53 respectively. Increasing the leading-edge bluntness to 0.50 inch reduces the average value to about 1.22. There appears to be no consistent Reynolds number effect for these data. The

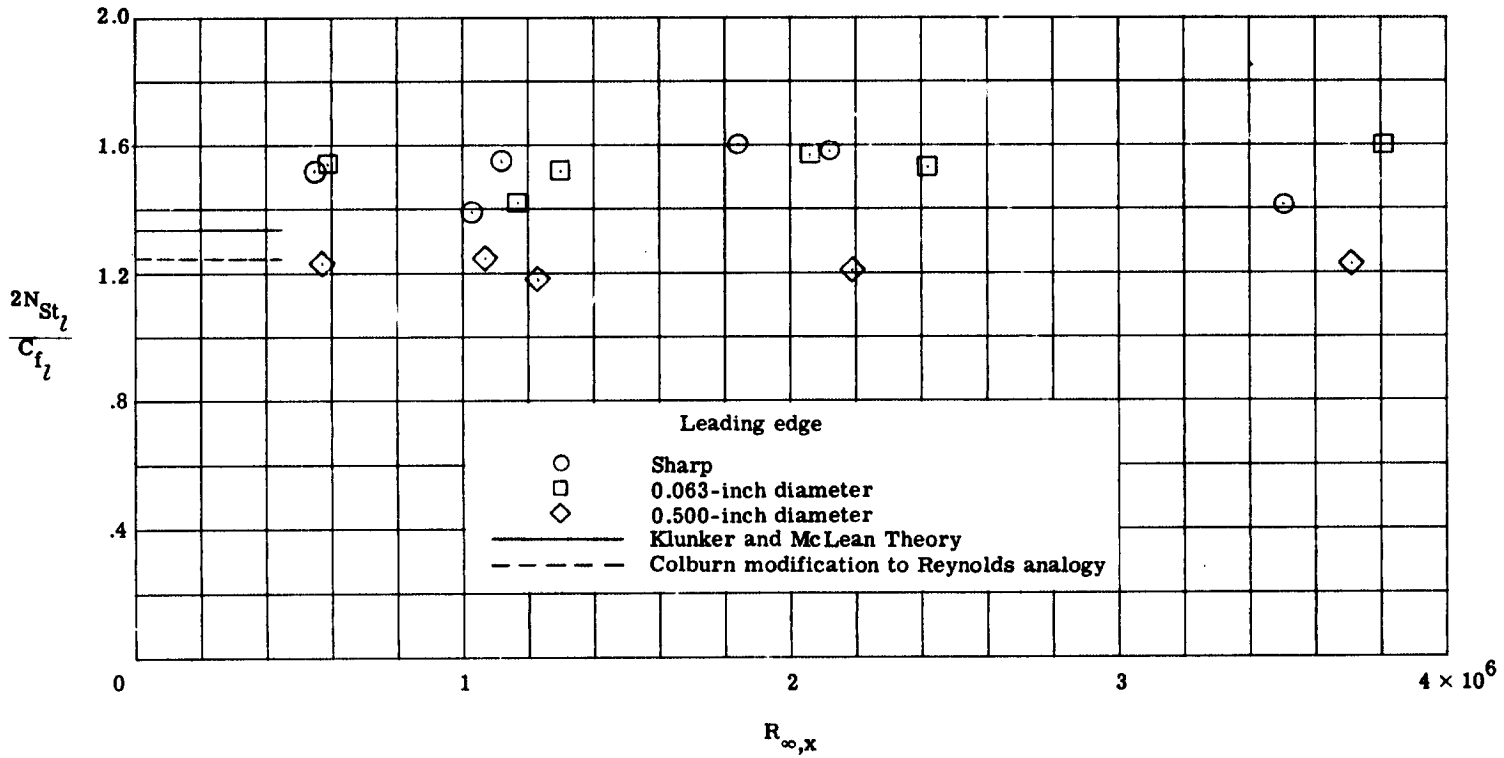

Figure 33.- Reynolds analogy factor.

pressure distributions for the leading-edge configurations of the present tests showed that the level and gradient for the sharp and 0.063-inch-diameter leading-edge models were similar and while the gradient for the 0.50-inch-diameter leading-edge model was relatively large the level at the trailing edge of the model was close to the sharp model distribution. Thus the present data suggest that the Reynolds analogy factor is related to the exponent n of the power law variation of the wall-pressure distribution ($p_w \propto x^n$).

The average Reynolds analogy factor for the sharp leading-edge data is 12.7 percent greater than the Klunker and McLean theory prediction. While this difference is less than the overall accuracy, the data are consistently above the theory. The reason for this difference is not known at present.

CHAPTER VI

CONCLUSIONS AND RECOMMENDATIONS

A program has been undertaken to examine the effect of leading-edge thickness on the laminar flat-plate boundary layer in a nominal Mach 10.4 stream. The model for the experimental part of the program was a 30-inch flat plate with cylindrical leading edges 0.002, 0.063, and 0.50 inches in diameter. The unit Reynolds number was varied from 0.04×10^6 to 0.13×10^6 per inch. The experimental program consisted of oil-flow tests to determine the local flow direction on the plate surface near the centerline for various end plate configurations, measurement of the heat transfer and wall pressure distributions, and impact-pressure surveys of the boundary layer at two locations on the model centerline. The boundary layer velocity profiles, local skin friction, boundary layer thickness, and Reynolds analogy factor were calculated from the measured data and examined in this program. The results of this experimental program and comparisons with theory support the following conclusions:

(1) At the lowest unit Reynolds number tested, the viscous-induced pressure distribution on the sharp leading-edge model was slightly greater than the bluntness- and viscous-induced pressure

distribution on the 0.063-inch-diameter leading-edge model 93 to 469 diameters from the leading edge. Increasing the unit Reynolds number decreased the general level of the data due to boundary layer thinning. The level of the viscous-induced pressures for the forward portion of the sharp leading-edge model at the highest unit Reynolds number was lower than the bluntness- and viscous-induced pressures of the 0.063-inch-diameter plate.

(2) The impact-pressure profiles for the sharp leading-edge model in a boundary-layer induced pressure gradient agreed with the zero-pressure gradient theory of Klunker and McLean based on free-stream conditions. This agreement supports the hypersonic boundary-layer independence principle of Hayes and Probstein. A low pressure correction for viscosity was used in the theory.

(3) The bluntness effect of the 0.063-inch-diameter leading edge resulted in a thicker boundary layer than for the sharp leading edge with an entropy gradient encompassing the boundary layer and much of the external flow.

(4) The 0.50-inch-diameter leading-edge impact-pressure profiles indicated that within 58.5 diameters of the leading edge the boundary-layer edge total pressure is equal to the free-stream impact pressure, and, therefore, the boundary-layer streamlines have passed through a normal shock.

(5) The velocity profiles and local skin friction coefficients for the sharp leading-edge model agreed with the Klunker and McLean

theory. Going from the sharp leading edge to the 0.063-inch and 0.50-inch-diameter leading edges first decreased and then increased the slope of the velocity profiles and the local skin friction.

(6) A plot of boundary-layer velocity profiles nondimensionalized by the experimental outer edge velocities and characteristic boundary-layer lengths revealed similarity for all the profiles regardless of leading-edge bluntness for the inner 60 percent of the boundary layer. A correlation of boundary-layer thickness for all leading edges was good.

(7) The heat transfer data for the sharp leading-edge model were somewhat above the Klunker and McLean theory, and a pressure correction due to Bertram and Feller adequately modified the data. Progressively blunting the leading edge had the same effect on the heat-transfer distributions as was found for the local skin friction.

(8) The Reynolds analogy factor based on local conditions $2N_{ST_l}/C_{f_l}$ was approximately 1.53 for the sharp leading-edge data, 1.51 for the 0.063-inch-diameter leading-edge data, and 1.22 for the 0.50-inch-diameter leading-edge data. The Reynolds analogy factor was found to be a function of the exponent n of power law variation of the wall pressure distribution.

While these conclusions are limited to the range of parameters for which data was obtained in this investigation, there is no reason to believe that these conclusions are not indicative of the trends behind sharp and blunt leading edges in hypersonic flow.

There are, however, interesting problems brought to light by this investigation and still to be considered. They are:

(1) What is the full range of diameters from a blunt leading edge and Reynolds number based on leading-edge diameter where the wall pressure is lower than the viscous-induced pressures on a sharp leading-edge model How can these distributions be predicted?

(2) Will a zero-pressure gradient boundary-layer theory satisfactorily predict the boundary-layer profiles behind a sharp leading-edge in a strong interaction viscous-induced pressure gradient?

(3) How far behind a blunt leading edge does the entropy gradient become important to the boundary layer profiles?

(4) How can the boundary-layer profiles be calculated in such a flow field?

(5) What is the relationship between Reynolds analogy factor and the pressure gradient?

(6) To what extent does this dependency remain independent of leading-edge diameter?

REFERENCES

1. Lees, Lester; and Probstein, R. F.: Hypersonic Viscous Flow over a Flat Plate. Princeton University, Report no. 195, April 1952.

2. Moulic, E. S., Jr.: Local Skin Friction and Induced Pressure Measurements on a Sharp-Edged Insulated Flat Plate in Low Density Hypersonic Flow. University of California Space Sciences Laboratory, NSF GP-2520, Series 7, Issue no. 3, January 1966.

3. Lees, Lester: Inviscid Hypersonic Flow over Blunt-Nosed Slender Bodies. GALCIT Memo no. 31, February 1, 1956.

4. Cheng, H. K.; Hall, J. Gordon; Golian, T. C.; and Hertzberg, A.: Boundary-Layer Displacement and Leading Edge Bluntness Effects in High-Temperature Hypersonic Flow. Journal of the Aeronautical Sciences, vol. 28, no. 5, May 1961, pp. 353-381.

5. Kendall, James M., Jr.: An Experimental Investigation of Leading-Edge Shock-Wave Boundary-Layer Interaction at Mach 5.8. Journal of the Aeronautical Sciences, vol. 24, no. 1, January 1957, pp. 47-56.

6. Lees, Lester: Hypersonic Flow. GALCIT Pub. no. 404, 1955.

7. Graham, W. J.; and Vas, I. E.: The Effect of Leading Edge Conditions on the Detailed Flow over a Flat Plate at M = 11.7. Princeton University, USAF ARL 138, September 1961.

8. Marvin, Joseph G.: Surface Pressures and Heat Transfer on Unswept Blunt Plates in Helium at High Mach Numbers. NASA TN D-688, March 1961.

9. Bertram, Mitchel H.; and Feller, William V.: A Simple Method for Determining Heat Transfer, Skin Friction, and Boundary-Layer Thickness for Hypersonic Laminar Boundary-Layer Flows in a Pressure Gradient. NASA Memo 5-24-59L, June 1959.

10. Harvey, William D.: Effects of Leading-Edge Bluntness on Pressure and Heat Transfer Measurements over a Flat Plate at a Mach Number of 20. NASA TN D-2846, October 1965.

11. Bertram, Mitchel H.; and Blackstock, T. A.: Some Simple Solutions to the Problem of Predicting Boundary-Layer Self-Induced Pressures. NASA TN D-798, April 1961.

12. Creager, Marcus O.: Effect of Leading-Edge Thickness on the Flow over a Flat Plate at a Mach Number of 5.7. NASA TN D-313, May 1960.

13. Neal, Luther, Jr.: A Study of the Pressure, Heat Transfer, and Skin Friction on Sharp and Blunt Flat Plates at Mach 6.8. NASA TN D-3312, April 1966.

14. Baradell, Donald L.; and Bertram Mitchell H.: The Blunt Plate in Hypersonic Flow. NASA TN D-408, October 1960.

15. Townsend, J. C.; Vollmar, W. R.; and Vas, I. E.: The Leading Edge Effect on the Flow over a Flat Plate at M = 10. Princeton University ARL 66-0145, July 1966.

16. Bradfield, W. S.; DeCoursin, D. G.; and Blumer, C. B.: The Effect of Leading-Edge Bluntness on a Laminar Supersonic Boundary Layer. Journal of the Aeronautical Sciences, vol. 21, no. 6, June 1954, pp. 373-382.

17. MacMillan, F. A.: Viscous Effects on Flattened Pitot Tubes at Low Speeds. Journal of the Royal Aeronautical Society, vol. 58, pp. 837-839.

18. Love, E. S.: A Reexamination of the Use of Simple Concepts for Predicting the Shape and Location of Detached Shock Waves. NACA TN-4170, December 1957.

19. Li, Ting-Yi; and Nagamatsu, H. T.: Hypersonic Viscous Flow on a Noninsulated Flat Plate. GALCIT Memo. no. 25, April 1955.

20. Van Driest, E. R.: Investigation of Laminar Boundary Layer in Compressible Fluids Using the Crocco Method. NACA TN-2597, January 1952.

21. Klunker, E. B.; and McLean, F. Edward: Effect of Thermal Properties on Laminar Boundary-Layer Characteristics. NACA TN-2916, March 1953.

22. Hilsenwrath, Joseph; Beckett, Charles W., et al.: Tables of Thermal Properties of Gases. NBSCir. 564, U.S. Dept. of Commerce, 1955.

23. Ames Research Staff: Equations, Tables, and Charts for Compressible Flow. NACA Rept. 1135, 1953 (Supercedes NACA TN-1428).

24. Johnston, Herrick L.; Mattox, Robert W.; and Powers, Robert W.: Viscosities of Air and Nitrogen at Low Pressures, NACA TN-2546, November 1951.

25. Grieser, Daniel R.; Goldthwaite, William H.: Experimental Determination of the Viscosity of Air in the Gaseous State at Low Temperatures and Pressures. AEDC-TDR-63-143, June 1963.

26. Erickson, Wayne D.; and Creekmore, Helen S.: A Study of Equilibrium Real-Gas Effects in Hypersonic Air Nozzles, including Charts of Thermodynamic Properties for Equilibrium Air. NASA TN D-231, April 1960.

27. Hayes, Wallace D.; and Probstein, Ronald F.: Hypersonic Flow Theory. Academic Press, 1959.

28. Hayes, Wallace D.; and Probstein, Ronald F.: Viscous Hypersonic Similitude. Journal of the Aero/Space Sciences, December 1959, pp. 815-824.

29. Creager, Marcus O.: Effects of Leading-Edge Blunting on the Local Heat Transfer and Pressure Distribution over Flat Plates in Supersonic Flow. NACA TN-4142, December 1957.